COPPER-BASED TERNARY OXIDE SEMICONDUCTORS FOR SOLAR ENERGY CONVERSION AND ENVIRONMENTAL REMEDIATION

by

MOHAMMAD KABIR HOSSAIN

DISSERTATION

Submitted in partial fulfillment of the requirements
for the degree of Doctor of Philosophy at
The University of Texas at Arlington
August, 2019

Arlington, TX

Supervising committee:

Krishnan Rajeshwar, Supervising Professor
Robin T. Macaluso
Daniel W. Armstrong
Peter Kroll

To the memories of my Late Mother

ACKNOWLEDGMENTS

During the past five years of my life as a graduate student, I had remarkable opportunities to work and crossed paths with certain individuals whose relentless support and motivations had been my core source of courage. I have always lacked adequate verbose hence failed to express how immensely I have enjoyed their companionship, guidance and keen help in every aspect of my PhD journey. Therefore, this acknowledgment section is the most satisfying part that I was looking forward to writing to appreciate and be grateful for the enormous support I received throughout this time.

First and foremost, I would like to thank God for blessing me with the requisite strength that I needed to survive this chapter of my life.

Then at the top of my prodigious list of people, I am truly thankful to my advisor, Dr Krishnan Rajeshwar. I am forever indebted to him for all his contributions of time, mentorship and motivations during these years. Not only he provided a suitable research environment to perform my graduate studies but, most importantly, he made sure that I take my work seriously. I sincerely appreciate the fact that he always made room for my research interests and he ensured his adequate assistance at pivotal moments in my work.

I would also like to convey my thankfulness to all my committee members, Dr. Robin T. Macaluso; Dr. Daniel W. Armstrong and Dr. Peter Kroll, for their comments, advice, and support to my research work. During my time I had the opportunity to collaborate with many other groups. I am particularly thankful to Dr. Csaba Janáky, Dr. Robin T. Macaluso, Dr. Mohammad N Huda, Dr. Ping Liu, and Dr. Claudia Longo for their supports and collaborations to complete my projects.

I owe an immense amount of gratitude to Dr. Thomas Abegayl, Dr. Attila Kormányos, Dr. Gergely F. Samu, Dr. Wilaiwan Chanmanee, Dr. Paola Sotelo, Dr. Miguel T. Galante, Dr. Mohammad Swakat Hossain, Dr. Dong Liu, Dr. Kinjal Gandha, Dr. Jeotikanta Mohapatra, Dr. Delphine Gout, Dr. Mohamamd F. Islam, Abbas Vali, Farinaz Firouzan and Hori Pada Sarker for their instructions, demonstrations and thoughtful discussions. I also appreciate John Ewoke and Saam Honarvar for their support in experimentations.

I thank Dr. William Cleaver and Dr. Cynthia Griffith for making my teaching duties easier. My profound gratefulness goes to Dr. Roy McDougald and Dr. Brian Edwards for their time and generous effort to ensure the smooth operation of the instruments. I hugely appreciate Debbie Cooke, Jill Howard, Stephanie Henry for their kind help and tremendous support.

I am indebted to my colleagues Jayanta K. Chakrabarty, Dr. Abu Hena Mostafa Kamal, Dr. ADA Shahinuzzaman, Dr. Sajib Barman and Afzal Shakar for their support, suggestion, and friendship. My humble gratitude also goes to Dr. Saiful M. Chowdhury for his suggestion and motivation throughout my PhD journey.

Finally, but by no means least, my heartiest gratitude is reserved for my parents who instilled a vision in me. I am thankful to my mother-in-law for her well wishes and support. Words will not be enough to articulate my heartfelt gratitude for my only sister-Fatema, my two brothers-Mosarof and Panir, and for my beloved better-half, Nazmy. I am blessed to have all of them in my life.

TABLE OF CONTENTS

LIST OF ILLUSTRATIONS

LIST OF TABLES

LIST OF ABBREVIATIONS

Å	Angstrom
AES	Atomic emission spectroscopy
BET	Brunauer-Emmet-Teller analysis
Calc	Calculated
CB	Conduction band
CPD	Contact potential difference
CV	Cyclic voltammetry
DFT	Density functional theory
DRS	Diffuse reflectance spectroscopy
DSC	Differential scanning calorimetry
EDS	Energy-dispersive x-ray spectroscopy
E_g	Energy gap
F_L	Fermi-level energy
FTO	Fluorine-doped tin oxide
FWHM	Peak full-width at half-maximum
HER	Hydrogen evolution reaction
HMT	Hexamethylenetetramine
ICP	Inductively-coupled plasma
IPCE	Incident photon-to-electron conversion efficiency
ITO	Tin-doped indium oxide
MA	Malic acid
NHE	Normal hydrogen electrode
Obs	Observed
OCP	Open circuit potential
PDF	Powder diffraction file

PEC	Photoelectrochemical
RHE	Reversible hydrogen electrode
SCS	Solution combustion synthesis
SEM	Scanning electron microscopy
SPV	Surface photovoltage
SPS	Surface photovoltage spectroscopy
TCO	Transparent conducting oxide
TEM	Transmission electron microscopy
TGA	Thermogravimetric analysis
UV-vis	Ultraviolet-visible
VB	Valence band
XRD	X-ray diffraction

ABSTRACT

COPPER-BASED TERNARY OXIDE SEMICONDUCTORS FOR SOLAR ENERGY CONVERSION AND ENVIRONMENTAL REMEDIATION

Mohammad Kabir Hossain, Ph.D.

The University of Texas at Arlington, 2019

Supervising Professor: Krishnan Rajeshwar

Photoelectrochemical (PEC) water splitting using inorganic semiconductors is a promising approach to convert sunlight into sustainable fuels. However, many scientific and engineering challenges need to be overcome before its commercialization. Oxide semiconductors offer many advantages such as stability in a variety of electrolytes, a diverse range of bandgaps and their Earth-abundance in nature. In this respect, many binary metal oxides have been investigated thoroughly; however, unfortunately, a suitable candidate for PEC water splitting has not been identified. While many efforts are ongoing to overcome the limitations of binary metal oxides, it is also essential to expand the search to more complex oxide families such as ternary, quaternary as well as to their composites. Nevertheless, this warrants a *time-efficient* route of synthesis to study such a large number of possible combinations (8,000 ternary and 700,000 quaternary oxides).

Herein, we studied several complex oxides in the Cu-Bi-V-O system using a rapid- and energy-efficient solution combustion synthesis (SCS). We demonstrated the synthesis of binary CuO and α-Bi_2O_3 as well as their ternary combination, $CuBi_2O_4$. In addition, we prepared several

composites of $CuBi_2O_4$ with binary CuO and α-Bi_2O_3. We systematically studied the optical and PEC behavior of these oxides and found improved photoactivities by the composites than their parent oxides which are attributed to the vectorial transfer of photogenerated carriers in them.

Similarly, we developed a complexation-assisted solution combustion synthesis for multiple ternary copper vanadates. Four copper vanadates, namely α-CuV_2O_6, α/β-$Cu_2V_2O_7$ and γ-$Cu_3V_2O_8$, were prepared in "one-pot" by simply tuning the Cu/V mole ratio in the precursor solutions. This enabled comparative PEC performance assessment of these vanadates toward water splitting. The α-CuV_2O_6 polymorph outperformed the other three copper vanadates in PEC water splitting. This performance enhancement was attributed to its unique crystal structure and direct nature of the optical transition from the valence to the conduction band.

CHAPTER 1

INTRODUCTION

Solar fuels generation *via* water splitting or carbon dioxide reduction using inorganic semiconductors is an attractive route for sustainable energy supply. Among various inorganic semiconductors, metal oxide semiconductors are promising because of attributes such as excellent stability against photocorrosion and Earth-abundance.[1-3] However, of the myriad binary oxide semiconductors that have been studied, only a few such as Cu_2O, CuO, WO_3 and Fe_2O_3 are visible light active which is a desired characteristic in a photocatalyst for optimum utilization of available solar energy.[4,5] In addition, short carrier lifespans through extensive recombination and/or sluggish transport properties is another shortcoming of many binary metal oxides. Hematite (Fe_2O_3), irrespective of its suitable band gap (~2 eV) and excellent photostability, falls in the above category.[6]

While efforts are ongoing to suppress carrier recombination in binary oxides via nanostructuring as well as lowering the band gap by doping (also termed as 'band engineering'), it is also imperative to expand materials search towards more complex oxides (ternary or quaternary oxides and their composites).[7-8] Interestingly, $BiVO_4$, one of the best performing visible-light active PEC catalysts, has been found in the ternary family system.[9] Moreover, band edge engineering to align the conduction band or the valence band for appropriate reduction and oxidation reactions respectively has also evolved as another approach for improving catalyst performance. This is usually accomplished by incorporating a suitable cation to the existing oxide

and thus making more complex, ternary or quaternary, oxides. For example, the band gap and band-edge position of Ag_2WO_4 are not suitable for the hydrogen evolution reaction (HER).[10] Nonetheless, incorporation of Bi (6s) orbitals with existing W (5d) orbitals has shown the uplift of band-edge position toward more negative potentials which makes it more suitable for HER.[10-11] Recently, a similar approach has been applied theoretically to tune the band gap of $CuWO_4$ (2.2 eV) by incorporating Bi which suggested a stable quaternary $CuBiW_2O_8$ with the band gap, 1.4 eV.[12]

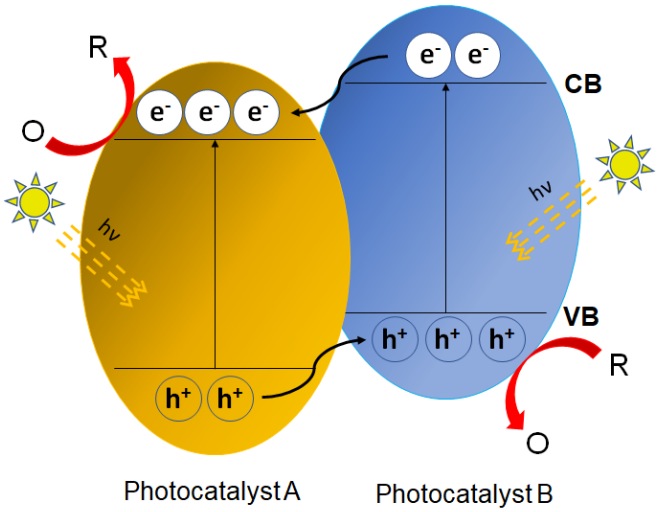

Figure 1-1. Schematic diagram of a *p-n* heterojunction showing vectorial electron-hole separation.

Another approach to tackle carrier recombination is the formation of a suitable heterojunction of two photocatalysts with different band positions. Thus, charge carriers generating in two different photocatalysts are vectorially transferred to the other material and hence hinders the possible recombination pathway.[13] Figure 1-1 shows a *p-n* heterojunction where photogenerated electrons in photocatalyst B can vectorially migrate to the more stable conduction band of photocatalyst A, and holes can migrate to the opposite direction. In this way, the conduction band of photocatalyst A becomes electron-rich while the valence band of photocatalyst B becomes hole-

rich and thus can perform the reduction and oxidation reactions effectively. Although heterojunctions of various binary oxides have been explored exhaustively, many heterojunctions in the ternary/quaternary families remain unexplored.

Copper oxides (Cu_2O/CuO) have drawn much attention due to their favorable band gaps (Cu_2O~ 2.0 - 2.2 eV/CuO~ 1.33 - 1.7 eV), non-toxicity and applicability for CO_2 conversion to value-added fuels. Furthermore, the component elements (Cu, O) are abundant on the Earth's crust (unlike metals such as Ga or In).[14] However, a major drawback of copper oxides is their poor chemical and PEC stability in aqueous solutions, originating from the location of their redox potentials, which lie within their band gaps (Figure 1-2).

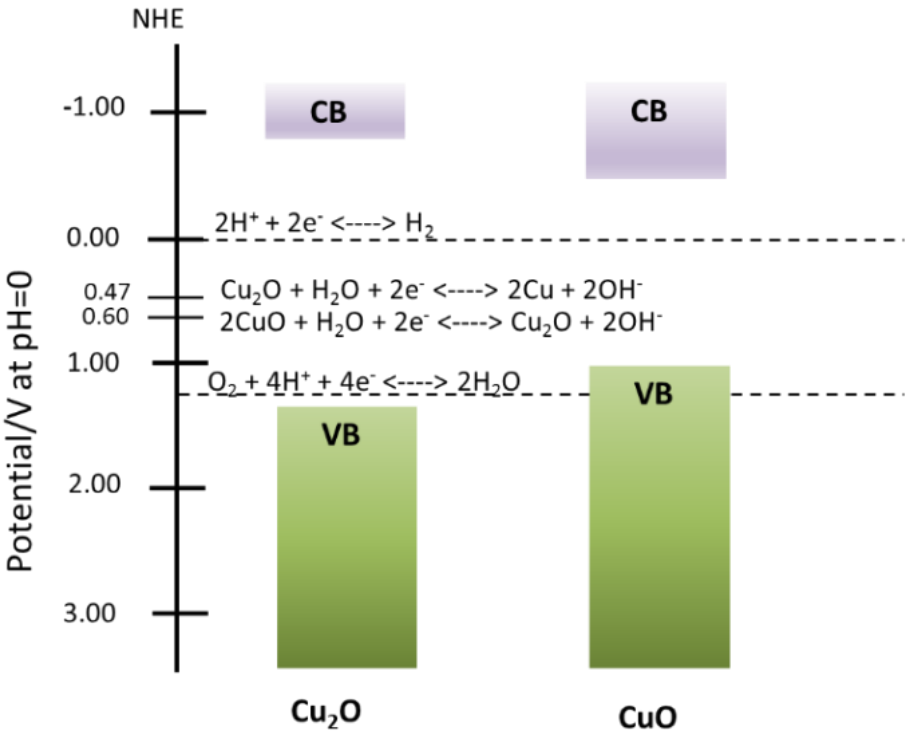

Figure 1-2. Band edge positions of copper oxides and their reduction potentials along with relevant potentials for water splitting.

Strategies such as coating a protective layer on the electrode surface by atomic layer deposition or introducing one or more cations to alter the electronic and structural properties have been demonstrated to overcome this limitation and have had varying levels of success .[15-18]

Another avenue is to search for *new* oxide semiconductor candidates. Thus, layered Cu (I)-based ternary delafossite oxides ($CuMO_2$, M= Fe, Rh, Cr, Ga, Al) have been reported[19-22] with increased stability stemming from the presumed introduction of M(III) orbitals in the conduction band (CB). For example, Fe(III) dominates the CB in $CuFeO_2$ acting as an electron acceptor orbital instead of Cu 3d and making the parent compound more stable.[18-21] Nevertheless, most of the delafossite oxides have high band gaps and therefore have been studied extensively only for transparent conducting oxide (TCO) applications.[23]

Along with delafossites, Cu (II)-based spinel-type oxides (CuM_2O_4) such as $CuBi_2O_4$, $CuFe_2O_4$, $CuCo_2O_4$, $CuCr_2O_4$ and $CuMn_2O_4$ have also shown reasonable water splitting activities and better stability than their binary counterparts.[24-26] Furthermore, divalent Cu is oxidatively more stable than the monovalent Cu. Despite that, photocatalytic studies of these oxides are limited and only a few studies have been reported relating to H_2 evolution from water.[24-26]Among various Cu-based spinels, recently $CuBi_2O_4$ has drawn much attention due to its low band gap (~1.8 eV) and favorable band edge positions for photocatalytic hydrogen evolution. Besides, $CuBi_2O_4$ also displayed more photostability compared to binary CuO. Ternary $CuBi_2O_4$ can also form composites either with CuO or Bi_2O_3 by varying the precursor stoichiometry. Consequently, $CuO/CuBi_2O_4$ composite with improved charge separation was reported using the co-precipitation method.[26]

More recently, a combinatorial analysis identified several copper vanadate phases such as CuV_2O_6, $Cu_2V_2O_7$, and $Cu_3V_2O_8$ with band gaps of ~ 2.0 eV and their self-passivation was

demonstrated in weakly alkaline borate electrolytes pointing to the promise of these materials as PEC photoanodes.[28,29] However, there is only limited literature on the effect of morphology and synthetic method choice on photocatalytic performance for these compounds.

Synthesis of ternary and quaternary oxides, as well as their multitude of possible composites in a time-efficient manner, is another challenge. Solution combustion synthesis (SCS), which is the wet chemical version of combustion synthesis (CS), has emerged recently as a time-and energy-efficient synthetic method for a range of oxides.[30,31] This latter method employs metal salts such as nitrates, sulfates, carbonates as oxidants and fuels such as urea, glycine, hexamethylene-tetramine (HMT), sucrose or starch as reducing agents. Once the reaction mixture is brought to the ignition temperature, self-generated heat triggers combustion and converts the precursors to their respective metal oxides without the addition of further external energy input. The reaction happens in a short time period (usually 3-10 min), evolving large amounts of gases and leaving behind the oxide nanoparticles. The morphology, particle size, and crystallinity can be optimized by altering the fuel, varying the fuel-to-oxidizer ratio and annealing at different temperatures.[32] In SCS, precursor stoichiometry can also be easily varied, and a range of composites can be formed.

In this respect, we were interested to systematically study Cu-Bi-V-O system towards PEC applications. Figure 1-3 represents a ternary diagram showing possible combinations of various ternary and quaternary oxides in this system. Along the CuO-Bi_2O_3 line of Figure 1-3, there is only one possible ternary composition-$CuBi_2O_4$, and similarly, one ternary $BiVO_4$ along the Bi_2O_3-V_2O_5 line. However, there are multiple possible ternary compounds are available in the Cu-V-O system.

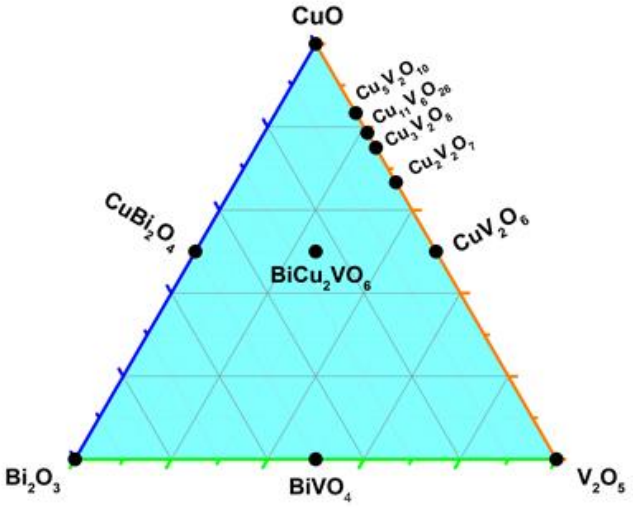

Figure 1-3. Ternary diagram of Cu-Bi-V-O system showing different thermodynamically possible ternary and quaternary compounds

From this perspective, this dissertation focuses on the development of suitable SCS-based rapid one-pot methods to tune the composition of ternary Cu-Bi-O and Cu-V-O systems as well as to study their PEC behavior. Chapter 2 of this dissertation deals with a review on the solution combustion synthesis of various complex oxides. This chapter discusses the effect of a range of controlling parameters to tune the reaction condition for the expected product. In addition, a discussion on the application of SCS-derived oxides toward solar energy conversion has been drawn. Chapter 3 describes the preparation of binary CuO, Bi_2O_3 oxides; ternary $CuBi_2O_4$, and their composites using a time- and energy-efficient route. A comparative analysis of the composites and their parent oxides toward photoelectrochemical hydrogen generation has been developed. A rapid one-pot synthesis method of four copper vanadates and their photoelectrochemical behavior have been discussed in chapter 4. A computational study to explain experimental results has also been performed. Finally, chapter 5 concludes with a summary and future directions.

REFERENCES.

1. Kudo, A.; Miseki, Y. Heterogeneous Photocatalyst Materials for Water Splitting. *Chem. Soc. Rev.* 2009, *38*, 253-278.
2. Osterloh, F. Inorganic Materials as Catalysts for Photochemical Splitting of Water. *Chem. Mater.* 2008, *20*, 35-54.
3. Sivula, K.; van de Krol, R. Semiconducting Materials for Photoelectrochemical Energy Conversion. *Nat. Rev. Mater.* 2016, *1*.
4. van de Krol, R.; Liang, Y.; Schoonman, J. Solar Hydrogen Production with Nanostructured Metal Oxides. *J. Mater. Chem.* 2008, *18*, 2311.
5. Rajeshwar, K.; Thomas, A.; Janáky, C. Photocatalytic Activity of Inorganic Semiconductor Surfaces: Myths, Hype, and Reality. *J. Phy. Chem. Lett.* 2015, *6*, 139-147.
6. Kleiman-Shwarsctein, A.; Huda, M.; Walsh, A.; Yan, Y.; Stucky, G.; Hu, Y.; Al-Jassim, M.; McFarland, E. Electrodeposited Aluminum-Doped α-Fe_2O_3 Photoelectrodes: Experiment and Theory. *Chem. Mater.* 2010, *22*, 510-517.
7. Abdi, F.; Berglund, S. Recent Developments in Complex Metal Oxide Photoelectrodes. *J. Phys. D: Appl. Phys.* 2017, *50*, 193002.
8. Woodhouse, M.; Parkinson, B. Combinatorial Approaches for the Identification and Optimization of Oxide Semiconductors for Efficient Solar Photoelectrolysis. *Chem. Soc. Rev.* 2009, *38*, 197-210.
9. Kim, T.; Choi, K. Nanoporous $BiVO_4$ Photoanodes with Dual-Layer Oxygen Evolution Catalysts for Solar Water Splitting. *Science* 2014, *343*, 990-994.
10. Tang, J.; Ye, J. Correlation of Crystal Structures and Electronic Structures and Photocatalytic Properties of the W-Containing Oxides. *J. Mater. Chem.* 2005, 15, 4246-4251.
11. de Tacconi, N.; Timmaji, H.; Chanmanee, W.; Huda, M.; Sarker, P.; Janáky, C.; Rajeshwar, K. Photocatalytic Generation of Syngas Using Combustion-Synthesized Silver Bismuth Tungstate. *ChemPhysChem* 2012, *13*, 2945-2955.
12. Sarker, P.; Prasher, D.; Gaillard, N.; Huda, M. Predicting a New Photocatalyst and Its Electronic Properties by Density Functional Theory. *J. Appl. Phys.* 2013, *114*, 133508-133508.
13. Moniz, S.; Shevlin, S.; Martin, D.; Guo, Z.; Tang, J. Visible-Light Driven Heterojunction Photocatalysts For Water Splitting – a Critical Review. *Energy Environ. Sci.* 2015, *8*, 731-759.
14. Rajeshwar, K.; Hossain, M.; Macaluso, R.; Janáky, C.; Varga, A.; Kulesza, P. Copper Oxide-Based Ternary and Quaternary Oxides: Where Solid-State Chemistry Meets Photoelectrochemistry. *J. Electrochem. Soc.* 2018, *165*, H3192-H3206.
15. Paracchino, A.; Laporte, V.; Sivula, K.; Grätzel, M.; Thimsen, E. Highly Active Oxide Photocathode for Photoelectrochemical Water Reduction. *Nat. Mater.* 2011, *10*, 456-461.
16. Yin, W.; Tang, H.; Wei, S.; Al-Jassim, M.; Turner, J.; Yan, Y. Band Structure Engineering of Semiconductors for Enhanced Photoelectrochemical Water Splitting: the Case of TiO2. *Phys. Rev. B* 2010, *82*, 0451061-0451062.
17. Zhang, Z.; Wang, P. Highly Stable Copper Oxide Composite as an Effective Photocathode for Water Splitting via a Facile Electrochemical Synthesis Strategy *J. Mater. Chem.* 2012, *22*, 2456-2464.
18. Rajeshwar, K.; de Tacconi, N.; Ghadimkhani, G.; Chanmanee, W.; Janáky, C. Tailoring

Copper Oxide Semiconductor Nanorod Arrays for Photoelectrochemical Reduction of Carbon Dioxide to Methanol. *ChemPhysChem* 2013, *14*, 2251-2259.

19. Ma, Y.; Zhou, X.; Ma, Q.; Litke, A.; Liu, P.; Zhang, Y.; Li, C.; Hensen, E. Photoelectrochemical Properties of $CuCrO_2$: Characterization of Light Absorption and Photocatalytic H_2 Production Performance. *Catal. Lett.* 2014, *144*, 1487-1493.
20. Gu, J.; Yan, Y.; Krizan, J.; Gibson, Q.; Detweiler, Z.; Cava, R.; Bocarsly, A. *p*-Type $CuRhO_2$ as a Self-Healing Photoelectrode for Water Reduction under Visible Light. *J. Am. Chem. Soc.* 2014, *136*, 830-833.
21. Prévot, M.; Li, Y.; Guijarro, N.; Sivula, K. Improving Charge Collection with Delafossite Photocathodes: a Host–Guest $CuAlO_2$/$CuFeO_2$ Approach. *J. Mater. Chem. A* 2016, *4*, 3018-3026.
22. Prévot, M.; Guijarro, N.; Sivula, K. Enhancing the Performance of a Robust Sol–Gel-Processed *p*-Type Delafossite $CuFeO_2$ Photocathode for Solar Water Reduction. *ChemSusChem* 2015, *8*, 1494-1494.
23. Wang, Z.; Nayak, P.; Caraveo-Frescas, J.; Alshareef, H. Recent Developments in *p*-Type Oxide Semiconductor Materials and Devices. *Adv. Mater.* 2016, 28, 3831–3892.
24. Arai, T.; Konishi, Y.; Iwasaki, Y.; Sugihara, H.; Sayama, K. High-Throughput Screening Using Porous Photoelectrode for the Development of Visible-Light-Responsive Semiconductors. *J. Comb. Chem.* 2007, *9*, 574-581.
25. Saadi, S.; Bouguelia, A.; Trari, M. Photoassisted Hydrogen Evolution over Spinel CuM_2O_4 (M=Al, Cr, Mn, Fe and Co). *Renew. Energy* 2006, *31*, 2245-2256.
26. Boumaza, S.; Bouarab, R.; Trari, M.; Bouguelia, A. Hydrogen Photo-evolution over the Spinel $CuCr_2O_4$. *Energ. Convers. Manage.* 2009, *50*, 62-68.
27. Patil, R.; Kelkar, S.; Naphade, R.; Ogale, S. Low Temperature Grown $CuBi_2O_4$ with Flower Morphology and Its Composite with CuO Nanosheets for Photoelectrochemical Water Splitting. *J. Mater. Chem. A* 2014, *2*, 3661-3668.
28. Zhou, L.; Yan, Q.; Shinde, A.; Guevarra, D.; Newhouse, P.; Becerra-Stasiewicz, N.; Chatman, S.; Haber, J.; Neaton, J.; Gregoire, J. Solar Fuel Photoanodes Prepared by Inkjet Printing of Copper Vanadates. *Adv. Energy Mater.* 2015, *5*, 1-13.
29. Zhou, L.; Yan, Q.; Yu, J.; Jones, R.; Becerra-Stasiewicz, N.; Suram, S.; Shinde, A.; Guevarra, D.; Neaton, J.; Persson, K.; Gregoire, J. Stability and Self-Passivation of Copper Vanadate Photoanodes Under Chemical, Electrochemical, and Photoelectrochemical Operation. *Phys. Chem. Chem. Phys.* 2016, *18*, 9349-9352.
30. Patil, K.C.; Aruna, S.T.; Mimani, T. Combustion Synthesis: an Update. *Curr. Opin. Solid State and Mater. Sci.* 2002, *6*, 507-512.
31. Morales, W.; Cason, M.; Aina, O.; de Tacconi, N.; Rajeshwar, K. Combustion Synthesis and Characterization of Nanocrystalline WO_3. *J. Am. Chem. Soc.* 2008, *130*, 6318-6319.
32. Thomas, A.; Janáky, C.; Samu, G. F.; Huda, M. N.; Sarker, P.; Liu, J. P.; Van Nguyen, V.; Wang, E. H.; Schug, K. A.; Rajeshwar, K. Time- and Energy- Efficient Solution Combustion Synthesis of Binary Metal Tungstate Nanoparticles with Enhanced Photocatalytic Activity. *ChemSusChem* 2015, *8*, 1652−1663.

CHAPTER 2

SOLUTION COMBUSTION SYNTHESIS OF COMPLEX OXIDE SEMICONDUCTORS

ABSTRACT

This is a perspective of the role that combustion synthesis, specifically solution combustion synthesis, has played in the development of ternary and quaternary metal oxide semiconductors, and materials derived from these compounds such as composites, solid solutions, and doped samples. The attributes of materials, collectively termed “complex oxides” within the context of this discussion, are discussed in terms of their applicability in the generation of solar fuels from water splitting and CO_2 reduction, and environmental pollution remediation via heterogeneous photocatalysis.

2.1 INTRODUCTION

Metal oxides are important from both fundamental chemistry and practical application perspectives. They occur, in the solid state, in a fascinating array of crystallographic structures and polymorphs. Both their surfaces and bulk can be chemically altered to impart striking effects on their optoelectronic, charge transport, magnetic, or catalytic properties. The library of possible materials can be expanded by variation of both cationic and anionic sub-lattices within the oxide structure.[1-4] These, in turn, lead to a wide array of application possibilities in energy conversion, energy storage, microelectronics, magnetic devices, etc. Metal oxides can be electronically conducting or insulating, and their optical transparency can be tuned to afford a class of important technological materials termed transparent, conducting oxides or TCOs. Further, they can also exhibit semiconductor behavior and be made in either *n*- or *p*-type form. Utilization of sunlight using metal oxide semiconductors via artificial photosynthesis (to photoelectrochemically generate solar fuels) or photocatalytic degradation of environmental pollutants has attracted much attention in recent years.[5-7] Although photocatalytic degradation of pollutants has found limited commercial success, artificial photosynthesis still languishes in the research laboratory in the absence of a "magic bullet" oxide semiconductor.

Photoelectrochemical generation of solar fuels demands a rigorous (even conflicting) set of material attributes including chemical/electrochemical robustness under irradiation, optimal optical attributes that match the solar spectrum, and exceptional bulk carrier transport and surface electrocatalytic attributes.[5-7] Furthermore, the component element(s) must be earth-abundant and non-toxic. Thus it is hardly surprising that no metal oxide has emerged so far, even after ~4 decades of research. The on-going search (the so-called Holy Grail, Ref. 8) has expanded beyond binary oxide semiconductors to ternary or even quaternary metal oxides.[4] Composites of multiple metal

oxides, solid solutions of metal oxides, and doping are attractive strategies for tweaking materials attributes for photoelectrochemical/photocatalytic applications. Control of the metal oxidation state (for example, the ratio of copper in the +1 or +2 states in copper oxide) in a solution combustion synthesis (SCS) environment is another intriguing avenue in this regard. Within the context of the present article, all these materials aspects are collectively termed as "complex oxides." While precedent reviews and a monograph exist for the combustion synthesis of *binary* metal oxides in general,[9-17] including from one of us previously,[16] we are not aware of an instance where combustion synthesis-derived *complex oxides* have been discussed from the above perspectives. This then constitutes the main theme of the present article with examples drawn from recent work in both our laboratories in the U.S. and in Hungary.

2.2 SYNTHETIC ASPECTS AND MECHANISTIC UNDERSTANDING

Where does combustion synthesis stand relative to other candidates available for the synthesis of metal oxides in nanocrystalline (powder) form? Table 1 shows the relevant aspects.

Table 2-1. Attributes of Solution Combustion Synthesis Relative to Other Routes for the Preparation of Nanocrystalline Metal Oxide Powders

synthesis candidate	energy efficiency	time efficiency	comments
solution combustion synthesis	very good	very good	sample composition can be easily tuned
hydrothermal synthesis	very good	moderate	---
sol-gel	good	poor	mild conditions
ceramic	poor	poor	sample usually obtained in crystalline form
arc-melting and plasma	poor	very good	---

It is noted, as also exemplified by the other contributions in this special volume celebrating the successes of combustion synthesis, that there are many variants of combustion synthesis. For example, spray pyrolysis has been combined with combustion synthesis for preparing TCO films.[18] Indeed, the variant commonly deployed in most works, including our own, utilizes the so-called volume solution combustion mode.[19] Figure 2-1 outlines the essence of this commonly-used approach.

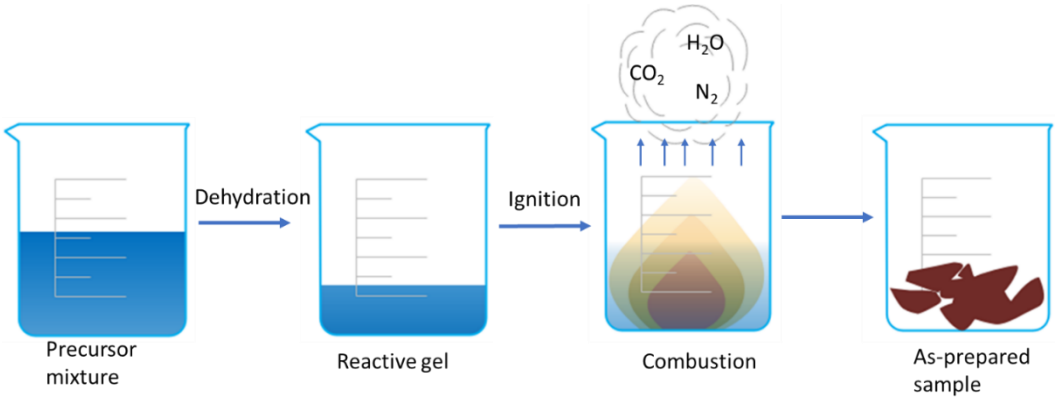

Figure 2-1. Schematic of the solution combustion synthesis variant used in the studies considered here.

The main handicap of the SCS approach is mostly associated with the lack of thermal control since the synthesis basically occurs in an explosive environment. Therefore, other, more controllable variants (e.g., self-propagating sol-gel combustion, Ref. 19) have been developed; see also other papers in this special volume.

The other handicap is that visualization of dynamic events occurring during the SCS itself is hampered, precluding close monitoring of the reaction progress and mechanisms. There is a fertile field of opportunity here for the development so operando techniques, especially based on optical (e.g., infra-red) probes that may be profitably inserted into the SCS environment. In other variants of SHS, thermocouples have been used in the combustion tube to measure the combustion

temperature and burn velocity.[20] Nonetheless, some degree of understanding of the mechanistic aspects of SCS may be gleaned by the use of thermal analysis (i.e., differential scanning calorimetry, DSC and thermogravimetric analysis, TGA) on the SCS precursors. An example is contained in Figure 2-2.

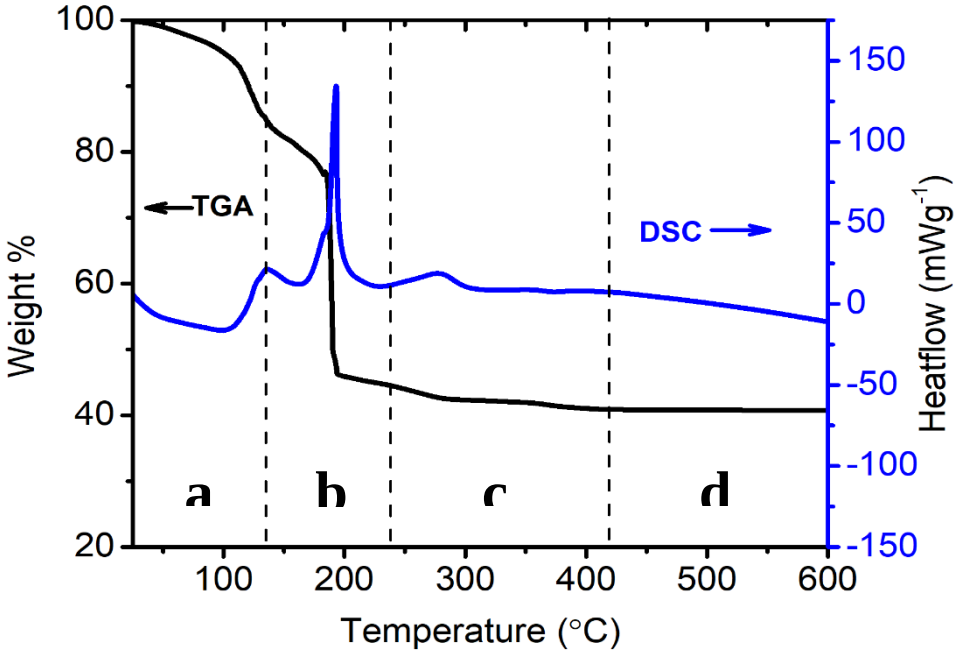

Figure 2-2. Representative DSC-TGA profile for a SCS precursor metal nitrate-fuel (e.g., urea) mixture. This example is for the SCS of copper bismuth oxide where stoichiometric amounts of copper nitrate, bismuth nitrate and urea were dissolved together in water to make the precursor mixture.

A quick gauge of the ignition temperature and exothermicity of a given reaction mixture can be attained by simulating SCS using DSC-TGA. A representative DSC-TGA profile for a SCS precursor is shown in Figure 2-2. Different stages in Figure 2-2 (shown by dashed lines) can be identified with: (a) endothermic loss of water (b) combustion reaction (c) removal of carbonaceous materials and (d) final product formation with constant mass. In Figure 2-2, the DSC peak at ~200 °C confirms the exothermic nature of the reaction and concurrent loss of mass corroborates the

evolution of gaseous products (c.f., Figure 2-1). The constant mass regime ‘d’ in the TGA scan (Figure 2-2) reflects the refractory nature of most metal oxides. Interestingly, use of data such as those in Figure 2-2 also serves to carefully delineate the temperature chosen for post-synthesis thermal anneal. This step is sometimes needed for improving the morphology of the oxide sample for the targeted application.

2.3 CONTROL OF THE METAL OXIDATION STATE

The fuel:oxidizer ratio (F/O) is a versatile tool in the control of many SCS-derived sample variables, including the metal oxidation state. Figures 2-3 and 2-4 contain data demonstrating the key role of F/O. Thus, a series of samples were derived from SCS where the F/O ratio was systematically varied (from 0.5 to 4.0, with hexamethylenetetramine (HMT) as the fuel). The F/O ratio directly affects the redox nature of the mixture, while the flame temperature is indirectly affected. Even at first glance, there are clear changes in the series of XRD patterns (Figure 2-3). The low F/O ratio regime corresponds to the most oxidative environment, consequently the most oxidized species (CuO) is formed under these circumstances. With an increase of the F/O ratio, alterations in the XRD profiles are seen (Figure 2-3), with the gradual appearance of the more reduced products (i.e., Cu_2O, Cu, Cu_3N). The nitride product is somewhat surprising and the mechanistic aspects underlying its formation (see below), requires further study, beyond the scope of this discussion.

Careful inspection of the XRD patterns furnished further insights on the composition. Figure 2-4 compares diffraction patterns recorded for samples synthesized with four different F/O ratios, and the position of the most relevant diffraction of the possible components is also presented. At low F/O ratios, the CuO phase was formed almost exclusively. Importantly, all CuO-related diffractions can be identified without the presence of any minority phase. With the increase of the

F/O ratio, diffractions related to the Cu_2O phase appeared first, as deduced from the reflections at 2θ = 36.5º, 42.4 º and 61.5º. With further increase of the fuel content, the CuO phase was completely attenuated, while reflections related to metallic Cu developed. Finally, at very high F/O ratios, diffractions of Cu_3N were spotted, together with the development of diffractions related to a mixed oxide-nitride phase.

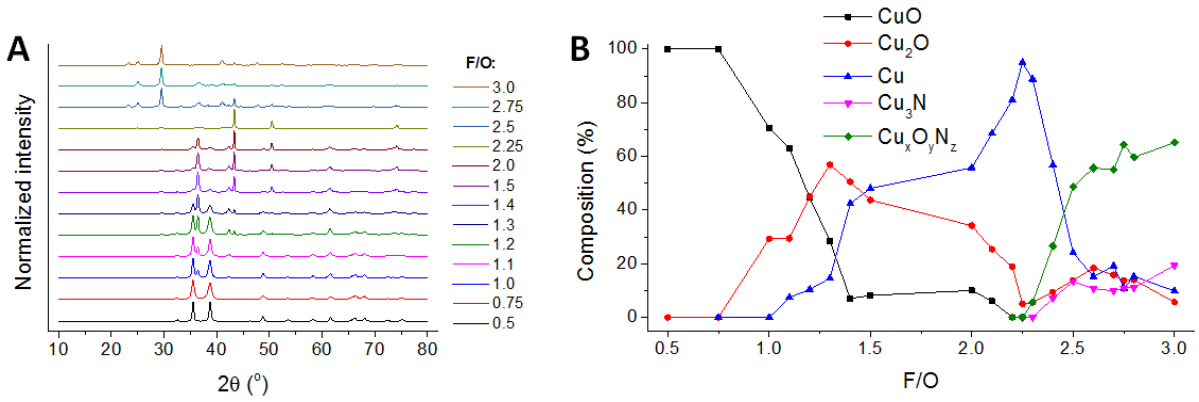

Figure 2-3. X-ray diffraction (XRD) patterns of solution combustion synthesized Cu_xO_y samples, obtained with different F/O ratios.

To assess the role of the reducing power of the fuel, the same set of experiments was carried out with urea. Similar trends were revealed, but similar compositions were obtained at different F/O ratios for the two systems. The higher reducing power of HMT is demonstrated in Figure 2-5, where the oxide reaction product was more Cu-rich, compared to its counterpart synthesized with urea fuel, under otherwise identical conditions. That is, the composition was skewed to a Cu:O ratio that was somewhat less than the predicted 2:1 level.

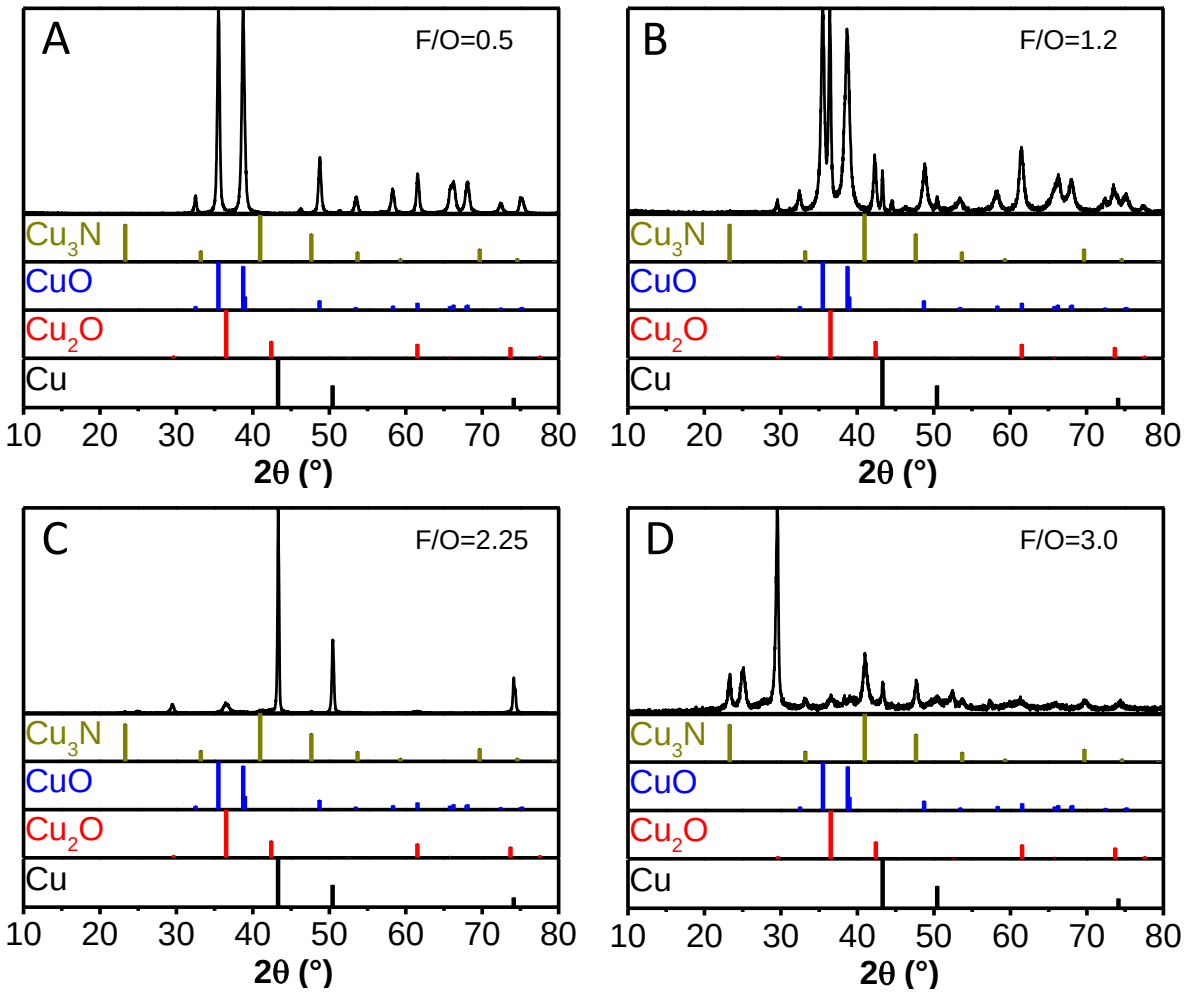

Figure 2-4. XRD patterns of solution combustion synthesized Cu_xO_y samples (using HMT fuel), obtained with four different F/O ratios, together with the patterns for the four relevant reference materials (see text).

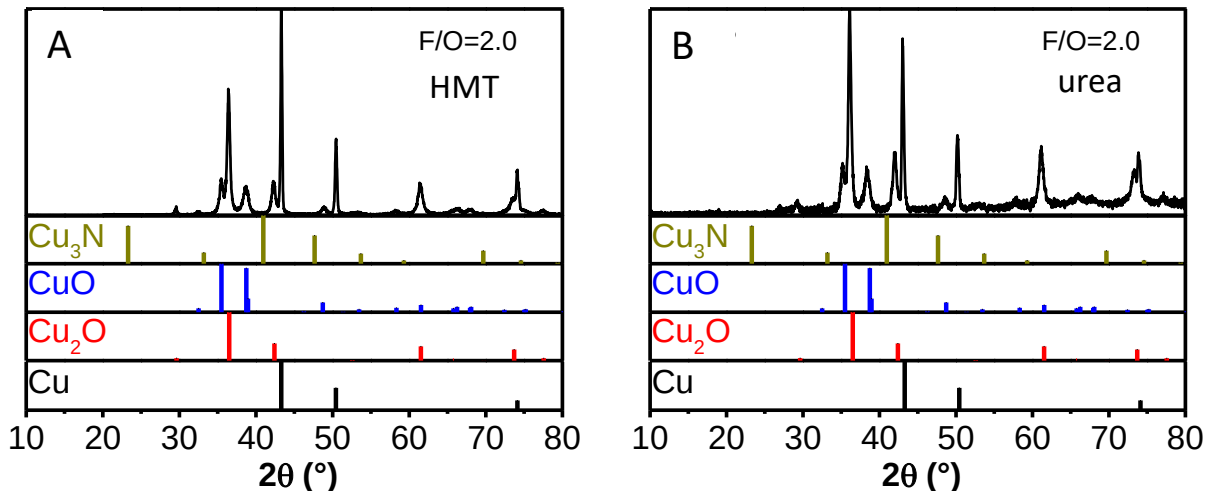

Figure 2-5. XRD patterns for solution combustion synthesized Cu_xO_y samples (using F/O = 2.0 ratio), obtained with two different fuels (HMT and urea), together with the patterns of the reference materials.

2.4 SCS OF TERNARY AND QUATERNARY OXIDES

A variety of *binary* metal oxides have been prepared via combustion synthesis. The earlier review articles cited above[11,12,16] provide a summary of this corpus of studies. Table 2 provides a compilation of ternary and quaternary metal oxides that have been derived from combustion syntheses. An impressive array of oxides spanning many important crystallographic structures have been synthesized using an equally diverse range of fuels. The effect of fuel in controlling the combustion intensity and thus the temperature attained is reflected in the corresponding range of nanoparticle morphology attributes (Columns 5-7) in Table 2.

Examples of data, reflecting the influence of SCS variables on the sample attributes, are morphology although these are as yet rather sparse on ternary oxides, confined only to a limited number of them. Different fuels such as urea, glycine, carboxymethylcellulose, citric acid, DL-malic acid, and mixed fuels were applied for synthesizing $BiVO_4$[40-42]. Use of urea or glycine showed a trace amount of V_2O_5 as impurity which was believed to be due to the lack of chelation of Bi^{3+} and VO^{3-} ions in the precursor mixture.[40-42] When citric acid, carboxymethylcellulose, and

DL-malic acid were used as fuel, it formed a single phase $BiVO_4$ due to their strong chelating action maintaining a homogeneous precursor mixture.[40-42] In terms of BET surface area, glycine and urea produced the lowest surface area values which can be correlated with their strong reducing power. While producing the maximum combustion temperature, as a result, agglomeration of particles, is an unfortunate consequence. On the other hand, use of carboxymethlycellulose or DL-malic acid led to the formation of single-phase $BiVO_4$ with higher surface areas i.e., 3.00 and 13.86 m^2/g respectively presumably stemming their slow, controlled combustion.[40]

Similarly, precursor chemistry also influences the purity of the final product. In the SCS of $CuWO_4$, $ZnWO_4$ and Ag_2WO_4, two different types of precursors namely $Na_2WO_4{\cdot}2H_2O$ and $(NH4)_2WO_4$, were used for the tungsten source.[44] Interestingly, $Na_2WO_4{\cdot}2H_2O$ produced an almost pure product while binary WO_{3-x} was always present as impurity when $(NH_4)_2WO_4$ was used as tungsten source.[44]

The F/O ratio was found to exert a great influence on the purity and product quality in the SCS of $Bi_2Ti_2O_7$.[49] Propulsion chemistry principles teaches that a maximum temperature can be achieved when the ratio is 1 (i.e., stoichiometric conditions). However, fuel-rich or fuel-lean conditions can often produce a superior product in terms of the desired phase, better crystallinity, higher surface area etc. In the case of $Bi_2Ti_2O_7$ with HMT as a fuel, only an amorphous product was formed when F/O = 1.5 or less. However, increasing F/O to 2.0 produced a well-crystallized material.[49] A similar trend was also found for the combustion synthesis of $FeAl_2O_4$ and $MgAl_2O_4$.[24-26] For the synthesis of $FeAl_2O_4$, different molar ratios of urea (3 to 7) were used; excess urea reduced the surface area and increased the particle size. However, after a certain F/O ratio, the surface area started to increase.[24]

Table 2-2. Ternary and Quaternary Oxides from Solution Combustion Synthesis and Sample Attributes

entry no.	crystal class	oxide	fuel used	average crystallite size (nm)	particle size (nm) from TEM	BET surface area (m^2/g)	ref
1		$CaFe_2O_4$	glycine	-	100	79.3	21
2		$CuBi_2O_4$	urea	35	300	1.9	22
3		$CuFe_2O_4$	urea	-	40-50	40	23
4		$FeAl_2O_4$	diethylamine hydrochloride and urea	16	-	179.3	24,25
5	spinel	$MgAl_2O_4$	glycine	21.3	-	12.1	26
6		$MgFe_2O_4$	urea	18	-	-	27
7		$MnFe_2O_4$	oxalyl dihydrazine	22	-	-	28
8		$NiFe_2O_4$	citric acid	-	-	-	29
9		$SnCd_2O_4$	citric acid	-	10-15	28	30
10		$ZnFe_2O_4$	urea	-	50	17	31
11		$GdFeO_3$	glycine	43	58	-	32
12		$LaFeO_3$	citric acid	24.1	24	25.8	33
			triethylamine hydrochloride	26.7	-	84.5	
13	perovskite	$LaNiO_3$	citric acid	23.1	~100	15.1	34
14		$SrTiO_3$	glycine	23	20	12	35
15		$YFeO_3$	glycine	50	50	6.4	36
			alanine	22	-	24.2	37
16	aurivillius	Bi_2MoO_6	tartaric acid	-	300-500	< 1	38
17		Bi_2WO_6	glycine	-	20-30	25.5	39
18	scheelite	$BiVO_4$	citric acid or urea or glycine	-	34	~1	40
			citric acid and urea	34	400–600	1.8	41

			sodium carboxymethylcellulose	-	400–600	3	42
			DL-malic acid	-	10–20	13.9	43
19	wolframite	$CuWO_4$	urea	22	-	13.2	44
20		$ZnWO_4$	urea	32	-	11.9	44
			sucrose	20-30	30-130	19.2	45
21	zircon	$LaVO_4$	glycine	-	5-80	3.2	46
22		$CeVO_4$	oxalyl dihydrazide	-	-	3	47
23	pyrochlore	$Bi_2Ce_2O_7$	glycine	-	5-6	15	48
24		$Bi_2Ti_2O_7$	hexamethylenetetramine (HMT)	-	61 ± 35	5	49
25		$Gd_2Ti_2O_7$	glycine	29.8	30	12.5	50
26		$Nd_2Ti_2O_7$	glycine	27.7	30	12.8	50
27		$Er_2Ti_2O_7$	glycine	33.2	30	11.8	50
28		$Bi_2Zr_2O_7$	urea	4-5	-	1.2	51
			tartaric acid	3-4	-	2.3	51
29	others	Ag_2WO_4	urea	22	33	21.3	44
30		$ZrMo_2O_8$	glycine	-	40−50	10	52
31		$CuNb_2O_6$	urea	20.3	20−60	8.8	53
32		$ZnNb_2O_6$	urea	15.8	20−60	18.4	53
33		ZrV_2O_7	glycine	-	30−40	-	54
34		$AgBiW_2O_8$	urea	6	6.6±1.0	34.4	55

2.5 COMPOSITES OF TERNARY METAL OXIDES, DOPED SAMPLES, AND SOLID SOLUTIONS VIA SOLUTION COMBUSTION SYNTHESIS

The distinction between composites and solid solutions relates to how two or more components are dispersed in a structural framework relative to one another. If the components are *phase-separated*, then the resultant framework is termed a composite. Thus in the Cu-Bi-O ternary system, composites of $CuBi_2O_4$ can be formed with either of its components, CuO or Bi_2O_3.[22] Both neat CuO and Bi_2O_3 as well as their 1:1 ternary composition, $CuBi_2O_4$ were very recently synthesized using SCS. The entire gamut of composite possibilities, ranging from CuO/$CuBi_2O_4$ composites at one end to $CuBi_2O_4$/Bi_2O_3 at the other, could be derived by tuning the SCS precursor chemistry.[22] Figure 2-7a shows the progressively lighter hue from pure $CuBi_2O_4$, the three composites, culminating in white coloration for pure Bi_2O_3. The corresponding spectral profiles are contained in Figure 2-7b. As the Bi_2O_3 amount increased in the composites, the spectrum progressively blue-shifted (i.e., from visible to the UV wavelength range) towards the Bi_2O_3 end.

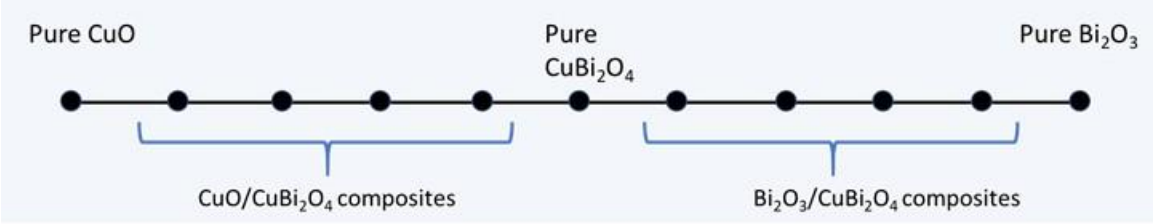

Figure 2-6. Formation of ternary oxides and composites in the Cu-Bi-O system. The line format shows the composition relationships between the ternary compound and its binary oxide components. The make-up of the eight composite mixtures that were studied, is also shown on this diagram.

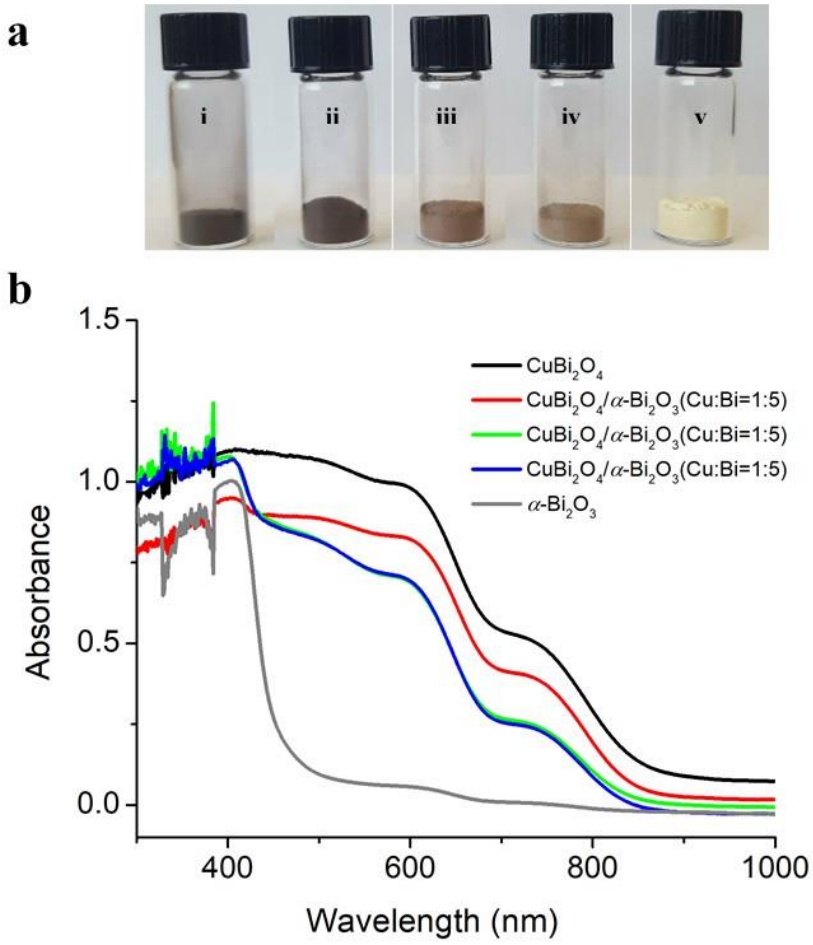

Figure 2-7. (a) Change of color from pure $CuBi_2O_4$ (i) through $CuBi_2O_4/Bi_2O_3$ (ii-iv) to pure Bi_2O_3 (v). (b) UV/visible absorption profiles for pure $CuBi_2O_4$ and Bi_2O_3 and their composites.

The data in Figure 2-7 signal an important hallmark of composites, namely the data signatures from them are a superposition of those corresponding to their components, and two distinct phases can be identified. In contrast, in a solid solution (or an "alloy"), the constituents lose their individual identity via mixing at a molecular level, and resulting in a single-phase material. This happens when the ionic (or atomic) radii of the individual components are within ~15 % of one another such that substitution of one atom (or ion) with another at a given lattice site becomes feasible. Metal alloys are very well known and so are solid solutions of chalcogenides, phosphides,

or arsenides in various technological contexts. Metal oxide solid solutions are less well studied; solid solutions of two ternary oxides are even less commonplace. This is exemplified by the Cu-Fe-Cr-O system where these new materials were prepared via SCS via simple compositional tuning of the precursor mixtures [4]. Both the lattice parameter (Fig. 8) and the optical band gap value systematically varied [4], in line with Vegard's law [56]. For more details, Ref. 4 may be consulted (see, for example, Fig. 5 in it).

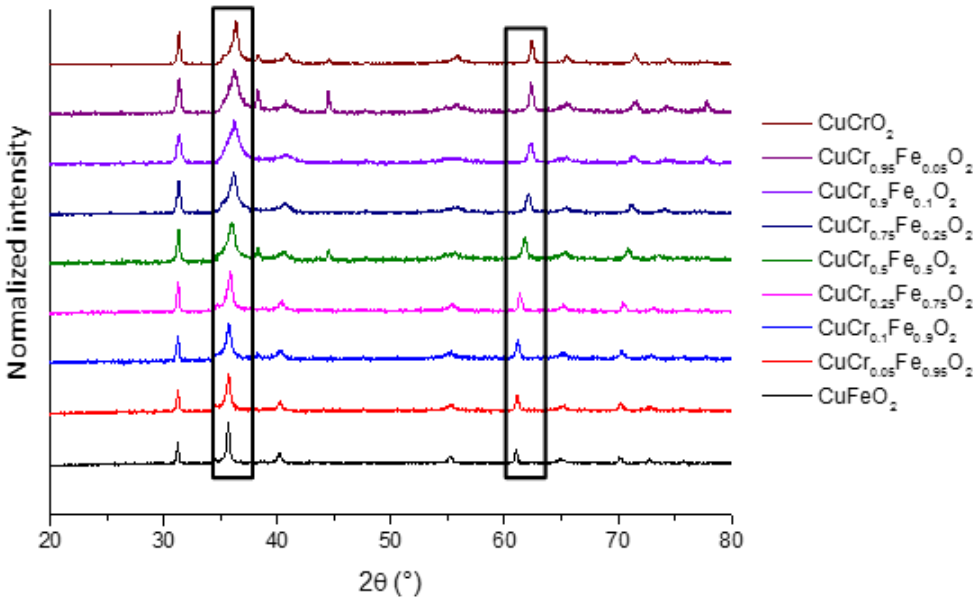

Figure 2-8. XRD profiles of a series of $CuFeO_2$-$CuCrO_2$ solid solutions along with those of the two ternary end members.

The phenomenon of doping largely derives its importance from the microelectronics industry. Doping refers to the *controlled* introduction of trace amounts of a foreign ("dopant") species into the host lattice framework. Like in the solid solution case, doping also results in a single-phase material but unlike in a solid solution, the foreign species are present at very small levels (parts per million or less) such that perturbation of data signatures (e.g., XRD profiles) can only be resolved by careful work. On the other hand, the optoelectronic perturbations of doping are rather

significant (and easily discerned) and lead to their importance in various applications. Many instances of doped metal oxide samples derived from solution combustion exist in the literature, and these will be discussed in the next and final section in this article.

2.6 PHOTOELECTROCHEMICAL AND PHOTOCATALYTIC APPLICATIONS OF COMBUSTION SYNTHESIS-DERIVED COMPLEX OXIDES

In this section, we consider how combustion synthesized complex oxides have fared in photoelectrochemical or photocatalytic applications. The distinction between the two has to do with the underlying thermodynamics of the photoconversion process. In photocatalytic processes, the radiation serves to speed up an intrinsically sluggish spontaneous reaction such as hydrocarbon (e.g., phenol) oxidation or metal ion (e.g., hexavalent chromium) reduction. On the other hand, photoelectrochemical processes such as the splitting of water (into H_2 and O_2) or the reduction of CO_2 are intrinsically non-spontaneous. Table 3 compiles instances wherein combustion-synthesized ternary oxides have been deployed for the photocatalytic degradation of an organic dye. In general, the oxides derived from SCS have a higher surface area than counterparts synthesized from ceramic, solid-state reaction (SSR) routes; and this factor is reflected in the much higher photoactivity of the SCS oxides. Thus the photodegradation of MB using SCS-$CuFe_2O_4$ reached almost 100 % in 30 min while only 25.9 % was degraded using SSR sample in the similar conditions.[23] This can be rationalized on the small particle size (SCS: 100 nm, SSR: 1-3 μm), and consequently, higher surface area of the SCS sample (SCS: 79.3 m^2/g, SSR: 2.2 m^2/g). A similar trend was seen for SCS-Bi_2WO_6 and SCS-$AgBiW_2O_8$ compared to their SSR counterparts.[55]

Table 2-3. Photocatalytic Dye Degradation Using Ternary and Quaternary Oxides Synthesized by SCS

entry no.	oxide	dye	[dye] (mg/l)	catalyst loading (g/l)	light source	irradiation time (h)	degradation (%)	ref
1	$CaFe_2O_4$	MB	3.2	1	500 W Xe lamp with 420 nm cut-off filter	0.75	~100	21
		Rh B	40				~80	
2	$CuFe_2O_4$	MB	40	0.2	natural Sunlight	2	~75	23
		MO	40				~25	
		Phenol	50				~15	
3	$FeAl_2O_4$	MB	10	1	350 W Xe lamp with a 400 nm cut-off filter	2.5	~70	24
		Phenol	-	1		4	~50	
4	$MgAl_2O_4$	MB	10	0.75	350 W Xe lamp with 400 nm cut off	0.75	~85	26
5	$MgFe_2O_4$	MY	20	0.16	350 W Xe lamp	1	~65	27
6	$MnFe_2O_4$	MG	20	0.24	natural sunlight	2	~65	28
7	$NiFe_2O_4$	MB	20	0.25	300W Xe lamp	2	~65	29
8	$ZnFe_2O_4$	Rh B	5	1	natural sunlight	1	~94	31
		CR	10			0.5	~95	
9	$GdFeO_3$	Rh B	4.8	1	500 W Xe lamp	2	~40	32
11	$LaNiO_3$	MO	10	2	400W Xe lamp	5	~75	34
12	$SrTiO_3$	MO	5	0.3	16 W UV lamp	3	~8	35
13	$YFeO_3$	MB	32	1	300 W tungsten halogen lamp	4	~70	36
		Rh B	10	1	175 W metal halide lamp with 420 nm cut-off filter	3	~70	37
14	Bi_2MoO_6	Rh B	10	1	natural sunlight	5	~100	38
15	Bi_2WO_6	Rh B	47.9	1	500W Xe lamp	1.25	~100	39
		MO	32.8	2	450 W tungsten-halogen lamp	4	~65	40
16	$BiVO_4$	MB	639.7	0.05	500 W Xe lamp	3	~70	41
		Rh B	5	1	Xe lamp of 6000K	3	~100	42
		MB	20	2	natural sunlight	1	~100	43

17	$CuWO_4$	MO	16.4	2	400W medium pressure Hg arc	1.33	~100	44
18	$ZnWO_4$	MO	16.4	2	400W medium pressure Hg arc	1	~100	44
		MB	5	0.8	125 W Hg lamp	3	~75	45
19	$CeVO_4$	OG	50	1	125 W high pressure Hg lamp	0.5	~40	46
20	Ag_2WO_4	MO	16.4	2	400 W medium pressure Hg arc	1	~90	44
21	$Bi_2Ce_2O_7$	MG	45	1	Natural sunlight	5	~100	48
22	$Bi_2Ti_2O_7$	MO	16.4	2	150W medium pressure Hg arc	2	~95	49
23	$Gd_2Ti_2O_7$	MO	5	1	four 4 W UV lamps	2	~97	
24	$Nd_2Ti_2O_7$	MO	5	1	four 4 W UV lamps	2	~50	50
25	$Er_2Ti_2O_7$	MO	5	1	four 4 W UV lamps	2	~89	
		RBBR					~70	
26	$Bi_2Zr_2O_7$	IC		1	natural sunlight (800 Wm^{-2})	5	~100	51
		RBBR					~35	
		IC					~60	
27	$ZrMo_2O_8$	Rh B	15	1	125 W high pressure Hg lamp	2	~40	52
28	ZrV_2O_7	Rh B	20	1	125 W high pressure Hg lamp	1	~40	54
29	$AgBiW_2O_8$	MO	16.4	2	400 W medium-pressure Hg arc	6	~95	55

MO	Methyl orange	MG	Malachite green	RBBR	Ramazoline brilliant blue
MB	Methylene blue	CR	Congo red	MY	Metanil yellow
Rh B	Rhodium B	IC	Indigo carmine	OG	Orange green

Composites containing ternary oxides and prepared via SCS, have been tested for their photocatalytic dye degradation capability. Table 4 shows a list of these composites and their dye degradation capability. In all the cases, the composite outperformed its components; compare Columns 8, 9, and 10 in the compilation below.

Table 2-4. Composite Oxides with Improved Dye Degradation Performance

entry no.	composite	dye	[dye] (mg/l)	catalyst loading	light source	irradiation time (h)	degradation (%)			ref
							first component	second component	composite	
1	Bi_2O_3/Bi_2WO_6	Rh B	47.9	1	500W Xe lamp	0.5	~1.5	~61	~98	57
2	$BiVO_4$/BiOCl	Rh B	20	1	300W Xe lamp	3	~8	~38	~85	58
3	CuO/$BiVO_4$	MB	639.7	0.05	500-W Xe lamp	3	-	~28	~47	59
4	$NiFe_2O_4$/BiOBr	Rh B	10	1	300W Xe lamp	2	~31	~46	~96	60
5	$V_2O_5/BiVO_4$	MB	639.7	0.05	500-W Xe lamp	3	~58	~37	~83	61

Data are also available for doped oxides derived from SCS and their use in Photocatalytic dye degradation scenarios; Table 5 collects this corpus of data.

Table 2-5. Photocatalytic Degradation of Organic Dyes Using Doped Ternary Oxides

entry no.	oxide	dopant	dye	[dye] (mg/L)	catalyst loading (g/L)	light source	degradation (%)		ref
							pristine oxide	doped oxide	
1	$MgFe_2O_4$	Ag	MY	20	0.16	350 W Xe-lamp	~65	~89	27
2	$MnFe_2O_4$	Cu	MG	20	0.24	Natural sunlight	~65	~92	28
3	$NiFe_2O_4$	Ag	MB	20	0.25	300 W Xe lamp	~50	~65	29
4	$SrTiO_3$	Pb	MO	5	0.3	16 W UV lamp	~8	~85	35
5	$LaFeO_3$	Mn	MO	100	7.3	Natural sunlight	-	~87	62
6	$ZnWO_4$	Eu	Rh B	4.8	1	Four 4 W UV lamps	~70	-85	63
7	$CeVO_4$	Pd	OG	50	1	125 W high pressure Hg lamp	~40	~65	47
9	ZrV_2O_7	Mo	Rh B	20	1	125 W high pressure Hg lamp	~40	~80	54

In contrast to the rich body of examples of photocatalytic applications, corresponding examples of photoelectrochemical water splitting or carbon dioxide reduction using SCS samples are rather limited. Although $BiVO_4$ is primarily an oxygen evolution photocatalyst, recently, high surface area $BiVO_4$ was synthesized using SCS and reported to be very active toward hydrogen evolution.[43] Thus, nanoparticles of SCS-$BiVO_4$ was able to generate 195.6 mmol/h H_2 from water-ethanol mixture.[43] Pt-modified SCS-$AgBiW_2O_8$ was investigated for the photoelectrochemical conversion of CO_2 and found that to be able to generate syngas from formic acid.[55]

$LaVO_4/BiVO_4$ composites using SCS were evaluated for photoelectrochemical hydrogen generation [46]. Pristine $BiVO_4$ did not show any H_2 while $LaVO_4$ showed a H_2 photogeneration rate of 24 μmol h^{-1}. On the other hand, 20% loading of $BiVO_4$ in $LaVO_4/BiVO_4$ composite showed 45.5 μmol h^{-1}.[46] High resolution TEM images showed intimate physical contact of $LaVO_4$ and $BiVO_4$ in the composite matrix facilitating vectorial charge transport and thus enhancing the photoelectrochemical activity.

In summary, the examples given above in this perspective article ought to have amply demonstrated the virtues of combustion synthesis as a viable technique for the preparation of complex oxides for photoelectrochemical and photocatalytic applications. While serving as a useful review for seasoned practitioners, hopefully, this article will be helpful to new entrants to this field as a sampling of the exciting possibilities ahead in materials discovery and use.

2.7 REFERENCES

1. Kobayashi, Y.; Yoshihiro, T.; Kageyama, H., Property Engineering in Perovskites via Modification of Anion Chemistry. *Annu. Rev. Mater. Sci.* 2018, *48*, 303-326.
2. Kageyama, H.; Hayashi, K.; Maeda, K.; Attfield, J. P.; Hiroi, Z.; Rondinelli, J.; Poeppelmeir, K. R., Expanding Frontiers in Materials Chemistry and Physics with Multiple Anions, *Nature Comm*. 2018, *9*, 772.
3. McCarroll, W. H.; Ramanujachary, K. V. Encycolpaedia of Inorganic Chemistry, Oxides: Solid State Chemistry, Ch. 3, John Wiley & Sons, 2006.
4. Rajeshwar, K.; Hossain, M. K.; Macaluso, R. T.; Janaky, C.; Varga, A.; Kulesza, P. Review-Copper Oxide-Based Ternary and Quaternary Oxides: Where Solid-State Chemistry Meets Photoelectrochemistry. *J. Electrochem. Soc.* 2018, 165, H3192-H3206.
5. Rajeshwar, K.: in Solar Hydrogen Generation: Toward a Renewable Energy Future Rajeshwar, K., McConnell, R. and Licht, S., Eds., New York: Kluwer Academic, Chapter 7, 2008, 167-228.
6. Rajeshwar, K. Solar Energy Conversion and Environmental Remediation Using Inorganic Semiconductor-Liquid Interfaces: The Road Traveled and the Way Forward, *J. Phys. Chem. Lett.* 2011, *2*, 1301-1309.
7. Rajeshwar, K. Photoelectrochemistry and the Environment. *J. Appl. Electrochem*. 1995, *25*, 1067-1082.
8. Bard, A. J.; Fox, M. A. Artificial Photosynthesis: Solar Splitting of Water to Hydrogen and Oxygen. *Acc. Chem. Res*. 1995, *28*, 41-145.

9. Wen, W.; Wu, J.M. Nanomaterials via Solution Combustion Synthesis: a Step Nearer to Controllability. *RSC Adv.* 2014, *4*, 58090-58100.
10. Mukasyan, A.S.; Epstein, P.; Dinka, P. Solution Combustion Synthesis of Nanomaterials. *Proc. Combust. Inst.* 2007, *31*, 1789-1795.
11. Aruna, S.T.; Mukasyan, A.S. Combustion synthesis and Nanomaterials. *Curr. Opin. Solid State Mater. Sci.*, 2008, *12*, 44-50.
12. Varma, A.; Mukasyan, A.S.; Rogachev, A.S.; Manukyan, K.V. Solution Combustion Synthesis of Nanoscale Materials. *Chem. Rev.* 2016, 116, 14493–14586.
13. Li, F.T.; Ran, J.; Jaroniec, M.; Qiao, S.Z. Solution Combustion Synthesis of Metal Oxide Nanomaterials for Energy Storage and Conversion. *Nanoscale*, 2015, *7*, 17590–17610.
14. Hegde, M.S.; Madras, G.; Patil, K.C. Noble Metal Ionic Catalysts. *Acc. Chem. Res.* 2009, *42*, 704–712.
15. González-Cortés, S.L.; Imbert, F.E. Fundamentals, Properties and Applications of Solid Catalysts Prepared by Solution Combustion Synthesis (SCS). *Appl. Catal., A* 2013, *452*, 117-131.
16. Rajeshwar, K.; de Tacconi, N.R. Solution Combustion Synthesis of Oxide Semiconductors for Solar Energy Conversion and Environmental Remediation. *Chem. Soc. Rev.* 2009, *38*, 1984–1998.
17. Patil, K.C.; Hegde, M.S.; Yanu, R.; Aruna, S.T. Chemistry of Nanocrystalline Oxide Materials: Combustion Synthesis, Properties and Applications, Singapore: World Scientific, 2008.
18. Yu, X., Smith, J.; Zhou, N.; Zeng, L.; Guo, P.; Xia, Y.; Alvarez, A.; Aghion, S.; Lin, H.; Yu, J.; Chang, R. P.; Bedzyk, M. J.; Ferragut, R.; Marks, T. J.; Facchetti, A. Spray-Combustion Synthesis: Efficient Solution Route to High-performance Oxide Transistors. *Proc. Natl. Acad. Sci. U.S.A*, 2015, *112*, 3217-3222.
19. Mukasyan, A. S.; Dinka, P. Novel Approaches to Solution-Combustion Synthesis of Nanomaterials. *Int. J. Self-Propag. High-Temp. Synth.* 2007, *16*, 23-35.
20. Akopdzhanyan, T. G.; Borovinskaya, I. P. AlON Powders by SHS under Nitrogen Pressure with $KClO_4$ as a Booster, *Int. J. Self-Propag. High-Temp. Synth.* 2017, *26*, 244-247.
21. Zhang, Z.; Wang, W. Solution Combustion Synthesis of $CaFe_2O_4$ Nanocrystal as a Magnetically Separable Photocatalyst. *Mater. Lett.* 2014, *133*, 212–215.
22. Hossain, M. K.; Samu, G. F.; Gandha, K.; Santhanagopalan, S.; Liu, J. P.; Janáky, C.; Rajeshwar, K. Solution Combustion Synthesis, Characterization, and Photocatalytic Activity of $CuBi_2O_4$ and Its Nanocomposites with CuO and α-Bi_2O_3. *J. Phys. Chem. C*, 2017, 121, 8252–6261.
23. Kumar, A.: Rout, L.; Achary, L. S. K.; Mohanty, S. K.; Dash, P. A Combustion Synthesis Route for Magnetically Separable Graphene Oxide–$CuFe_2O_4$–ZnO Nanocomposites with Enhanced Solar Light-Mediated Photocatalytic Activity. *New J. Chem* 2017, *41*, 10568-10583.
24. Chai, M. J.; Chen, X. M.; Zhao, Y.; Liu, R. H.; Zhao, J.; Li, F. T. Facile Ionic Liquid Combustion Synthesis and Visible-Light Photocatalytic Ability of Mesoporous $FeAl_2O_4$ with High Specific Surface Area. *Chem. Lett.* 2014, *43*, 1743-1745.
25. Mu, H. Y.; Li, F. T.; An, X. T.; Liu, R. H.; Li, Y. L.; Qian, X.; Hu, Y.Q. One-Step Synthesis, Electronic Structure, and Photocatalytic Activity of Earth-Abundant Visible-Light-Driven $FeAl_2O_4$. *Phys. Chem. Chem. Phys.* 2017, *19*, 9392-9401.

26. Li, F. T.; Zhao, Y.; Liu, Y.; Hao, Y. J.; Liu, R. H.; Zhao, D. S. Solution Combustion Synthesis and Visible Light-Induced Photocatalytic Activity of Mixed Amorphous and Crystalline $MgAl_2O_4$ Nanopowders. *Chem. Eng. J.* 2011, *173*, 750-759.
27. Shetty, K.; Prathibha, B. S.; Rangappa, D.; Anantharaju, K. S.; Nagaswarupa, H. P.; Nagabhushana, H.; Prashantha, S. C. Photocatalytic Study for Fabricated Ag Doped and Undoped $MgFe_2O_4$ Nanoparticles. *Mater Today* 2017, *4*, 11764-11772.
28. Meena, S.; Renuka, L.; Anantharaju, K. S.; Vidya, Y. S.; Nagaswarupa, H. P.; Prashantha, S.C.; Nagabhushana, H. Optical, Electrochemical and Photocatalytic Properties of Sunlight Driven Cu Doped Manganese Ferrite Synthesized by Solution Combustion Synthesis. *Mater Today* 2017, *4*, 11773-11781.
29. Zhang, D.; Pu, X., Du; K., Yu, Y.M.; Shim, J. J.; Cai, P.; Kim, S. I.; Seo, H. J. Combustion Synthesis of Magnetic Ag/$NiFe_2O_4$ Composites with Enhanced Visible-Light Photocatalytic Properties. *Sep. Purif. Technol.* 2014, *137*, 82-85.
30. Kelkar, S. A.; Shaikh, P. A.; Pachfule, P.; Ogale, S. B., Nanostructured Cd_2SnO_4 as an Energy Harvesting Photoanode for Solar Water Splitting. *Energy Environ. Sci* 2012, *5*, 5681-5685.
31. Behera, A.; Kandi, D.; Majhi, S. M.; Martha, S.; Parida, K. Facile Synthesis of $ZnFe_2O_4$ Photocatalysts for Decolourization of Organic Dyes Under Solar Irradiation. *Beilstein J. Nanotechnol.* 2018, *9*, 436-446.
32. Li, L.; Wang, X. Self-Propagating Combustion Synthesis and Synergistic Photocatalytic Activity of $GdFeO_3$ Nanoparticles. *J. Sol-Gel Sci.* 2016, *79*, 107-113.
33. Parida, K. M.; Reddy, K. H.; Martha, S.; Das, D. P.; Biswal, N. Fabrication of Nanocrystalline $LaFeO_3$: an Efficient Sol–Gel Auto-Combustion Assisted Visible Light Responsive Photocatalyst for Water Decomposition. *Int. J. Hydrog. Energy*, 2010, 35, 12161-12168.
34. Li, F. T.; Liu, Y.; Sun, Z. M.; Liu, R. H.; Kou, C. G.; Zhao, Y.; Zhao, D.S. Facile Preparation of Porous $LaFeO_3$ Nanomaterial by Self-combustion of Ionic Liquids. *Mater. Lett.*, 2011, *65*, 406-408.
35. Li, Y.; Yao, S.; Wen, W.; Xue, L.; Yan, Y. Sol–Gel Combustion Synthesis and Visible-Light-Driven Photocatalytic Property of Perovskite $LaNiO_3$. *J. Alloys Compd.* 2010, *491*, 560-564.
36. Xue, H.; Li, Z.; Wang, X.; Fu, X. Studies on Nanocrystalline (Sr, Pb)TiO_3 Solid Solutions Prepared via a Facile Self-Propagating Combustion Method. *J. Phys. Chem. Solids*, 2007, *8*, 2326-2331.
37. Wu, L.; Jimmy, C. Y.; Zhang, L.; Wang, X.; Li, S. Selective Self-Propagating Combustion Synthesis of Hexagonal and Orthorhombic Nanocrystalline Yttrium Iron Oxide. *J. Solid State Chem.* 2004, *177*, 3666-3674.
38. Chen, Y.; Yang, J.; Wang, X.; Feng, F.; Zhang, Y.; Tang, Y. Synthesis $YFeO_3$ by Salt-Assisted Solution Combustion Method and Its Photocatalytic Activity. *J. Ceram. Soc. Jpn.* 2014, *122*, 146-150.
39. Saha, D.; Madras, G.; Row, T.G. Solution Combustion Synthesis of γ (L)-Bi_2MoO_6 and Photocatalytic Activity Under Solar Radiation. *Mater. Res. Bull.* 2011, *46*, 1252-1256.
40. Zhang, Z.; Wang, W.; Shang, M.; Yin, W. Low-Temperature Combustion Synthesis of Bi_2WO_6 Nanoparticles as a Visible-Light-Driven Photocatalyst. *J. Hazard. Mater.* 2010, *177*, 1013-1018.

41. Timmaji, H.K.; Chanmanee, W.; De Tacconi, N. R.; Rajeshwar, K. Solution Combustion Synthesis of $BiVO_4$ Nanoparticles: Effect of Combustion Precursors on the Photocatalytic activity. *J. Adv. Oxid. Technol.* 2011, *14*, 93-105.
42. Jiang, H. Q.; Endo, H.; Natori, H.; Nagai, M.; Kobayashi, K. Fabrication and Photoactivities of Spherical-Shaped $BiVO_4$ Photocatalysts through Solution Combustion Synthesis Method. *J. Eur. Ceram. Soc* 2008, *28*, 2955-2962.
43. Pérez, U. G.; Sepúlveda-Guzmán, S.; Martínez-de la Cruz, A.; Méndez, U. O. Photocatalytic Activity of $BiVO_4$ Nanospheres Obtained by Solution Combustion Synthesis Using Sodium Carboxymethylcellulose. *J. Mol. Catal. A: Chem.* 2011, *335*, 169- 175.
44. Nagabhushana, G. P.; Nagaraju, G.; Chandrappa, G. T. Synthesis of Bismuth Vanadate: Its Application in H_2 Evolution and Sunlight-Driven Photodegradation. *J. Mater. Chem. A* 2013, *1*, 388-394.
45. Thomas, A.; Janáky, C.; Samu, G. F.; Huda, M. N.; Sarker, P.; Liu, J. P.; Van Nguyen, V.; Wang, E. H.; Schug, K. A.; Rajeshwar, K. Time-and Energy-Efficient Solution Combustion Synthesis of Binary Metal Tungstate Nanoparticles with Enhanced Photocatalytic Activity. *ChemSusChem* 2015, *8*, 1652-1663.
46. Eranjaneya, H.; Chandrappa, G. T. Solution Combustion Synthesis of Nano $ZnWO_4$ Photocatalyst. *Trans. Indian Ceram. Soc.* 2016, *75*, 133-137.
47. Veldurthi, N. K.; Eswar, N. K.; Singh, S. A.; Madras, G. Cocatalyst Free Z-Schematic Enhanced H_2 Evolution over $LaVO_4/BiVO_4$ Composite Photocatalyst using Ag as an Electron Mediator. *Appl. Catal. B* 2018, *220*, 512-523.
48. Bellakki, M.B.; Baidya, T.; Shivakumara, C.; Vasanthacharya, N.Y. Hegde, M.S.; Madras, G. Synthesis, Characterization, Redox and Photocatalytic Properties of $Ce_{1-x}Pd_xVO_4$ ($0 \leq x \leq 0.1$). *Appl. Catal., B* 2018, *84*, 474-481.
49. Saha, D.; Madras, G.; Row, T. N. G. Synthesis and Structure of $Bi_2Ce_2O_7$: a New Compound Exhibiting High Solar Photocatalytic Activity. *Dalton Trans.* 2012, 41, 9598-9600.
50. Samu, G. F.; Veres, Á.; Endrődi, B.; Varga, E.; Rajeshwar, K.; Janáky, C. Bandgap-Engineered Quaternary $M_xBi_{2-x}Ti_2O_7$ (M: Fe, Mn) Semiconductor Nanoparticles: Solution Combustion Synthesis, Characterization, and Photocatalysis. *Appl. Catal., B*, 2017, *208*, 148-160.
51. Xue, H.; Zhang, Y.; Xu, J.; Liu, X.; Qian, Q.; Xiao, L.; Chen, Q. Facile One-Pot Synthesis of Porous $Ln_2Ti_2O_7$ (Ln= Nd, Gd, Er) with Photocatalytic Degradation Performance for Methyl Orange. *Catal Commun* 2014, *51*, 72-76.
52. Sharma, V. M.; Saha, D.; Madras, G.; Row, T. G. Synthesis, Structure, Characterization and Photocatalytic Activity of $Bi_2Zr_2O_7$ Under Solar Radiation. *RSC Adv.* 2013, *3*, 18938-18943.
53. Sahoo, P. P.; Madras, G.; Guru Row, T. N. Synthesis, Characterization, and Photocatalytic Properties of $ZrMo_2O_8$. *J. Phys. Chem. C* 2009, *113*, 10661-10666.
54. Kormányos, A.; Thomas, A.; Huda, M. N.; Sarker, P.; Liu, J. P.; Poudyal, N.; Janáky, C.; Rajeshwar, K. Solution Combustion Synthesis, Characterization, and Photoelectrochemistry of $CuNb_2O_6$ and $ZnNb_2O_6$ nanoparticles. *J. Phys. Chem. C* 2016, *120*, 16024-16034.
55. Sahoo, P.P.; Sumithra, S.; Madras, G.; Guru Row, T. N. Synthesis, Structure, Negative Thermal Expansion, and Photocatalytic Property of Mo Doped ZrV_2O_7. *Inorg. Chem.* 2011, *50*, 8774-8781.

56. de Tacconi, N. R.; Timmaji, H. K.; Chanmanee, W.; Huda, M. N; Sarker, P.; Janáky, C.; Rajeshwar, K. Photocatalytic Generation of Syngas Using Combustion-Synthesized Silver Bismuth Tungstate. *ChemPhysChem* 2012, *13*, 2945-2955.
57. Vegard, L. Die Konstitution der Mischkristalle und die Raumfüllung der Atome, *Zeitschrift Für Phys*. 1921, *5*, 17–26.
58. Hao, Y. J.; Li, F. T.; Chen, F.; Chai, M. J.; Liu, R. H.; Wang, X. J. In Situ One-Step Combustion Synthesis of Bi_2O_3/Bi_2WO_6 Heterojunctions with Notable Visible Light Photocatalytic Activities. *Mater. Lett.* 2014, *124*, 1-3.
59. Lv, D.; Zhang, D.; Pu, X.; Kong, D.; Lu, Z.; Shao, X.; Ma, H.; Dou, J. One-Pot Combustion Synthesis of $BiVO_4$/BiOCl Composites with Enhanced Visible-Light Photocatalytic Properties. *Sep. Purif. Technol.* 2017, *174*, 97-103.
60. Jiang, H.Q.; Endo, H.; Natori, H.; Nagai, M.; Kobayashi, K. Fabrication and Efficient Photocatalytic Degradation of Methylene Blue over CuO/$BiVO_4$ Composite under Visible-Light Irradiation. *Mater. Res. Bull.* 2009, *44*, 700-706.
61. Lv, D.; Zhang, D.; Liu, X.; Liu, Z.; Hu, L.; Pu, X.; Ma, H.; Li, D.; Dou, J. Magnetic $NiFe_2O_4$/BiOBr Composites: One-Pot Combustion Synthesis and Enhanced Visible-Light Photocatalytic Properties. *Sep. Purif. Technol.* 2016, *158*, 302-307.
62. Jiang, H.; Nagai, M.; Kobayashi, K. Enhanced Photocatalytic Activity for Degradation of Methylene Blue over $V_2O_5/BiVO_4$ Composite. *J. Alloys Compd.* 2009, *479*, 821-827.
63. Wei, Z. X.; Wang, Y.; Liu, J. P.; Xiao, C. M.; Zeng, W. W. Synthesis, Magnetization and Photocatalytic Activity of $LaFeO_3$ and $LaFe_{0.5}Mn_{0.5-x}O_{3-\delta}$. *Mater. Chem. Phys.* 2012, *136*, 755-761.
64. Dong, T.; Li, Z.; Ding, Z.; Wu, L.; Wang, X.; Fu, X. Characterizations and Properties of Eu^{3+}-Doped $ZnWO_4$ Prepared via a Facile Self-Propagating Combustion Method. *Mater. Res. Bull.* 2008, *43*, 1694-1701.

CHAPTER 3

SOLUTION COMBUSTION SYNTHESIS, CHARACTERIZATION, AND PHOTOCATALYTIC ACTIVITY OF $CuBi_2O_4$ AND ITS NANOCOMPOSITES WITH CuO AND α-Bi_2O_3

ABSTRACT

The ternary compound, $CuBi_2O_4$, a 1:1 stoichiometric derivative of the two component oxides: CuO and Bi_2O_3, has attracted attention from the solar water splitting and photocatalysis communities as a *p*-type semiconductor responsive to visible light. This study demonstrates that solution combustion synthesis (SCS) can be used to prepare powders not only of this compound but also nanocomposites with either CuO or Bi_2O_3 in excess. This was simply done by tuning the SCS precursor mixture composition. The synthesized crystalline samples were characterized by powder X-ray diffraction (with Rietveld refinement for phase purity), diffuse reflectance UV-visible spectroscopy, electron microscopy, and photoelectrochemical (PEC) techniques. The band structure and photoactivity of these oxides were probed by linear sweep voltammetry and by measuring their photoaction spectra (internal photon-to-electron conversion efficiency vs. wavelength). The photoactivity (attributed to hydrogen evolution and CO_2 photoreduction) was considerably improved in the $CuO/CuBi_2O_4$ nanocomposites because of electron transport of the photogenerated charge carriers between the $CuBi_2O_4$ and the CuO nanoparticles.

3.1 INTRODUCTION

Utilizing sunlight via its photoelectrochemical (PEC) conversion to fuels/chemicals is an eminently-attractive strategy for attacking energy supply and environmental concerns associated with the use of fossil fuels.[1] Nonetheless, some four decades of R&D have still not identified a "magic bullet" semiconductor that simultaneously satisfies all of the disparate requirements for efficient and sustained generation of solar fuels/chemicals.[2] Similar performance issues beset the use of semiconductors for environmental pollution abatement (i.e., the so-called photocatalytic (PC) applications, Ref. 3). In recent years, *p*-type oxide semiconductors have been studied as photocathodes for driving various reductive processes such as H_2 evolution and CO_2 conversion.[4,5] Copper-containing oxides are particularly relevant for the above applications and ternary oxides such as $CuFeO_2$,[6-8] $CuRhO_2$,[9] $CuWO_4$,[10] $CuFe_2O_4$,[11] $CuNb_2O_6$,[12] and $Cu_3Nb_2O_8$[13] have been examined as possible candidates. The present study focuses on $CuBi_2O_4$, a semiconductor material that has captured recent attention since its combinatorial discovery in 2007.[14]

As Table 3-1 shows, there have been many studies on this *p*-type semiconductor since then but none that uses solution combustion synthesis (SCS). This previous body of work also reveals that this oxide converts incident photons much more efficiently when used in conjunction with another oxide semiconductor, especially an *n*-type semiconductor. Thus, we demonstrate below that SCS is versatile for exploring the entire composition space from CuO on the one end to Bi_2O_3 at the other. [An early study[35] shows that in the CuO-Bi_2O_3 phase diagram, $CuBi_2O_4$, i.e., the 1:1 stoichiometry of the two binary components, is the only ternary compound that is stable.] Specifically, tuning of the precursor SCS mixture is shown below to enable the facile synthesis of not only $CuBi_2O_4$ but also its nanocomposites with CuO or Bi_2O_3 by using Cu-rich or Bi-rich precursor mixtures, respectively.

In the search for time- or energy-efficient oxide preparation routes, SCS has emerged as a popular candidate. Unlike the solid-state or solution-based (e.g., sol-gel) methods that have long been deployed for preparing oxides, SCS features very short reaction times. Further, no special equipment is required, and most importantly from a solid-state chemistry perspective, the host oxide can be doped or nanocomposites prepared by simple changes of the precursor fuel or mixture composition. Review articles have summarized the surging popularity of this synthesis approach within the solar fuels and photocatalysis communities.[36-38]

It is underlined that, notwithstanding the multitude of studies listed in Table 3-1, this study represents the first instance where SCS has been used to prepare $CuBi_2O_4$ or its nanocomposites with CuO or Bi_2O_3. Further, some benefits of nanostructured oxide heterojunctions as demonstrated below for PEC CO_2 reduction, are exemplified by the CuO or Bi_2O_3 system.

Table 3-1. Previous Studies on $CuBi_2O_4$ or Its Nanocomposites with Other Oxides

entry no.	preparation method	comments	application	ref
1	solid-state reaction	nanocomposites with WO_3 also studied	photocatalytic (PC) oxidation of acetaldehyde	14
2	solid-state reaction followed by ball-milling	heterojunctions with *n*-TiO_2 also studied.	PC reduction of Cr(VI) or oxidation of methyl orange dye	15
3	thin film photocathodes prepared by electrodeposition	film unstable in acid but stable in basic electrolyte under constant illumination.	PEC hydrogen generation	16
4	solid-state reaction followed by milling (as in Entry 2 above) followed by ion exchange for SrO insertion	nanoscale powder containing 20 mass % SrO was studied	PC destruction of Congo Red dye	17

5	hydrothermal	material obtained as nanosheets	PC oxidation of methylene blue	18
6	solid-state reaction	oxide combined with $BiVO_4$ by mixing two powders and heat treating at 150 C for 3 h	PC oxidation of acetaldehyde	19
7	low-temperature solution process	variety of morphologies seen.	PC degradation of methylene blue	20
8	a dispenser and scanner system developed to screen Cu-Bi-M oxide arrays for comparison with the Cu-Bi-oxide	Bi-Ag-Cu oxide seen to have 4 times higher photocurrent than the Cu-Bi-oxide	PEC hydrogen generation	21
9	hydrothermal	DFT calculations also performed in study	PC hydrogen generation with sacrificial electron donor	22
10	hydrothermal	hierarchically-structured composites studied	PC generation of sulfate radicals from peroxymonosulfate for organic pollutant removal and disinfection	23
11	anodic co-electrodeposition	deposition on FTO substrate	PEC hydrogen generation	24
12	solution growth in an ethanol-water mixture	both spherulite and nanorods of oxides synthesized along with CuO nanosheet composites	PEC hydrogen generation	25
13	$CuBi_2O_4$ layer grown on CuO and then platinized	FTO substrate used	PEC hydrogen generation	26
14	solvothermal growth	hybrid with graphene oxide	PC degradation of methylene blue and methyl orange dyes	27
15	hydrothermal	self-assembled nanocolumn arrays of oxide obtained	activation of persulfate and peroxymonosulfate for 1H-benzotriazole removal	28
16	ball-milling	composite with multi-walled carbon nanotube (MWCNT)	PC degradation of methyl orange	29
17	grinding followed by thermal anneal	composites with $NaTaO_3$	PC degradation of methylene blue	30

18	electrodeposition	FTO support with a gold transition layer	PEC hydrogen generation	31
19	electrodeposition	Ag doping also studied	PEC hydrogen generation	32
20	hydrothermal	composites with Co or Cu studied	sulfanilamide removal via peroxymonosulfate activation	33
21	drop-casting	limitations for use in PEC water splitting discussed	PEC hydrogen generation	34

3.2 EXPERIMENTAL SECTION

3.2.1 Materials

Copper nitrate hemi (pentahydrate) [$Cu(NO_3)_2 \cdot 2.5\ H_2O$ (Alfa Aesar)] and bismuth nitrate pentahydrate – [$Bi(NO_3)_3 \cdot 5\ H_2O$ (Alfa Aesar)] were used as the metal sources as well as the oxidizing species in the reaction. Urea and hexamethylenetetramine (HMT) were used as fuel. Nitric acid (Alfa Aesar) was used to dissolve bismuth nitrate. Double-distilled water (Corning Megapure) was used to prepare all the solutions. All the chemicals were used as received without further purification.

3.2.2 Solution Combustion Synthesis

Stoichiometric amounts of copper nitrate and fuel were dissolved in water along with a stoichiometric amount of bismuth nitrate in 2.0 M nitric acid. The two solutions were mixed together with the final metal concentrations of copper and bismuth being 0.18 M and 0.36 M, respectively. Then the solutions were homogenized and transferred to a pre-heated furnace at 300 °C for 5-8 min. Once they were dehydrated, spontaneous ignition produced gases, leaving behind a foamy mass. The variant Cu/Bi mole ratios used in this study are identified in Table 3-2. Initial screening used different fuel-to-oxidizer ratios; the stoichiometric (1:1) composition produced the

most optimal results such that only this case is considered below (see also Table 3-2). As-prepared samples were ground in mortar and pestle and annealed at different temperatures to remove any carbonaceous residue as well as to improve sample crystallinity.

Table 3-2. Sample Identification with Various Cu/Bi Mole Ratios and Fuels Used

sample identification	Cu/Bi mole ratio in precursor mixture	fuel	fuel-to- oxidizer ratio
$CuBi_2O_4$ (U)	1 : 2	urea	1
$CuBi_2O_4$ (HMT)	1 : 2	hexamethylenetetramine (HMT)	1
CuO/ $CuBi_2O_4$ (5:1)	5 : 1	urea	1
CuO/ $CuBi_2O_4$ (10:1)	10 : 1	urea	1
CuO/ $CuBi_2O_4$ (10:1)	15 : 1	urea	1
α-Bi_2O_3/$CuBi_2O_4$ (1:5)	1 : 5	urea	1
α-Bi_2O_3/$CuBi_2O_4$ (1:10)	1 : 10	urea	1
α-Bi_2O_3/$CuBi_2O_4$ (1:15)	1 : 15	urea	1
CuO	1 : 0	urea	1
α-Bi_2O_3	0 : 1	urea	1

3.2.3 Photoelectrode Preparation

The metal oxide samples were spray-coated from isopropanol solutions (10 mg cm^{-3} concentration) on Sn-doped indium oxide (ITO) glass electrodes with different loadings and were used as working electrodes. Prior to coating, the ITO electrodes were sequentially sonicated for 5 min in acetone, 2-propanol, and finally deionized water. This step was followed by O_2 plasma treatment of the cleaned electrodes for 15 min. After the coating procedure the electrodes were

subjected to a sintering step for 1 h at 350 °C to ensure the adherence of the film to the electrode surfaces.

3.2.4 Physical Characterization

Simulation of combustion reactions was performed using thermogravimetric analysis/differential scanning calorimetry (TGA/DC) in a TA Instruments model Q600 instrument. Homogeneous mixtures of precursor and fuel were placed in an alumina crucible in air atmosphere with a gas flow rate of 100 ml/min at a heating rate of 10 °C/min. Powder X-ray diffraction (XRD) was carried out on a Siemens D-500 instrument within a 2θ range of 10−70° using Cu Kα source (λ = 1.5406 Å). Rietveld refinement was performed using MDI Jade 9 software with model structures culled from the JCPDS database. Pseudo-Voigt peak profile function with displacement was used to fit the experimental profile allowing for any deviation from the model structure. Average crystallite size of the materials was estimated using the Scherrer equation.

UV-visible diffuse reflectance spectroscopy (DRS) was performed on a Perkin Elmer Lambda 35 spectrophotometer equipped with an integrating sphere. Brunauer-Emmett-Teller (BET) surface area values were measured using nitrogen in a Micromeritics TriStar II 3020 instrument at a relative pressure range of P/P_0 = 0.05-0.3. A Hitachi S4800 FE-SEM instrument was used for scanning electron microscopy. High-resolution transmission electron microscopy (HR-TEM) was performed on a Hitachi H-9500 instrument at various magnifications. The samples were prepared by evaporating isopropanol dispersions on carbon-coated copper grids. An acceleration voltage of 300 kV was used. A Gatan digital micrograph was used to perform fast Fourier transforms (FFT) thereby affording the *d*-spacing for the lattice planes.

3.2.5 Photoelectrochemistry Measurements

All photoelectrochemical (PEC) measurements were carried out on a CH Instruments (CHI720C) instrument in a classical one-compartment, three-electrode electrochemical cell. A Ag/AgCl/3M KCl electrode and Pt wire were used as the reference electrode and counterelectrode respectively. A 400 W Xe-arc lamp (Newport) was used as the radiation source. The electrochemical cell was place 20 cm away from the radiation source. Photovoltammograms were performed in 0.1 M Na_2SO_4 as electrolyte with a potential scan of 1 mVs^{-1} sweep rate. Incident photon-to-electron conversion efficiency (IPCE) measurements were performed on a Newport Quantum Efficiency Measurement System (QEPVSI-B) in a single-compartment, three electrode quartz electrochemical cell. The wavelength range was either 300-1100 nm or 300-800 nm (resolution, $\Delta\lambda = 10$ nm) as indicated below. The incident photon-to electron-conversion efficiency (IPCE)-wavelength profiles (photoaction spectra) were recorded in a 0.5 M $NaHCO_3$ solution saturated with CO_2 at -0.3 V applied bias. For these measurements, photoelectrodes with equal loadings were chosen. All measurements were performed at ambient temperature (20 ± 2 °C).

3.3 RESULTS AND DISCUSSION

3.3.1 Synthesis

In the preliminary phases of this study, $CuBi_2O_4$ was synthesized using two fuels namely urea and hexamethylenetetramine (HMT). The stoichiometric combustion reactions are represented by Eqs 1 and 2.

$$3\ Cu(NO_3)_2{\cdot}2.5H_2O + 6\ Bi(NO_3)_3{\cdot}5\ H_2O + 20\ H_4N_2CO = 3CuBi_2O_4 + 32\ N_2 + 20\ CO_2 + 77.5\ H_2O \quad (1)$$

$$9\ Cu(NO_3)_2{\cdot}2.5H_2O + 18\ Bi(NO_3)_3{\cdot}5\ H_2O + 10\ C_6H_{12}N_4 = 9\ CuBi_2O_4 + 56\ N_2 + 60\ CO_2 + 172.5\ H_2O \quad (2)$$

A fuel/oxidizer ratio of 1 was used for all cases (Table 3-2), as it was presumed that combustion of this stoichiometric reaction mixture would give out maximum heat.[31] The phase diagram of

binary CuO and Bi_2O_3 showed a single ternary phase of $CuBi_2O_4$ at a stoichiometric mole ratio (Cu/Bi) of 1:2; a stoichiometric mole ratio of Cu and Bi in the precursor mixture was accordingly used to synthesize single-phase $CuBi_2O_4$.

To better understand the decomposition process of the precursor mixture using the two different fuels, a TGA-DSC simulation was performed using both fuels as shown in Figure 3-1. In this exercise, the sample contains a mixture of the fuel and the oxidizer just like in SCS. Figure 3-1a shows various regions of the decomposition process using urea as a fuel. The TGA curve shows weight loss in four regimes over a broad range of temperatures. The first weight loss in the range of 100-200 °C (Figure 3-1a, Regime 1) can be assigned to the elimination of water followed by decomposition of the precursor mixture from 150-200 °C (Figure 3-1a, Regime II)) according to eqns. 3 and 4:[39,40]

$$2\ Cu(NO_3)_2 \cdot 3H_2O = Cu_2(OH)_3NO_3 + 3\ H_2O + HNO_3 \quad (3)$$

$$6\ Bi(NO_3)_3 \cdot 5\ H_2O = (BiONO_3)_6 .3\ H_2O + 27\ H_2O + 12\ NO_2 + 3O_2 \quad (4)$$

Combustion of the precursor mixture appears with an appreciable amount of heat generation at 200-300 °C. Finally, removal of carbonaceous combustion residue occurs in the range, 300-550 °C (Figure 3-1a, Regime IV). An exothermic peak at 261 °C can be assigned as the ignition temperature. Figure 3-1b, for HMT as the fuel, shows mass change in four regimes: first elimination of water at 100-150 °C and then decomposition culminating in combustion of the precursor mixture. This is followed by the removal of remaining carbonaceous materials. An exothermic peak at 265 °C can be assigned to the ignition temperature.

The percent mass loss during combustion reactions was estimated from the TGA traces after the dehydration stage and was~55 % for urea as fuel and ~50 % using HMT (Table 3-3). After combustion, there was a gradual mass change up to ~500 °C in both cases, believed to be due to the removal of remaining carbonaceous materials. The overall mass loss from region II-region IV appear as 66% for urea and 59% for HMT, and these results correspond well with the theoretical mass loss values of 66 % and 60 % using urea and HMT respectively as calculated from Eqns. 1 and 2 above.

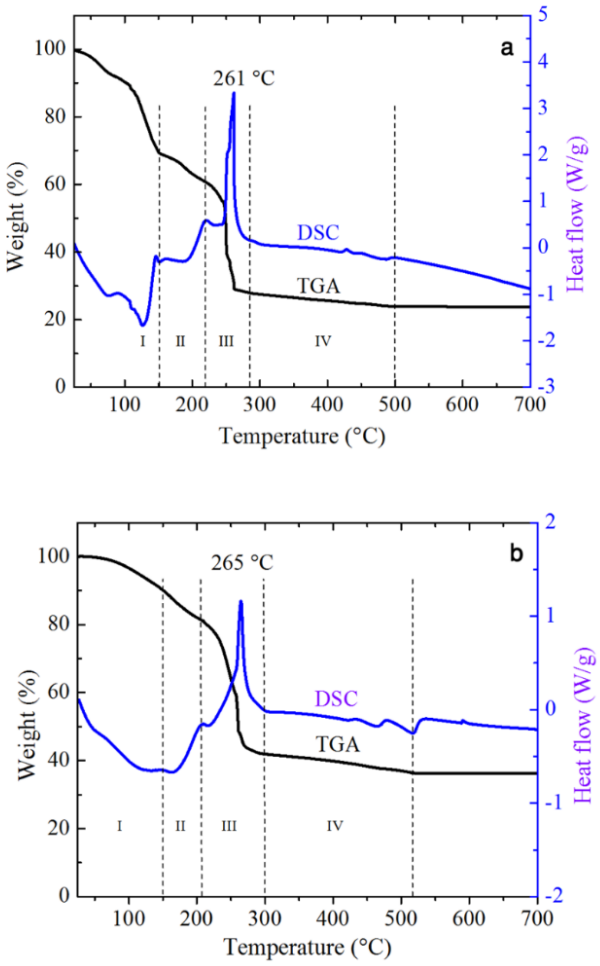

Figure 3-1. Simulation of solution combustion synthesis via TGA-DSC analyses for the two fuels: (a) urea and (b) HMT. Refer to experimental section for sample/precursor mixture details.

Table 3-3. Combustion Properties and TGA Data with Respect to the Two Fuels

fuel	ignition temperature (°C)	type of combustion	% mass loss during combustion (regime II)	% mass loss up to 500 °C (regimes II-IV)
urea	261	volume combustion	~ 55	~ 66
HMT	265	smoldering combustion	~ 50	~ 59

The type of combustion reaction using urea and HMT were different: Urea as a fuel showed volume combustion whereas HMT exhibited the characteristics of smoldering combustion.[38] Notably and as expected, there was no combustion reaction without fuel in the precursor mixture (see Figure A-S1 in Supporting Information).

3.3.2 Structural and Morphological Characterization.

Effect of anneal temperature. As-synthesized samples were annealed to enhance the degree of crystallinity as well as to remove any carbonaceous residue left after the combustion reaction. The effect of different annealing temperatures on as-synthesized samples is presented in Figures 2-2 and A-S2 using urea and HMT as fuel, respectively. The two samples are designated as $CuBi_2O_4$ (U) and $CuBi_2O_4$ (HMT), respectively. When the as-synthesized $CuBi_2O_4$ (U) was annealed at 400 °C for 1 h, peaks correspond to the kusachiite phase (PDF # 01-071-5101) started to develop, along with bismuth oxide phase as impurity, and at 600 °C, almost a single phase of $CuBi_2O_4$ was formed. Presumably, at a high temperature, ion mobility is high enough for single-phase $CuBi_2O_4$ growth without segregation of Bi_2O_3 phase. Rietveld refinement showed good agreement with the reference kusachiite XRD pattern (see Figure A-S3 in Supporting Information). On the other hand, samples prepared using HMT required thermal anneal at a higher temperature, 700 °C, for 1 h to secure the pure phase of crystalline material (Figure A-S3).

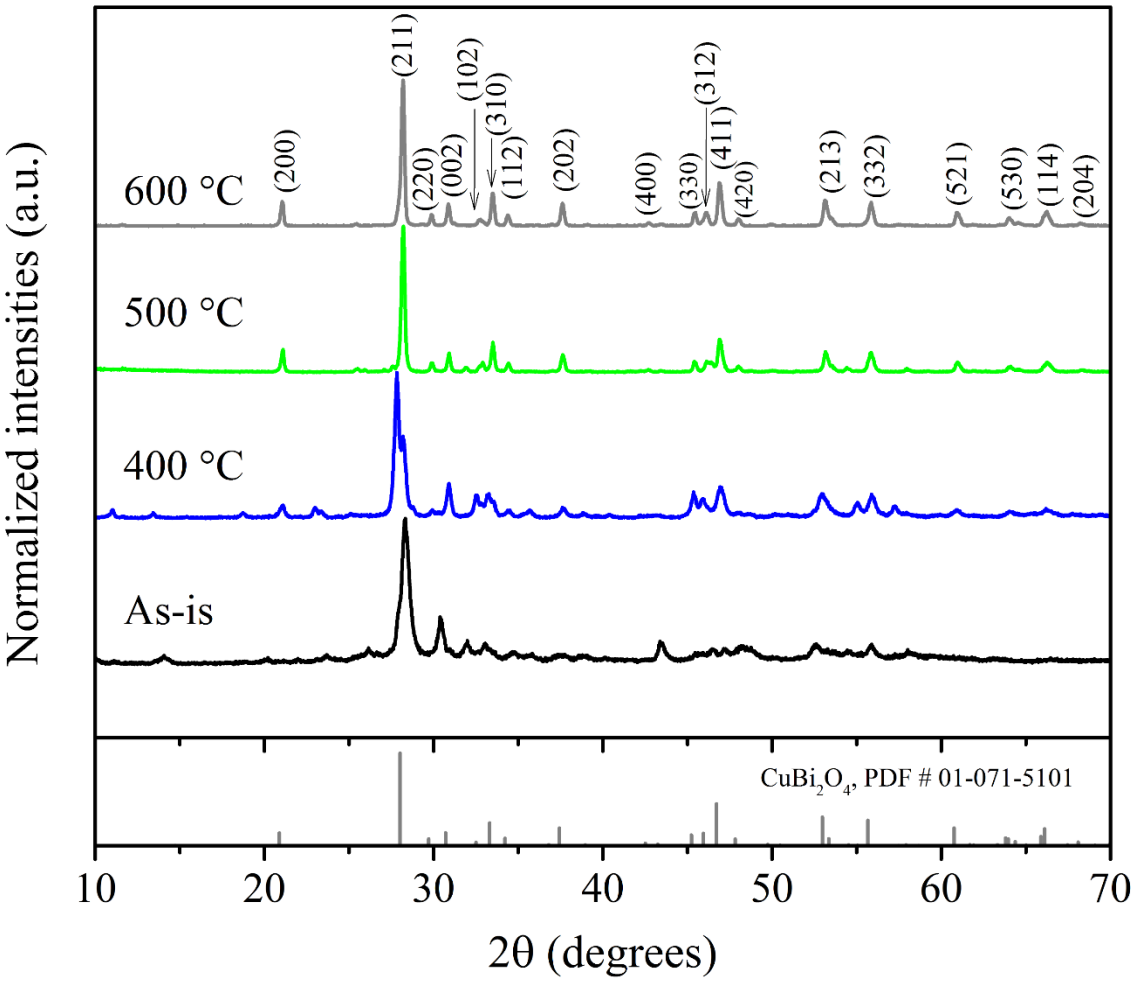

Figure 3-2. Effect of anneal temperature on the purity and the crystallinity of as-is $CuBi_2O_4$ (U). A standard XRD pattern of kusachiite, $CuBi_2O_4$ (PDF# 01-071-5101), is also shown for comparison.

The BET surface area and crystallite size of as-synthesized and annealed samples are shown in Table 3-4. The crystallite sizes of the annealed samples were found to be 35 nm and 41 nm using urea and HMT as fuel, respectively. However, the BET surface area of annealed $CuBi_2O_4$ (U) was 1.9 m^2g^{-1}, a value that was higher than for annealed $CuBi_2O_4$ (HMT) with 0.6 m^2g^{-1}. Annealed samples always showed lower surface areas than as-synthesized counterparts, a trend attributed to

sintering of the particles after thermal anneal. Since urea as a fuel produced samples with higher surface area, only samples derived from urea are discussed hereafter. The rather low

Table 3-4. Calculated Average Crystallite Sizes (from Scherrer XRD analyses) and BET Surface Areas for As-synthesized and Annealed Samples for the Two Fuels

sample	BET Surface area ($m^2 g^{-1}$)		average crystallite size (nm)	
	as-synthesized	annealed	as-synthesized	annealed
$CuBi_2O_4$ (U)	12.5	1.9[a]	8 ± 3	35 ± 2
$CuBi_2O_4$ (HMT)	6.6	0.6[a]	9 ± 2	41 ± 2

a. These values are only approximate since N_2-based BET model analyses are not reliable below 5 m^2g^{-1}, c.f., Ref. 41.

values of the specific surface area and the large particle sizes will become relevant when the PEC and photocatalytic perfomance of these samples are discussed below. At this juncture, it is merely noted that benchmark photocatalysts such as Degussa TiO_2 have much higher surface areas in the ~55 m^2g^{-1} range. Even other samples previously derived from SCS in our laboratories have much higher surface areas; for example, silver bismuth tungstate.[42] Clearly, the combustion characteristics and subsequent particle sintering conspire to produce a non-optimal morphology for the $CuBi_2O_4$ samples.

Representative TEM images of as-synthesized $CuBi_2O_4$ (Figure 3-3a) showed the porous nature of the material. However, after annealing at 600 °C (Figure 3-3b), the porosity decreased with concomitant increase in the particle size. This trend lends credence to the above interpretation for the lowering of surface area (cf., Table 3-4). Figure 3-3d shows the lattice fringes for $CuBi_2O_4$ (110) with a *d*-spacing of 0.600 nm which corresponds to the (110) orientation of the crystallites. An SEM image of annealed sample showed irregular morphology. The corresponding EDS scan

(See Figure A-S4 in Supporting Information) showed the elements present in the samples and confirmed the purity with an elemental ratio of Cu/Bi in the compound: 1:1.97.

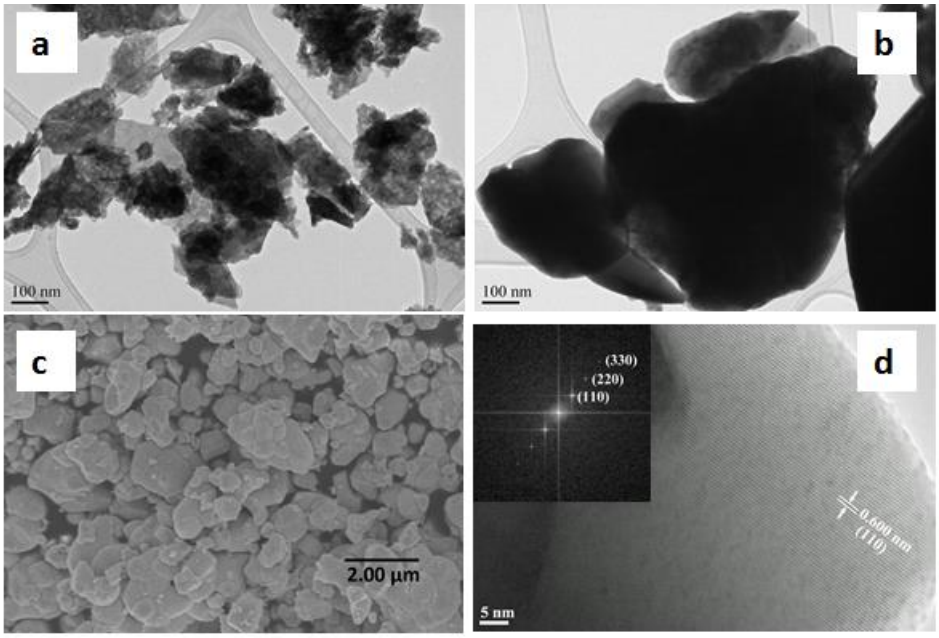

Figure 3-3. TEM images of $CuBi_2O_4$: (a) as-synthesized, (b) annealed at 600 °C for 1 h, (c) SEM image of $CuBi_2O_4$ annealed at 600 °C for 1 h, (d) HR-TEM and lattice image. The inset in frame d contains the corresponding numerical FFT pattern.

Effect of Cu/Bi Ratio. The phase diagram of CuO and Bi_2O_3 predicts that nonstoichiometric Cu/Bi mole ratios would lead to the formation of composites with excess of one binary oxide phase or the other. In the SCS procedure, then the expectation is that an excess of Cu precursor will lead to the formation of a composite with excess of the CuO component while an excess of Bi precursor leads to the formation of composite with excess Bi_2O_3. Accordingly, Figure 3-4 shows XRD patterns for CuO and $CuBi_2O_4$ composites with varying ratios and pure CuO at the extreme. Corresponding reference JCPDS files are also shown for the respective oxides. The XRD patterns show that the ratio of CuO increases with increasing mole ratio of Cu in the precursor solution.

Rietveld refinement of XRD data confirmed the two compounds and their corresponding compositions (Figure A-S5). Figure A-S6 compares the composition of the two phases as deduced from the Rietveld analyses with that expected from the amounts used in the precursor mixture. The agreement was satisfactory in all the three sample cases studied. Further results are contained in the Supplemental Information (Table A-S1).

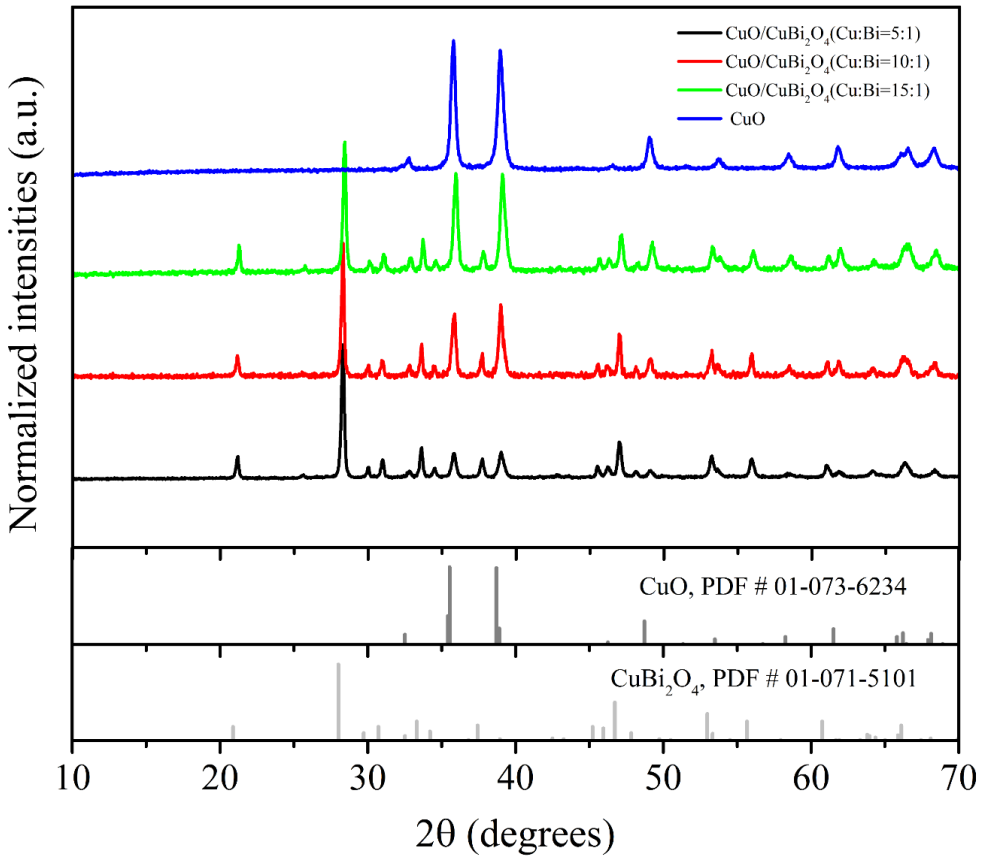

Figure 3-4. XRD patterns for $CuO/CuBi_2O_4$ nanocomposites with varying Cu:Bi ratios. Standard XRD patterns for kusachiite (PDF# 01-071-5101) and tenorite (PDF# 01-073-6234) are also shown below for comparison.

Figure 3-5a shows the SEM image of $CuO/CuBi_2O_4$ (Cu/Bi = 15:1) nanocomposite showing an irregular morphology from agglomeration of the nanoparticles. The HR-TEM images (Figures 3-5b and c) showed lattice fringes with *d*-spacings of 0.424 nm and 0.274 nm corresponding to the CuO (200) and $CuBi_2O_4$ (110) orientations, respectively.

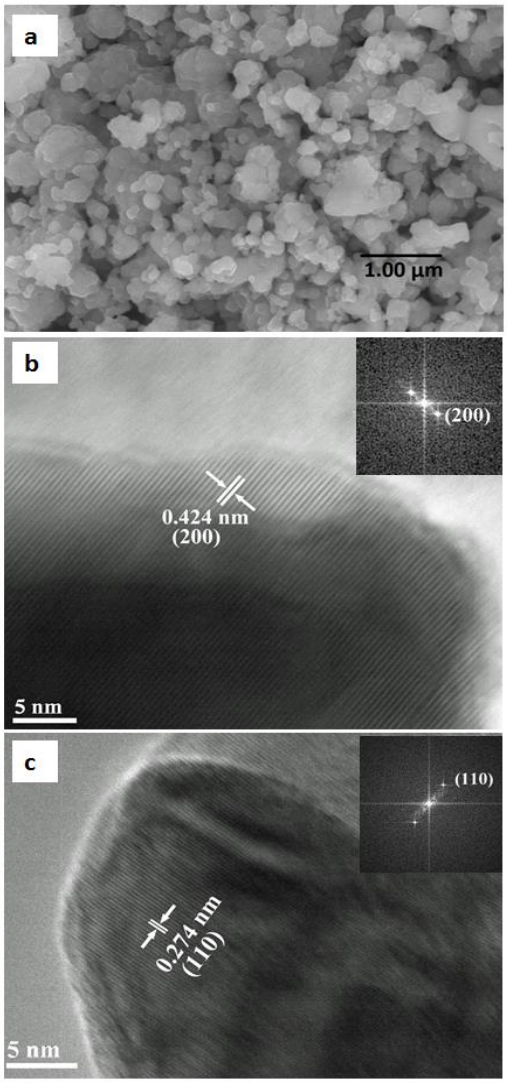

Figure 3-5. Representative microscopy data on $CuO/CuBi_2O_4$ nanocomposite (Cu:Bi = 15:1): (a) SEM image (b and c) HRTEM images showing lattice spacings in the CuO and $CuBi_2O_4$ phases respectively. The insets in frames b and c contain the corresponding numerical FFT patterns.

A similar approach was used to synthesize $CuBi_2O_4/\alpha\text{-}Bi_2O_3$ nanocomposites where an excess of Bi in comparison with Cu precursor was employed for the SCS. XRD patterns for the samples prepared from nonstoichiometric Cu:Bi mixtures with excess of Bi precursor are shown in Figure 3-6. The $\alpha\text{-}Bi_2O_3$ phase (PDF# 01-076-1730) was formed along with the kusachiite phase (PDF# 01-071-5101). A pure form of $\alpha\text{-}Bi_2O_3$ was formed when no Cu-precursor was used.

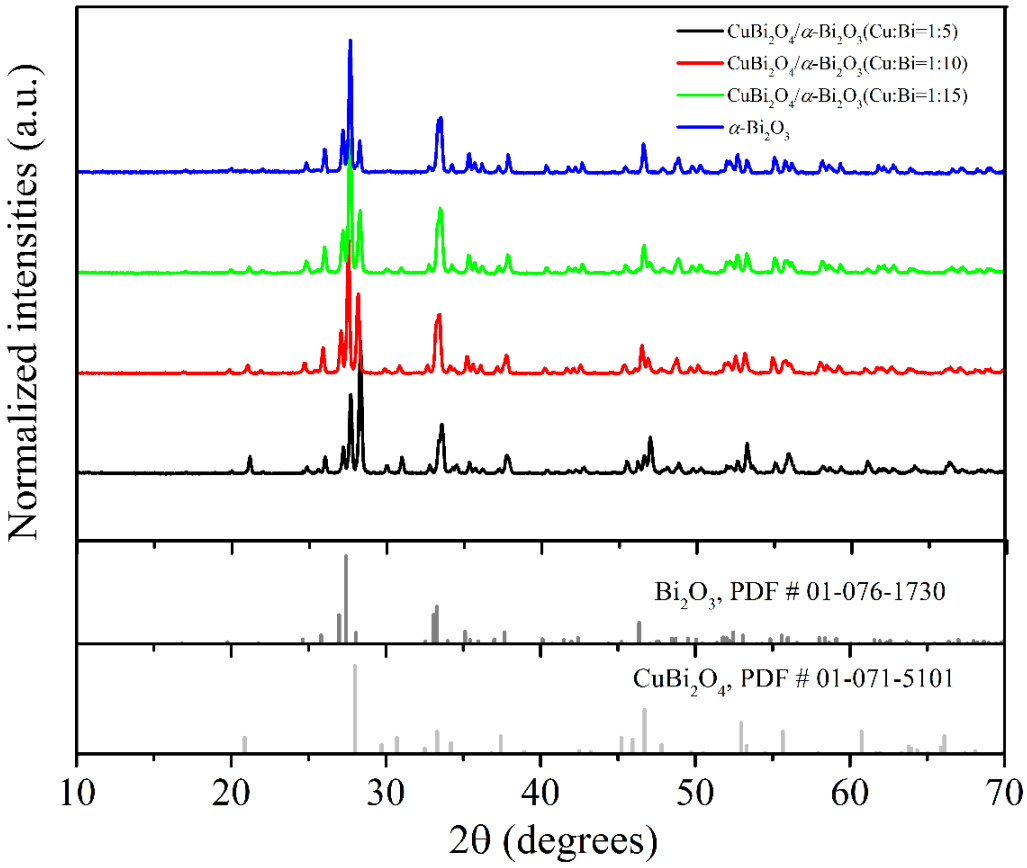

Figure 3-6. XRD pattern of $\alpha\text{-}Bi_2O_3/CuBi_2O_4$ nanocomposites with various Cu:Bi mole ratios in the precursor mixtures. Standard XRD profiles for tetragonal $CuBi_2O_4$ (PDF# 01-071-5101) and $\alpha\text{-}Bi_2O_3$ (PDF# 01-076-1730) are also displayed for comparison.

Rietveld analyses were again performed on the XRD data to estimate amounts of the two phases present in the nanocomposites (Figure A-S5). The results are presented in Figure A-S7, and additional details are contained Table A-S1 (Supporting Information). Interestingly, the agreement between what is expected and what was actually found (from Rietveld analyses), was not quite as satisfactory as in the $CuO/CuBi_2O_4$ cases discussed earlier. The discrepancy is particularly severe in the $CuBi_2O_4$ phase assay (see Figure A-S7 and Table A-S1). This variant behavior in the two nanocomposite cases could be accommodated by contamination with other (as yet unidentified) minority phases beyond just the two phases assumed for these analyses in the α-$Bi_2O_3/CuBi_2O_4$ cases. An SEM image (Figure 3-7a) of the nanocomposite, α-$Bi_2O_3/CuBi_2O_4$ (Cu/Bi = 1:10), showed irregular lumps of particles; this is believed to be due to the high temperature annealing. As the particles were large, it was difficult to see the size distribution in the TEM images. However, the HR-TEM data showed lattice fringes with *d*-spacings of 0.300 nm and 0.324 nm corresponding to the $CuBi_2O_4$ (220) and α-Bi_2O_3 (120) planes, respectively (Figures 3-7b and c).

The average crystallite sizes and BET surface areas of composites are presented in Table 3-5. The $CuO/CuBi_2O_4$ composites had two distinct crystallite sizes, one stemming from the $CuBi_2O_4$ phase and another from CuO. The CuO crystallites were lower in size (~ 25 nm) than $CuBi_2O_4$ (~ 40 nm). On the other hand, Bi_2O_3 (40 nm) formed as larger crystallites than $CuBi_2O_4$ (~30 nm) in the $Bi_2O_3/CuBi_2O_4$ nanocomposites.

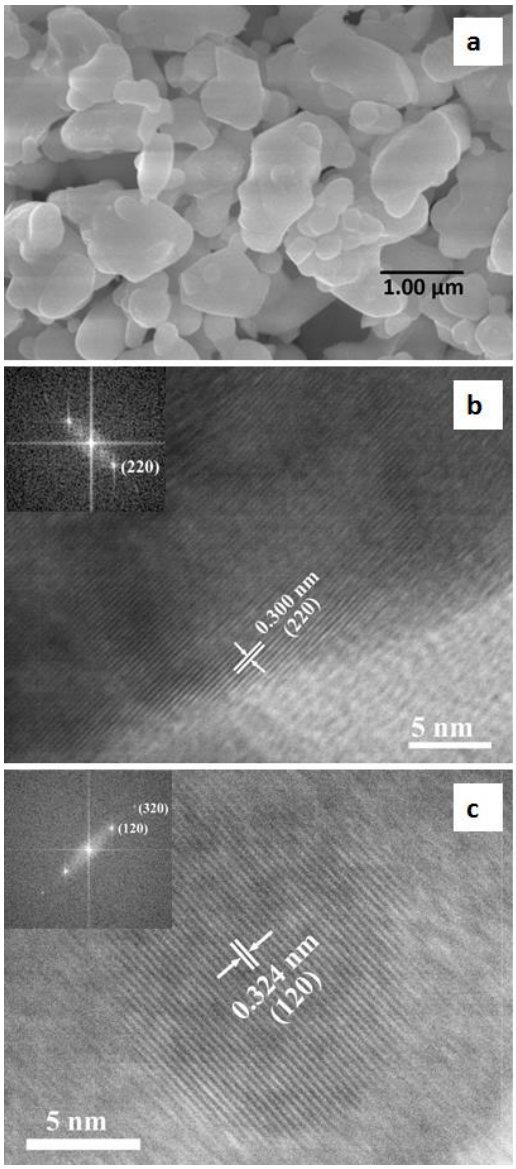

Figure 3-7. Representative microscopy data on α-Bi_2O_3/$CuBi_2O_4$ nanocomposite (Cu:Bi = 1:10): (a) SEM image (b and c) HR-TEM image showing lattice spacings in the α-Bi_2O_3 and $CuBi_2O_4$ phases respectively. The insets in frames b and c show the corresponding numerical FFT patterns.

Table 3-5. Average Crystallite Size of $CuO/CuBi_2O_4$ and α-$Bi_2O_3/CuBi_2O_4$ Composites Annealed at 600 °C

sample identification	BET Surface area (m^2g^{-1})	average crystallite size from $CuBi_2O_4$ peaks (nm)	average crystallite size from CuO or Bi_2O_3 peaks (nm)
$CuO/ CuBi_2O_4$ (5:1)	3.2	36 ± 2	23 ± 2
$CuO/ CuBi_2O_4$ (10:1)	2.5	38 ± 3	24 ± 1
$CuO/ CuBi_2O_4$ (10:1)	2.4	38 ± 4	23 ± 1
α-$Bi_2O_3/CuBi_2O_4$ (1:5)	0.7	28 ± 3	41 ± 2
α-$Bi_2O_3/CuBi_2O_4$ (1:10)	0.8	26 ± 2	38 ± 2
α-$Bi_2O_3/CuBi_2O_4$ (1:15)	0.6	31 ± 2	39±2

a. These values are only approximate since N_2-based BET model analyses are not reliable below 5 m^2g^{-1}, c.f., Ref. 41.

3.3.3 Optical Properties

Optical properties of the various powder samples were measured using UV-visible diffuse reflectance spectroscopy. Figure 3-8a,b shows Tauc plots for $CuBi_2O_4$; both direct and indirect optical transitions could be discerned. The direct bandgap was estimated as 1.84 ± 0.01 eV while the indirect bandgap was located at 1.42 ± 0.02 eV. Figure 3-10c,d shows the variation of bandgap and absorbance with the addition of CuO and α-Bi_2O_3 respectively to the parent ternary compound. As the CuO percentage increased, the bandgap shifted towards the bandgap of CuO (1.46 eV) while α-Bi_2O_3 addition increased the bandgap of composites toward the higher value (2.65 eV) characteristic of α-Bi_2O_3. Table 3-6 compares the present sets of values with those reported in the literature.

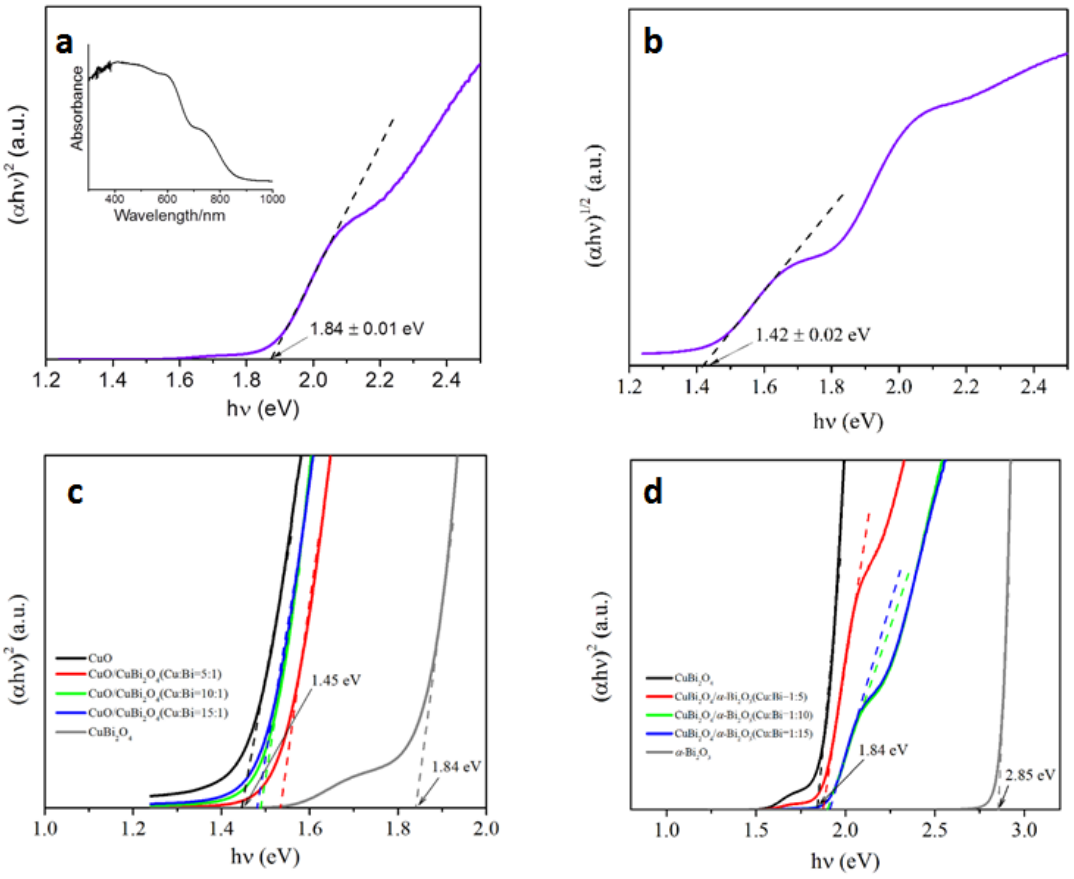

Figure 3-8. Tauc plots showing (a) direct band gap (b) indirect bandgap of $CuBi_2O_4$ (c) direct bandgap changes for $CuO/CuBi_2O_4$ nanocomposites (d) direct bandgap changes for α-$Bi_2O_3/CuBi_2O_4$ nanocomposites. Tauc plots for pure CuO and α-Bi_2O_3 are also included for comparison in frames c and d respectively. See also Table 6. The inset in frame 'a' contains a representative spectrum.

Table 3-6. Bandgaps of Solution Combustion-Synthesized $CuBi_2O_4$ and Its Nanocomposites with CuO and α-Bi_2O_3 along with Literature-Reported Values

method of preparation	sample	bandgap (eV)	mode of transition	method of determination	ref
solution combustion synthesis	$CuBi_2O_4$	1.85	direct	Tauc plot from DRS	this study
		1.42	indirect		
	CuO	1.45	direct		
	$CuO/CuBi_2O_4$	1.54 (Cu:Bi = 5:1)	direct		
		1.50 (Cu:Bi = 10:1)			
		1.48 (Cu:Bi = 15:1)			
	α-Bi_2O_3	2.85	direct		
	α-$Bi_2O_3/CuBi_2O_4$	1.88 (Cu:Bi = 1:5)	direct		
		1.92 (Cu:Bi = 1:10)			
		1.93 (Cu:Bi = 1:15)			
electrodeposition	$CuBi_2O_4$	1.8	-	absorption edge	16
solid-state reaction		1.30	indirect	Tauc plot from DRS	17
hydrothermal		1.75	-	absorption edge	22
electrodeposition		1.80	direct	Tauc plot from DRS	24
solution precipitation		1.74	direct	Tauc plot from DRS	25
electrodeposition		1.60	indirect	Tauc plot from DRS	31
drop-casting		1.8	-	absorption edge	34
electrochemical	CuO	1.38 – 1.56	direct	Tauc plot from DRS	43
solution precipitation	α-Bi_2O_3	2.68	indirect	Tauc plot from DRS	44

3.3.4 Photoelectrochemical Properties

Figure 3-9a shows chopped (light/dark) linear sweep voltammetry (LSV) scans for $CuBi_2O_4$, CuO, and $CuO/CuBi_2O_4$ (Cu/Bi = 15 : 1) with N_2 bubbling. The photocurrent polarity was cathodic consistent with the fact that all the compounds as synthesized behaved as *p*-type semiconductors. Disappointingly, the photocurrent density for pure $CuBi_2O_4$ was low compared to pure CuO. However, one of the nanocomposites ($CuO/CuBi_2O_4$, Cu/Bi = 15:1) showed improved photocurrent response than the parent oxides. Data on the other two nanocomposite $CuO/CuBi_2O_4$ samples are included for comparison in Figure A-S8. The shapes of the photovoltammograms are more complex than those typically observed for single crystal samples and can be attributed to the many more carrier recombination pathways available for nanocrystalline samples such as those considered in Figure 3-9. Also worthy of note is the peaked (rather than plateau) photoresponse for some of the nanocomposite samples (e.g., the "15:1" $CuO/CuBi_2O_4$ sample in Figures 3-9a and A-S8). The improved photoactivity of the $CuO/CuBi_2O_4$ samples (relative to $CuBi_2O_4$) is in line with the trends observed for corresponding nanocomposite samples prepared by other methods in two recent studies.[25,26]

On the other hand, the $Bi_2O_3/CuBi_2O_4$ nanocomposite sample only marginally outperformed both the α-Bi_2O_3 and $CuBi_2O_4$ samples (Figure 3-9b). However, in this case, it was the 1:10 composition that was optimal. The photocurrents were also markedly more spiked than in the cases shown in Figure 3-9a. Figure A-S9 contains the data counterparts of Figure A-S8 for the three α-$Bi_2O_3/CuBi_2O_4$ samples. The photocurrent onset potentials were also more positive than in the samples in Figure 3-9a.

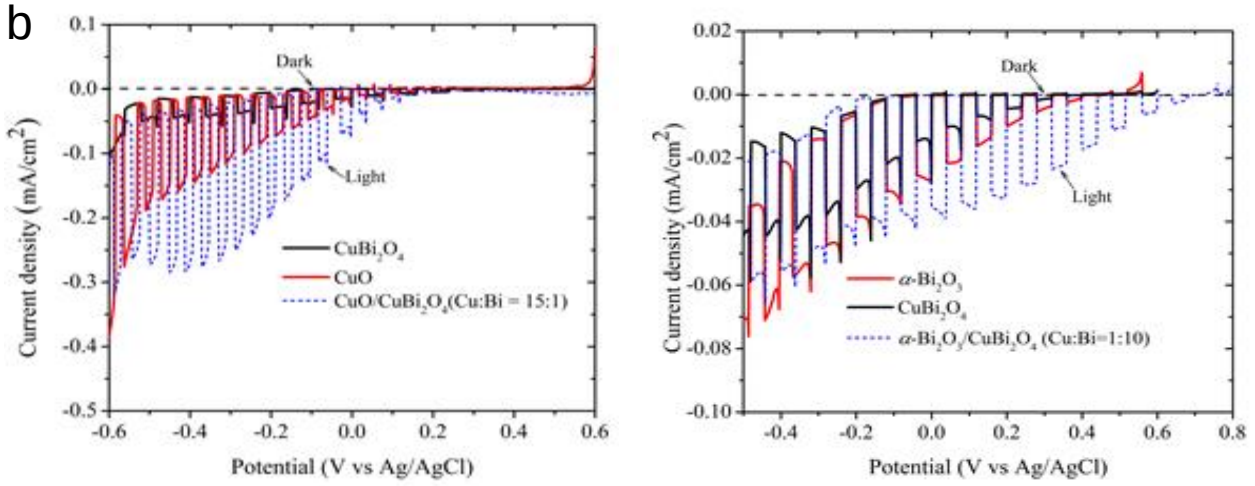

Figure 3-9. Chopped (light/dark) linear sweep voltammetry scans for (a) $CuBi_2O_4$ along with CuO and optimized CuO/$CuBi_2O_4$ nanocomposite (b) $CuBi_2O_4$ along with α-Bi_2O_3 and optimized α-Bi_2O_3/$CuBi_2O_4$. The photovoltammograms were run in 0.1 M Na_2SO_4 electrolyte with a potential scan rate of 1 mVs^{-1} with N_2 bubbling.

These trends are rationalizable in terms of energy band diagrams. An energy band diagram for CuO/$CuBi_2O_4$ (Figure 3-10a) supports the transfer of electrons from the $CuBi_2O_4$ conduction band to the CuO conduction band due to the difference of band energy positions. Similarly, the photogenerated holes can transfer to the valence band of CuO from the valence band of $CuBi_2O_4$. The net result is amelioration of carrier accumulation in the $CuBi_2O_4$ phase, lowered carrier recombination, and a higher photocurrent. On the other hand, the band alignments are such that in the α-Bi_2O_3/$CuBi_2O_4$ nanocomposite case (Figure 3-10b), there should be facile carrier recombination. This is indeed what is observed (compare Figures 3-9a and b). In general, the presented band edge alignments in Figure 3-10 are in good agreement with data on CuO/$CuBi_2O_4$ heterojunctions derived from other synthesis methodologies.[25,26]

We presume in all the cases that the cathodic photocurrent results in the reduction of protons at the interface although no attempt was made to identify the product (H_2). Note also that the nitrogen purge ensured that dioxygen reduction was not a factor in these experiments.

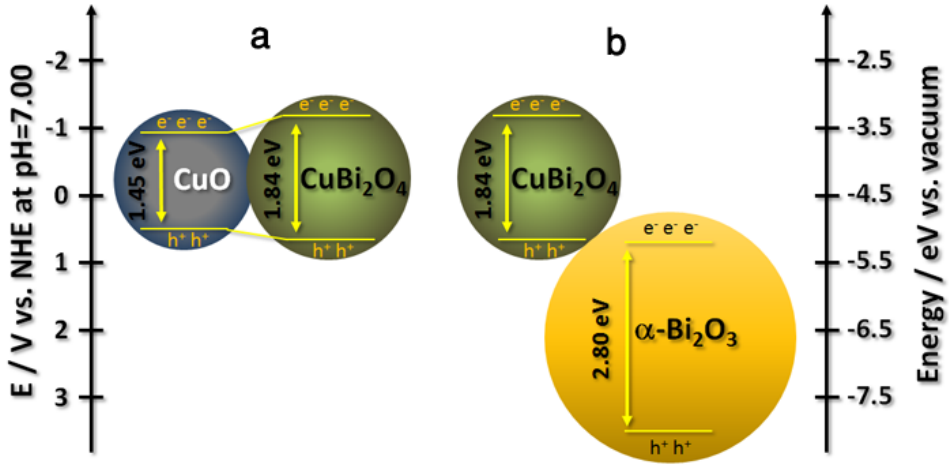

Figure 3-10. Energy band diagrams and vectorial charge transfer for (a) $CuO/CuBi_2O_4$ (b) α-$Bi_2O_3/CuBi_2O_4$.

Figure 3-11 shows the photoaction spectra, for the various metal-oxide coated electrodes in this study, in CO_2 saturated $NaHCO_3$. In all cases, the bandgap of the materials was estimated by fitting the cut-off region with a straight-line segment and extrapolating it to the wavelength axis. The photoactivity of pristine $CuBi_2O_4$ stretched into the visible region of the spectrum. A bandgap value of 2.08 eV was determined for $CuBi_2O_4$, in reasonable agreement with the 1.84 eV value obtained from DRS measurements (see above and Table 3-6) especially considering the rather severe kinetics barriers associated with the CO_2 reduction reaction.[5] By altering the SCS condition to form excess CuO, the overall light harvesting performance of the nanocomposite sample clearly increases to a broader spectral range. The enhanced visible light absorbance results in a bandgap

value of 1.41 eV, in excellent agreement with both the 1.45 eV value determined from optical measurements and values reported in the literature (Table 3-6).

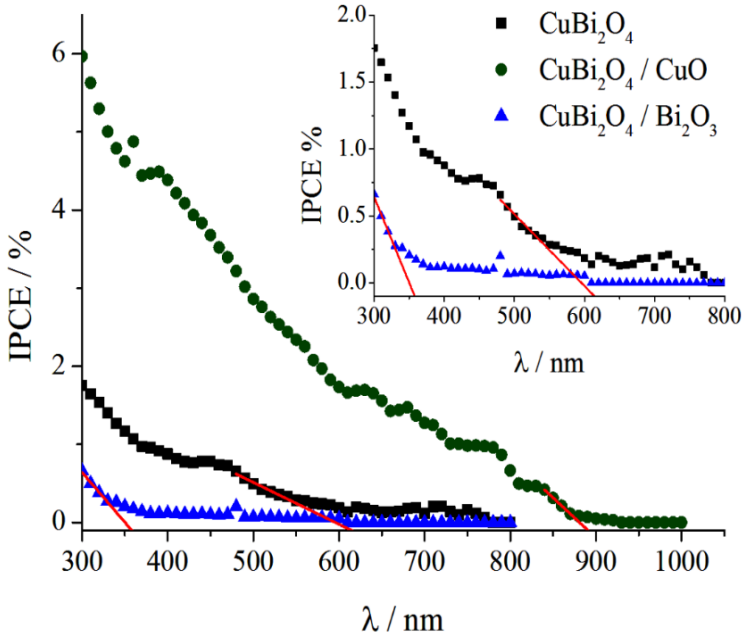

Figure 3-11. Photoaction spectra for $CuBi_2O_4$, $CuBi_2O_4$/CuO (Cu:Bi = 15:1) and $CuBi_2O_4/Bi_2O_3$ (Cu:Bi = 1:10) samples in 0.5 M $NaHCO_3$ saturated with CO_2 at E = -0.3 V, $\Delta\lambda$ = 10 nm. For better visualization, the inset shows a magnified portion of the original curve for two of the samples.

Interestingly, with the SCS conditions favoring the formation of Bi_2O_3-rich material, the behavior attributable only to the α-Bi_2O_3 portion of the sample can be clearly distinguished by breaks (discontinuities) in the spectra in Figure 3-11. Thus, the fitting in the low-wavelength region, resulted in a bandgap of 3.54 eV which is higher than the 2.85 eV value for Bi_2O_3 (Table 3-6). It is tempting to attribute this discrepancy to the same factor seen earlier; namely, sample contamination with other minority phases.

Finally, the photoaction spectral data in Figure 3-11 demonstrate that these samples have activity attributable not only to the hydrogen evolution reaction (HER) but also toward CO_2

reduction, although the reaction products have not been explicitly identified in the two cases yet. Note also that the trend between the relative photoactivity of the $CuBi_2O_4$ and $CuBi_2O_4/Bi_2O_3$ samples is reversed in Figures 3-9b and 3-11. However, this can be rationalized by the fact that the electrolytic media (and thus the photoreactions) are different in the two sets of PEC experiments related to Figures 3-9b and 3-11.

3.4 CONCLUDING REMARKS

This study demonstrates that solution combustion synthesis (SCS) can be added to the library of methods for preparing *p*-$CuBi_2O_4$. Importantly, however, simple tuning of the SCS precursor mixture composition enables ready synthesis of a range of nanocomposites from CuO at one end to α-Bi_2O_3 at the other. We have shown in this study that the nanocomposite electrode outperformed the pure $CuBi_2O_4$ albeit to varying degrees for Bi_2O_3 and CuO. More importantly, the enhancement in the PEC behavior is not a simple sum of the activity of the individual components. The enhanced charge carrier separation seen here was a synergetic effect, facilitated by proper alignment of the band edge positions. Further efforts aimed at improving the electronic and morphological characteristics of the samples for applications related to solar water splitting or CO_2 photoreduction are in progress.

3.5 REFERENCES

1. Rajeshwar, K.; McConnell, R.; Licht, S. *Solar Hydrogen Generation*; Springer: New York, 2008.
2. Rajeshwar, K. Solar Energy Conversion and Environmental Remediation Using Inorganic Semiconductor–Liquid Interfaces: The Road Traveled and the Way Forward. *J. Phys. Chem. Lett.* 2011, *2*, 1301-1309.
3. Rajeshwar, K.; Thomas, A.; Janáky, C. Photocatalytic Activity of Inorganic Semiconductor Surfaces: Myths, Hype, and Reality. *J. Phys. Chem. Lett.* 2015, *6*, 139-147.
4. Paracchino, A.; Laporte, V.; Sivula, K.; Grätzel, M.; Thimsen, E. Highly Active Oxide Photocathode for Photoelectrochemical Water Reduction. *Nat. Mat.* 2011, *10*, 456-461.
5. Janáky, C.; Hursán, D.; Endrődi, B.; Chanmanee, W.; Roy, D.; Liu, D.; de Tacconi, N.; Dennis, B.; Rajeshwar, K. Electro- and Photoreduction of Carbon Dioxide: The Twain Shall Meet at Copper Oxide/Copper Interfaces. *ACS Energy Lett.* 2016, *1*, 332-338.

6. Kang, U.; Choi, S.; Ham, D.; Ji, S.; Choi, W.; Han, D.; Abdel-Wahab, A.; Park, H. Photosynthesis of Formate from CO_2 and Water at 1% Energy Efficiency *via* Copper Iron Oxide Catalysis. *Energy Environ. Sci.* 2015, *8*, 2638-2643.
7. Gu, J.; Wuttig, A.; Krizan, J.; Hu, Y.; Detweiler, Z.; Cava, R.; Bocarsly, A. Mg-Doped $CuFeO_2$ Photocathodes for Photoelectrochemical Reduction of Carbon Dioxide. *J. Phys. Chem. C* 2013, *117*, 12415–12422.
8. Prévot, M.; Guijarro, N.; Sivula, K. Enhancing the Performance of a Robust Sol-Gel-Processed p-Type Delafossite $CuFeO_2$ Photocathode for Solar Water Reduction. *ChemSusChem* 2015, *8*, 1359-1367.
9. Gu, J.; Yan, Y.; Krizan, J.; Gibson, Q.; Detweiler, Z.; Cava, R.; Bocarsly, A. p-Type $CuRhO_2$ as a Self-Healing Photoelectrode for Water Reduction Under Visible Light. *J. Am. Chem. Soc.* 2014, *136*, 830–833.
10. Thomas, A.; Janáky, C.; Samu, G.; Huda, M.; Sarker, P.; Liu, J.; van Nguyen, V.; Wang, E.; Schug, K.; Rajeshwar, K. Time- and Energy-Efficient Solution Combustion Synthesis of Binary Metal Tungstate Nanoparticles with Enhanced Photocatalytic Activity. *ChemSusChem* 2015, *8*, 1652-1663.
11. Köferstein, R.; Walther, T.; Hesse, D.; Ebbinghaus, S. Crystallite-Growth, Phase Transition, Magnetic Properties, and Sintering Behaviour of Nano-$CuFe_2O_4$ Powders Prepared by a Combustion-Like Process. *J. Solid State Chem*. 2014, *213*, 57-64.
12. Kormányos, A.; Thomas, A.; Huda, M.; Sarker, P.; Liu, J.; Poudyal, N.; Janáky, C.; Rajeshwar, K. Solution Combustion Synthesis, Characterization, and Photoelectrochemistry of $CuNb_2O_6$ and $ZnNb_2O_6$ Nanoparticles. *J. Phys. Chem. C* 2016, *120*, 16024-16034.
13. Kamimura, S.; Murakami, N.; Tsubota, T.; Ohno, T. Fabrication and Characterization of a p-Type $Cu_3Nb_2O_8$ Photocathode toward Photoelectrochemical Reduction of Carbon Dioxide. *Appl. Catal. B Environ.* 2015, *174-175*, 471-476.
14. Arai, T.; Yanagida, M.; Konishi, Y.; Iwasaki, Y.; Sugihara, H.; Sayama, K. Efficient Complete Oxidation of Acetaldehyde into CO_2 Over $CuBi_2O_4$ /WO_3 Composite Photocatalyst Under Visible and UV Light Irradiation. *J. Phys. Chem. C* 2007, *111*, 7574-7577.
15. Wei, L.; Shifu, C.; Sujuan, Z.; Wei, Z.; Huaye, Z.; Xiaoling, Y. Preparation And Characterization of p–n Heterojunction Photocatalyst p-$CuBi_2O_4$/n-TiO_2 with High Photocatalytic Activity Under Visible and UV Light Irradiation. *J. Nanopart. Res.* 2009, *12*, 1355-1366.
16. Hahn, N.; Holmberg, V.; Korgel, B.; Mullins, C. Electrochemical Synthesis and Characterization of p-$CuBi_2O_4$ Thin Film Photocathodes. *J. Phys. Chem. C* 2012, *116*, 6459-6466.
17. Elaziouti, A.; Laouedj, N.; Bekka, A. Synergetic Effects of Sr-Doped $CuBi_2O_4$ Catalyst with Enhanced Photoactivity under UVA– Light Irradiation. *Environ. Sci. Pollut. Res.* 2015, *23*, 15862-15876.
18. Xie, Y.; Zhang, Y.; Yang, G.; Liu, C.; Wang, J. Hydrothermal Synthesis of $CuBi_2O_4$ Nanosheets and Their Photocatalytic Behavior under Visible Light Irradiation. *Mater. Lett.* 2013, *107*, 291-294.
19. Nishikawa, M.; Hiura, S.; Mitani, Y.; Nosaka, Y. Enhanced Photocatalytic Activity of $BiVO_4$ by Co-Grafting of Metal Ions and Combining with $CuBi_2O_4$. *J. Photochem. Photobiol. A* 2013, *262*, 52-56.

20. Zhang, Y.; Xie, Y.; Li, J.; Yang, G.; Bai, T.; Wang, J. Effects of Synthetic Conditions on the Morphology and Catalytic Properties of Hierarchical $CuBi_2O_4$ Nanoflowers Grown by Low-Temperature Solution Process. *J. Alloys Compd.* 2013, *580*, 172-175.
21. Berglund, S.; Lee, H.; Núñez, P.; Bard, A.; Mullins, C. Screening of Transition and Post-Transition Metals to Incorporate into Copper Oxide and Copper Bismuth Oxide for Photoelectrochemical Hydrogen Evolution. Phys. Chem. Chem. Phys. 2013, *15*, 4554.
22. Sharma, G.; Zhao, Z.; Sarker, P.; Nail, B.; Wang, J.; Huda, M.; Osterloh, F. Electronic Structure, Photovoltage, and Photocatalytic Hydrogen Evolution with p-$CuBi_2O_4$ Nanocrystals. *J. Mater. Chem. A* 2016, *4*, 2936-2942.
23. Oh, W.; Lua, S.; Dong, Z.; Lim, T. Rational Design of Hierarchically-Structured $CuBi_2O_4$ Composites by Deliberate Manipulation of the Nucleation and Growth Kinetics of $CuBi_2O_4$ for Environmental Applications. *Nanoscale* 2016, *8*, 2046-2054.
24. Nakabayashi, Y.; Nishikawa, M.; Nosaka, Y. Fabrication of $CuBi_2O_4$ Photocathode through Novel Anodic Electrodeposition for Solar Hydrogen Production. *Electrochim. Acta* 2014, *125*, 191-198.
25. Patil, R.; Kelkar, S.; Naphade, R.; Ogale, S. Low Temperature Grown $CuBi_2O_4$ with Flower Morphology and its Composite with CuO Nanosheets for Photoelectrochemical Water Splitting. *J. Mater. Chem. A* 2014, *2*, 3661-3668.
26. Park, H.; Lee, C.; Reisner, E. Photoelectrochemical Reduction of Aqueous Protons with a CuO|$CuBi_2O_4$ Heterojunction under Visible Light Irradiation. *Phys. Chem. Chem. Phys.* 2014, *16*, 22462-22465.
27. Muthukrishnaraj, A.; Vadivel, S.; Joni, I.; Balasubramanian, N. Development of Reduced Graphene Oxide/$CuBi_2O_4$ Hybrid for Enhanced Photocatalytic Behavior under Visible Light Irradiation. *Ceram. Int*.2015, *41*, 6164-6168.
28. Oh, W.; Lua, S.; Dong, Z.; Lim, T. A Novel Three-Dimensional Spherical $CuBi_2O_4$ Consisting of Nanocolumn Arrays with Persulfate and Peroxymonosulfate Activation Functionalities for 1H-Benzotriazole Removal. *Nanoscale* 2015, *7*, 8149-8158.
29. Chen, M.; Yang, Q.; Li, L.; Liu, M.; Xiao, P.; Zhang, M. Solid-State Synthesis of $CuBi_2O_4$/MWCNT Composites with Enhanced Photocatalytic Activity under Visible Light Irradiation. *Mater. Lett.* 2016, *171*, 255-258.
30. Deng, Y.; Chen, Y.; Chen, B.; Ma, J. Preparation, Characterization and Photocatalytic Activity of $CuBi_2O_4$/$NaTaO_3$ Coupled Photocatalysts. *J. Alloys Compd*. 2013, *559*, 116-122.
31. Cao, D.; Nasori, N.; Wang, Z.; Mi, Y.; Wen, L.; Yang, Y.; Qu, S.; Wang, Z.; Lei, Y. p-Type $CuBi_2O_4$: an Easily Accessible Photocathodic Material for High-Efficiency Water Splitting. *J. Mater. Chem. A* 2016, *4*, 8995-9001.
32. Kang, D.; Hill, J.; Park, Y.; Choi, K. Photoelectrochemical Properties and Photostabilities of High Surface Area $CuBi_2O_4$ and Ag-Doped $CuBi_2O_4$ Photocathodes. *Chem. Mater.* 2016, *28*, 4331-4340.
33. Oh, W.; Dong, Z.; Lim, T. Hierarchically-Structured Co-$CuBi_2O_4$ and Cu-$CuBi_2O_4$ for Sulfanilamide Removal via Peroxymonosulfate Activation. *Catal. Today* 2016, *280*, 2-7.
34. Berglund, S.; Abdi, F.; Bogdanoff, P.; Chemseddine, A.; Friedrich, D.; van de Krol, R. Comprehensive Evaluation of $CuBi_2O_4$ as a Photocathode Material for Photoelectrochemical Water Splitting. *Chem. Mater.* 2016, *28*, 4231-4242.

35. Tsang, C.; Meen, J.; Elthon, D. Phase Equilibria of the Bismuth Oxide-Copper Oxide System in Oxygen at 1 atm. *J. Am. Ceram. Soc.* 1994, *77*, 3119-3124.
36. Rajeshwar, K.de Tacconi, N. Solution Combustion Synthesis of Oxide Semiconductors for Solar Energy Conversion and Environmental Remediation. *Chem. Soc. Rev.* 2009, *38*, 1984-1998.
37. Li, F.; Ran, J.; Jaroniec, M.; Qiao, S. Solution Combustion Synthesis of Metal Oxide Nanomaterials for Energy Storage and Conversion. *Nanoscale* 2015, *7*, 17590-17610.
38. Patil, K. C.; Hegde, M. S.; Rattan, T.; Aruna, S. T. *Chemistry of Nanocrystalline Oxide Materials - Combustion Synthesis, Properties and Applications*; World Scientific Publishing Co.: NJ, 2008.
39. Kumar, A.; Wolf, E.; Mukasyan, A. Solution Combustion Synthesis of Metal Nanopowders: Copper and Copper/Nickel Alloys. *AIChE J.* 2011, *57*, 3473-3479.
40. Mukhopadhyay, C.; Datta, A. Bismuth (III) Nitrate Pentahydrate: a Stoichiometric Reagent for Microwave Induced Mild and Highly Efficient Aerial Oxidation of Aromatic Aldehydes Under Solvent-Free Conditions. *Cat. Comm.* 2008, *9*, 2588-2592.
41. For example, Jillavenkatesa, A.; Onoda, G. *Advances in Process Measurements for the Ceramic Industry*; 1st ed.; American Ceramic Society: Westerville, Ohio, 1999. 69-86.
42. de Tacconi, N.; Timmaji, H.; Chanmanee, W.; Huda, M.; Sarker, P.; Janáky, C.; Rajeshwar, K. Photocatalytic Generation of Syngas Using Combustion-Synthesized Silver Bismuth Tungstate. *ChemPhysChem* 2012, *13*, 2945-2955.
43. Nakaoka, K.; Ueyama, J.; Ogura, K. Photoelectrochemical Behavior of Electrodeposited CuO and Cu_2O Thin Films on Conducting Substrates. *J. Electrochem. Soc.* 2004, *151*, C661-C665.
44. Jiang, H.; Liu, J.; Cheng, K.; Sun, W.; Lin, J. Enhanced Visible Light Photocatalysis of Bi_2O_3 upon Fluorination. *J. Phys. Chem. C* 2013, *117*, 20029-20036.

CHAPTER 4

RAPID ONE-POT SYNTHESIS AND PHOTOELECTROCHEMICAL PROPERTIES OF COPPER VANADATES

https://doi.org/10.1021/acsaem.9b00179

ABSTRACT

Solution combustion synthesis (SCS) is shown to be versatile for the rapid one-pot synthesis of three compounds and four polymorphs in the Cu-V-O ternary family: α-CuV_2O_6, α- and β-$Cu_2V_2O_7$, and γ-$Cu_3V_2O_8$. These compounds feature copper: vanadium stoichiometric ratios ranging from 1:1 to 3:1; their structural, electronic, optoelectronic, and photoelectrochemical attributes were comprehensively characterized by a combination of theoretical and experimental techniques. The main contribution of the present study is the demonstration that a range of stoichiometries in this compound family can be derived simply by tuning the precursor mole ratio in the SCS procedure. The Cu-V-O family of samples, derived by SCS, is shown to exemplify the strong effect of compound stoichiometry on the optoelectronic and photoelectrochemical properties. Overall, α-CuV_2O_6 showed the best performance, rooted in the direct nature of the optical transition in this material. Finally, SCS is very time-efficient and the various compositions can be obtained in a matter of minutes, as opposed to hours or even days in classical solution-based or ceramic synthesis routes.

4.1 INTRODUCTION

We show in this paper that solution combustion synthesis (SCS)[1-5] is versatile for preparing various compound stoichiometries within the Cu-V-O ternary family simply by varying the copper/vanadium mole ratio in a "one-pot" precursor mixture. Trends in the materials chemistry properties and photoelectrochemical (PEC) activity[6,7] are presented as are corresponding trends in polymorphic modifications and electronic band structures. The stoichiometries of the various compounds in this family may be visualized[8] in terms of the CuO/V_2O_5 combining ratio in the ultimate ternary composition, as shown in the second column in Table 4-1.

Table 4-1. Synthetic Methods for Copper Vanadates

oxide composition	CuO: V_2O_5	polymorph	mineral name (crystal structure)	synthesis method	ref
CuV_2O_6	1:1	α-CuV_2O_6	- (triclinic)	ceramic method	9
				drop-casting	10
				ink-jet printing	11
				sol-gel	12,13
				electrospray	14
				hydrothermal	15
$Cu_2V_2O_7$	2:1	α- $Cu_2V_2O_7$	blossite (orthorhombic)	ceramic method	9
				magnetron co-sputtering	16
				inkjet-printing	11
		β- $Cu_2V_2O_7$	ziesite (monoclinic)	ceramic method	9
				flux growth method	17
				drop-casting	10
				magnetron co-sputtering	16
				ink-jet printing	11
				electrospray	14
		γ- $Cu_2V_2O_7$	- (triclinic)	ceramic method	18,19

		β- $Cu_3V_2O_8$	pseudolynsite (monoclinic)	ceramic method	20
				solution precipitation	21-24
$Cu_3V_2O_8$	3:1				
		γ- $Cu_3V_2O_8$	mcbirneyite (triclinic)	ceramic method	20
				magnetron co-sputtering	16,25
$Cu_{11}V_6O_{26}$	11:3	$Cu_{11}V_6O_{26}$	fingerite (triclinic)	electrochemical approach	26
				magnetron co-sputtering	16
$Cu_5V_2O_{10}$	5:1	$Cu_5V_2O_{10}$	stoiberite (monoclinic)	ceramic method	9
				inkjet-printing	11
	CuV_2O_6, $Cu_2V_2O_7$, $Cu_3V_2O_8$			solution combustion synthesis	this study

The combination of a narrow energy bandgap (in the ~2 eV range) and excellent stability against photocorrosion has thrust copper vanadates into the forefront of emerging photoanode materials for solar fuels generation.[10-12,14,16,25-29] In the continuing search for a magic bullet semiconductor material, it is imperative that the synthesis technique is time-efficient. Otherwise, materials screening is bound to be inefficient and cost-ineffective from a practical standpoint. In this vein, this study seeks to demonstrate the virtues of SCS as a screening tool to generate a series of compounds with progressively-tuned stoichiometries from a single "pot". Interest in the structural aspects of Cu-V-O materials appears to have begun in 1958;[30] this early study identified stoichiometries ranging from 1:1 to 5:1 within the system. Notably, the 4:1 stoichiometry was missing from a subsequently reported phase diagram,[31] and, accordingly, previous authors were unable to prepare $Cu_4V_2O_9$ (see ref 32 and references therein). Other than the PEC applications of immediate interest within the present study context, copper vanadates are also of technological interest as lithium-intercalating battery cathodes[9,13,15,23,33,34] (or even anodes[35]), thermal

batteries,[9,36] unique magnetic materials,[16,17,20,37-39] flame retardants,[40] photocatalysts for environmental remediation,[21,23] or as catalysts in solar thermochemical water splitting cycles.[41-43]

Polymorphic transformations have been of interest right from the early history of study of the Cu-V-O family to the present.[18,19,32,44-48] Thus, $Cu_2V_2O_7$ features three polymorphs, α-, β-, and γ- whose thermal interconversions have been studied[18] by the combined use of X-ray diffraction (XRD) and thermal analysis (specifically, differential thermal analysis or DTA). Similar studies have been performed on phase transitions in $Cu_3V_2O_8$, where again three modifications were reported.[44] Single crystals of α-CuV_2O_6 and the β- and γ-$Cu_2V_2O_7$ phases have been grown by the flux growth method or in melts.[17,38] A variety of polymorphs was also seen in studies employing high throughput combinatorial methodology[11,16] on CuV_2O_6 (α-), $Cu_2V_2O_7$ (α- and β), and $Cu_3V_2O_8$ (γ-). We were able to delineate the various polymorphs in our SCS samples using XRD (with Rietveld refinement) as a function of their thermal anneal history. The photoactivity of these polymorphs will be shown to depend crucially on the stoichiometry of the copper vanadates.

Finally, experimental results on the four SCS-derived copper vanadates in this study (α-CuV_2O_6, α- and β-$Cu_2V_2O_7$, and γ-$Cu_3V_2O_8$) were corroborated by electronic band structure calculations. Precedent theoretical studies, involving density functional theory (DFT) or relativistic and *ab initio* calculations, are noted here for $Cu_2V_2O_7$, $Cu_3V_2O_8$, and $Cu_{11}V_6O_{26}$.[16,27,39,47] In the $Cu_2V_2O_7$ case, the electronic, structural, and magnetic properties of all three phases (α-, β-, and γ-) were mapped in the first-principles study.[16] The electronic structures have been experimentally mapped *via* the use of X-ray absorption spectroscopy.[25] The overlapping aspects of our new results with the corpus of literature information summarized in this introductory section, and also presented in Table 1, will be further elaborated in what follows below.

4.2 EXPERIMENTAL SECTION

4.2.1 Materials. Copper nitrate hemi (pentahydrate) [$Cu(NO_3)_2 \cdot 2.5\ H_2O$ (Alfa Aesar)] and ammonium vanadate [NH_4VO_3 (Alfa Aesar)] were used as Cu and V source respectively. DL-Malic acid [$C_6H_4O_5$ (Alfa Aesar)] was used as fuel as well as complexing agent for vanadate ion in the solutions. Sodium tetraborate decahydrate [($Na_2B_4O_7 \cdot 10\ H_2O$ (Sigma Aldrich)] and boric acid (H_3BO_3) were used to prepare electrolyte solutions for PEC characterizations. Double-distilled water (Corning Megapure) was used to prepare all the solutions. All the chemicals were used as received without further purification.

4.2.2 Solution Combustion Synthesis. Stoichiometric amounts of precursors were calculated and are shown in eqs 1-3.

$$3\ Cu(NO_3)_2 \cdot 2.5\ H_2O + 6\ NH_4VO_3 + C_4H_6O_5 \rightarrow 3\ CuV_2O_6(s) + 6\ N_2\ (g) + 4\ CO_2\ (g) + 22.5\ H_2O\ (g) \quad (1)$$

$$12\ Cu(NO_3)_2 \cdot 2.5\ H_2O + 12\ NH_4VO_3 + 7\ C_4H_6O_5 \rightarrow 6\ Cu_2V_2O_7(s) + 18\ N_2\ (g) + 28\ CO_2\ (g) + 75\ H_2O\ (g) \quad (2)$$

$$3\ Cu(NO_3)_2 \cdot 2.5\ H_2O + 2\ NH_4VO_3 + 2\ C_4H_6O_5 \rightarrow Cu_3V_2O_8(s) + 4\ N_2\ (g) + 8\ CO_2\ (g) + 17.5\ H_2O\ (g) \quad (3)$$

A stoichiometric amount of copper nitrate was dissolved in water while stoichiometric proportions of ammonium vanadate and DL-malic acid (1:1 mole ratio) were dissolved in water. Then, the two solutions were mixed together with continuous stirring leading to the homogeneous precursor solution with a final concentration listed in Table 4-2. The precursor mixtures were then transferred to a preheated muffle furnace set at a temperature of ~ 300 °C (Figure 4-1). The precursor mixture was first dehydrated and brought to ignition; finally sintering of the sample set in. It took 5-10 min to complete the reaction; the product at this stage is termed “as-synthesized” in what follows. The as-synthesized samples were then annealed at different temperatures, both to remove remaining organic traces and to secure improved crystallinity.

Table 4-2. Concentration of Precursor Mixtures for Different Copper Vanadates

targeted ternary oxide composition	concentration in precursor mixtures		
	$[Cu(NO_3)_2 \cdot 2.5\ H_2O]$	$[NH_4VO_3]$	$[C_6H_4O_5]$
CuV_2O_6	0.25 M	0.50 M	0.75 M
$Cu_2V_2O_7$	0.50 M	0.50 M	1.0 M
$Cu_3V_2O_8$	0.75 M	0.50 M	1.25 M

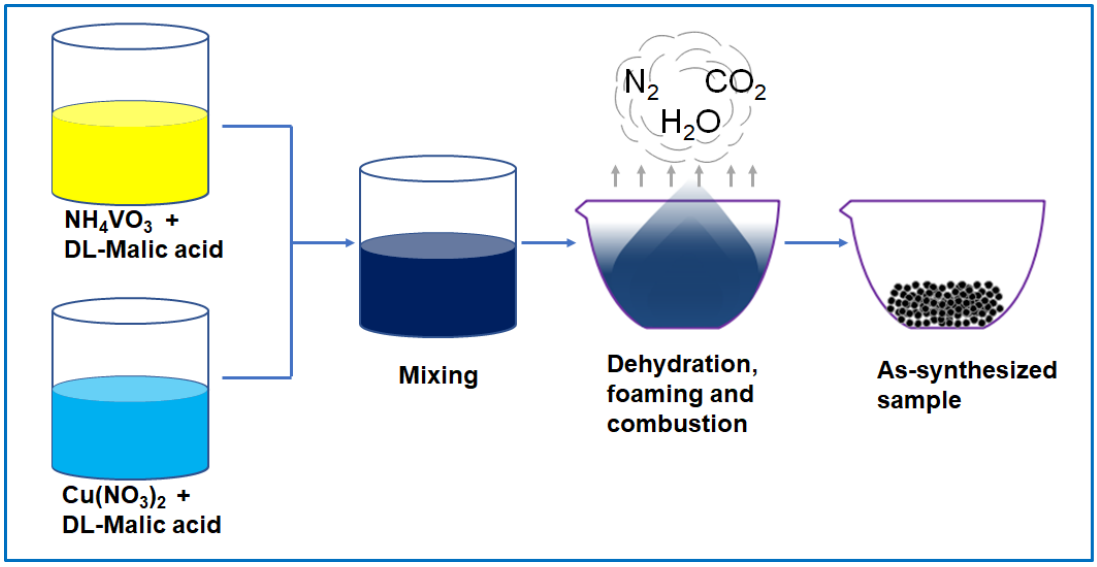

Figure 4-1. Schematic diagram of the solution combustion synthesis process. Refer to refs. 1-4 for further details.

4.2.3 Physical Characterizations. To study the combustion pattern of the precursor mixture, a simulation of combustion reactions was performed using thermogravimetric analysis (TGA) and differential scanning calorimetry (DSC) analysis in a TA Instruments-Q600 instrument using an alumina crucible. Approximately 20 mg of precursor mixture was loaded in the crucible and heated from room temperature to 800 °C with 5 °C/min ramp under a constant air flow of 100 ml/min. Powder XRD data were collected at room temperature on a PANalytical Empyrean powder diffractometer equipped with Cu Kα radiation, a Bragg–Brentano HD optical module and a position-sensitive PIXcel 3D detector. The angular range covered was 2θ = 10-70° and a step size of $\Delta 2\theta$ = 0.008° was used. Rietveld refinement of XRD patterns was carried out using X'Pert Highscore Plus[49] software package employing a pseudo-Voigt function.

Scanning electron microscopy (SEM) images and energy-dispersive X-ray spectroscopy (EDX) were performed on a Hitachi-S3000 instrument. Optical analyses of the bulk powder samples were performed on a Perkin-Elmer Lambda 35 UV-vis spectrophotometer equipped with an integrating sphere over the range of 400-1000 nm. The Kubelka-Munk transformation (eq 4) was applied to transform diffuse reflectance (R) to absorption coefficient, α[50]

$$F(R) = \frac{\alpha}{s} = \frac{(1 - R_\infty)^2}{2\,R_\infty} \qquad (4)$$

Energy bandgaps were estimated using the Tauc plot based on eq 5[50]

$$h\nu = \alpha(h\nu - E_g)^n \qquad (5)$$

Here, E_g denotes the bandgap and *n* represents the mode of transition, i.e., n = 1/2 for direct transition and n = 2 for indirect transition.

4.2.4 Electrode Preparation and Photoelectrochemical Measurements. Electrodes of the various samples were prepared from bulk powder using spray-coating. Details of the preparation can be found elsewhere.[51] The photoelectrochemical (PEC) measurements were performed in a classical one-compartment, three-electrode electrochemical cell (CH Instruments, Model CHI720C). A Ag/AgCl/4M KCl electrode was used as the reference and a Pt wire was used as the counterelectrode. All potentials in this study are reported versus the reversible hydrogen electrode according to eq 6.

$$\mathrm{E_{RHE}} = \mathrm{E_{Ag/AgCl}} + 0.0591\mathrm{pH} + \mathrm{E^0_{Ag/AgCl(4\ M\ KCl)}} \qquad (6)$$

$$\mathrm{E^0_{Ag/AgCl(4\ M\ KCl)}} = 0.1976\ \mathrm{V\ vs\ NHE\ at\ 25\ °C}$$

A 400 W Xe-arc lamp (Newport) was used as the radiation source equipped with an IR filter. The incident light was adjusted to 1 Sun (100 mW/cm^2) at the surface of working electrode using a calibrated Si reference cell (Oriel). Photocurrent measurements were performed in 0.1 M borate buffer (pH 9.2) (in some cases with addition of 0.1 M Na_2SO_3) with potential scan at 1 mVs^{-1} sweep rate.

Photoelectrochemical electrode stability tests employed chronoamperometric measurements at a fixed potential for 2 h. The irradiation was blocked after each 30 min for a few seconds to confirm that dark current remained negligible. ICP-AES analysis of the electrolyte solution after the photostability experiment was performed using a Shimadzu ICPE-9000 instrument.

4.2.5 Kelvin-Probe Microscopy and Surface Photovoltage Spectroscopy. Measurements were performed using a KP Technology APS04 K-probe instrument. First, the Fermi level (E_F) of the 2 mm in diameter gold alloy-coated tip was determined by measuring the Fermi level of a silver reference target ($E_{F,\ Au\ tip}$ = −4.73 eV). Thin films identical to those investigated in the PEC

experiments were studied. The tip was vibrated over the sample surface at a fixed height (~1 mm) and amplitude (0.2 mm), with a constant frequency (70 Hz). Contact potential difference (CPD) was measured between the sample and the Kelvin probe tip after electrical equilibrium was reached. Surface photovoltage spectroscopy (SPV) data were recorded under ambient conditions. The vibrating Kelvin-probe tip functioned as the reference electrode. The samples were illuminated with a 150 W quartz halogen lamp (Fiber-Lite DC950) which was coupled to a monochromator.

4.2.6 Computational Methodology. The present calculations were performed using the density functional theory (DFT)[52,53] as implemented in the Vienna ab initio simulation package (VASP).[54,55] Exchange and correlation were treated through the generalized gradient approximation (GGA) formalized by Perdew-Burke-Ernzerhof (PBE).[56] The projector augmented plane wave (PAW) method[57] was used to treat the core electrons. The Monkhorst-Pack (MP) scheme was used to generate the k-points grid. In the present calculations, a 9×9×5 k-point mesh for α-$Cu_2V_2O_7$, a 9×9×7 k-point mesh for β-$Cu_2V_2O_7$ and γ-$Cu_3V_2O_8$, and a 9×7×5 k-point mesh for α-CuV_2O_6 were used respectively for cell relaxation which gave well-converged results. A plane wave kinetic energy cutoff, E_{cut} of 500 eV for α-$Cu_2V_2O_7$, 550 eV for β-$Cu_2V_2O_7$, 600 eV for γ-$Cu_3V_2O_8$ and α-CuV_2O_6 were used respectively throughout the calculations. Effective U values (U_{eff}) of 3.1 eV and 5.0 eV were used for the strongly correlated d electrons of V and Cu respectively. The visualization software, VESTA was used to visualize and analyze the crystal structure.[58]

4.3 RESULTS AND DISCUSSION

Malic acid served as both fuel and chelating agent in the precursor mixture for SCS. A possible mechanism of complexation can be inferred from earlier reports.[59,60] In this scheme, $Cu(NO_3)_2$ and NH_4VO_3 dissolved in the solution by forming their respective ions (eqs 7-8). Malic acid (MA) served as a chelating agent for these metal ions leading to the formation of a polymeric complex network (eq 9).

$$Cu(NO_3)_2 \rightarrow Cu^{2+} + 2NO_3^- \quad (7)$$

$$NH_4VO_3 \rightarrow NH_4^+ + VO_3^- \quad (8)$$

$$Cu^{2+} \quad MA + VO_3^- \quad MA \rightarrow \quad Cu^{2+} \quad MA \quad VO_3^- \quad MA \quad (9)$$

Once the ignition temperature was attained, combustion of MA led to thermal breakdown of the complex and culminated in oxide formation. The SCS process can be simulated[61,62] by heating the precursor mixture in a TGA/DSC analysis environment; Figure 4-2 contains the TGA and DSC results for the formation of CuV_2O_6.

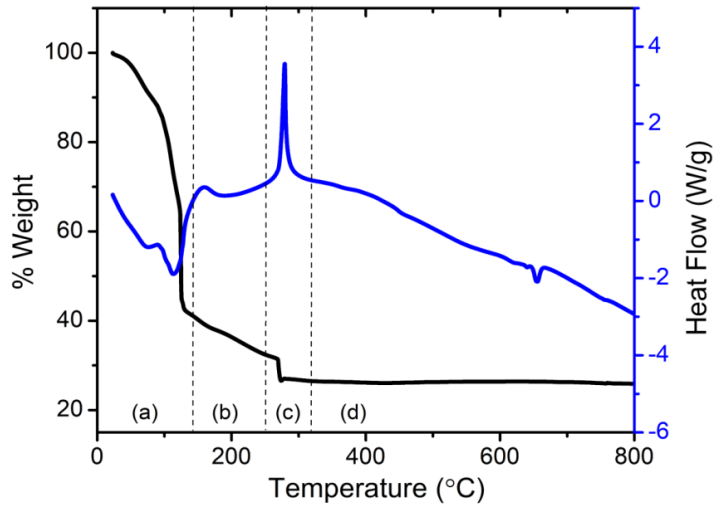

Figure 4-2. Simulation of solution combustion synthesis using TGA/DSC analysis for CuV_2O_6.

The TGA/DSC trace can be divided into four distinct regions: (a) evaporation of water (b) complexation of ions (see above) and removal of hydrated water (c) ignition and combustion and, (d) removal of any carbonaceous remnant as well as product anneal. The first step was dehydration, which is an endothermic process and reflected in the DSC trace as a peak with negative heat flow. Once all the water evaporated, further heating caused removal of hydrated water and ionization-complexation of the precursor mixture which was then ignited (Region c) with a positive heat flow peak in DSC trace. In the case of CuV_2O_6, the ignition temperature appeared at ~280 °C. As the combustion reaction took place only for a short time (a few min), the as-synthesized sample contained a mixture of amorphous and crystalline compounds which upon further heating yielded well-defined crystalline products (see below).

The effect of different anneal temperatures on the as-synthesized CuV_2O_6 sample is presented in the XRD data in Figure 4-3a. Annealing at 550 °C showed a well-defined triclinic α-CuV_2O_6 phase along with the minority phase, α-$Cu_2V_2O_7$. Increasing the anneal temperature to 600 °C resulted in a diminution of the α-$Cu_2V_2O_7$ phase. Further increasing the anneal temperature to 610 °C led to the formation of another compound in admixture, assigned as β-CuV_2O_6. Synthesis of α-CuV_2O_6 using electrospray and sol-gel methods also reported mixed phase oxides[14,15] presumably arising from their similar thermal history.

On the other hand, $Cu_2V_2O_7$ crystallized in two stable polymorphs, namely, low temperature β-$Cu_2V_2O_7$ (zeisite) and high temperature α-$Cu_2V_2O_7$ (blossite) as shown in Figure 4-3b. Notably, these phases were pure unlike in the CuV_2O_6 case above. Thermal anneal at 500 °C for 1 h yielded a high purity β-polymorph which started transforming to α-polymorph at higher temperatures; complete transformation occurred at 610 °C. These observations on the SCS samples are consistent

with earlier reports on Cu-V-O samples synthesized by other methods, which showed the β to α transition at 605-610 °C.[19]

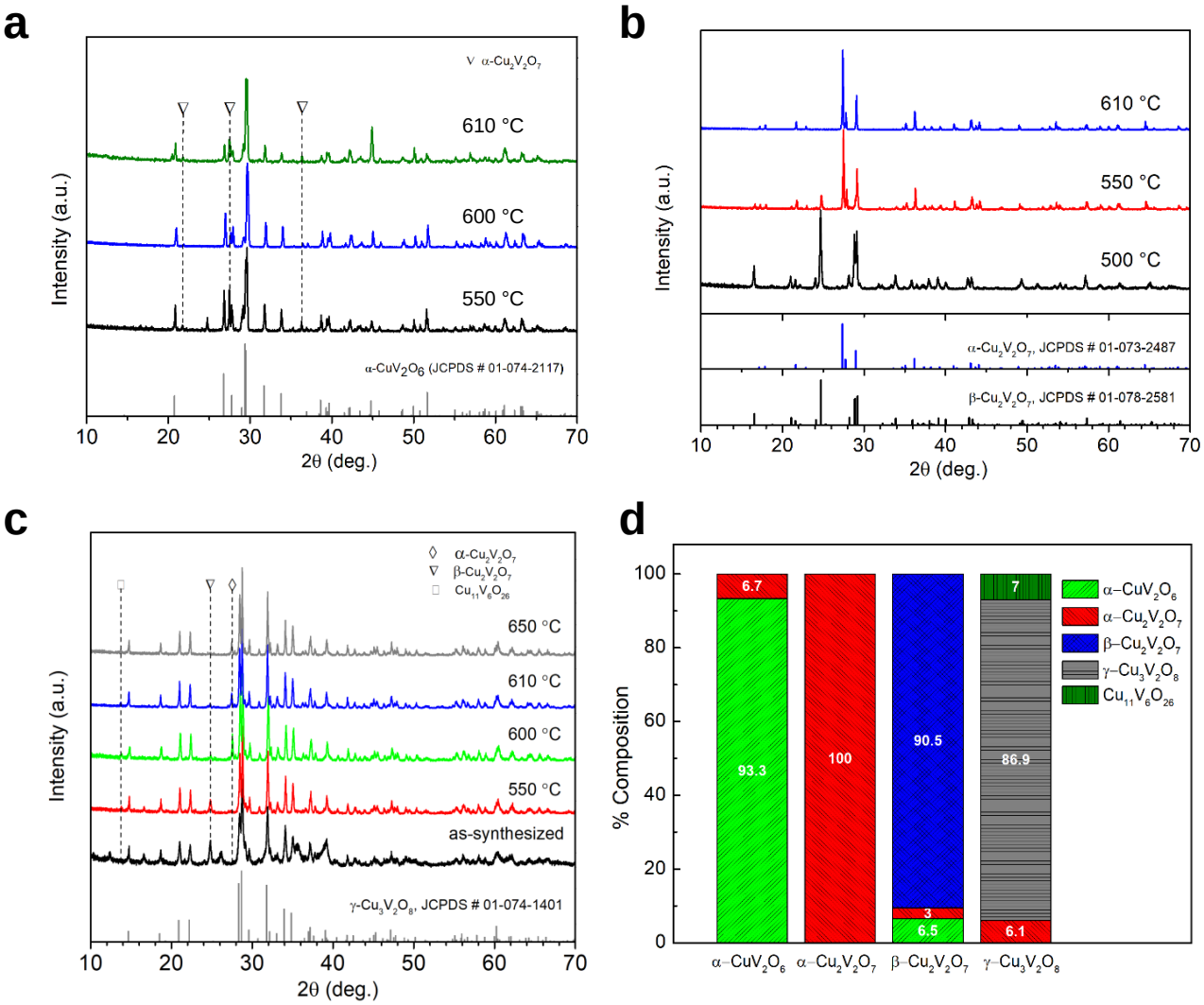

Figure 4-3. XRD-patterns of as-synthesized samples (a) CuV_2O_6 (b) $Cu_2V_2O_7$, (c) $Cu_3V_2O_8$ and (d) phase compositions from Rietveld refinement. In panels a-c, the minority components are marked with dashed lines.

The SCS of $Cu_3V_2O_8$ showed behavior contrasting the other two compounds with lower Cu content. The as-synthesized sample showed mostly the crystalline phase of γ-$Cu_3V_2O_8$ along with zeisite (β-$Cu_2V_2O_7$) (Figure 4-3c). Although we expected the formation of the low temperature

polymorph, β-$Cu_3V_2O_8$ (pseudolynsite),[44] the formation of the high temperature modification, γ-$Cu_3V_2O_8$ was presumably favored by the SCS environment. Once we annealed the as-synthesized sample, zeisite (β-$Cu_2V_2O_7$) transformed to blossite (α-$Cu_2V_2O_7$). At 550 °C for 1h, γ-$Cu_3V_2O_8$ co-existed with both α and β- $Cu_2V_2O_7$ while at 600 °C, complete conversion of β-$Cu_2V_2O_7$ to α-$Cu_2V_2O_7$ occurred. However, $Cu_2V_2O_7$ was always present in admixture with γ-$Cu_3V_2O_8$, a trend which also corroborates previous reports which show that γ-$Cu_3V_2O_8$ cannot be found as a single pure phase.[25]

Rietveld refinement was used to determine the crystal systems, unit cell parameters (Table B-S1) and compositions of different phases present in the SCS sample. Figure B-S1 represents the refinement of four compounds. For α-CuV_2O_6, the XRD pattern of the sample annealed at 600 °C was employed for the refinement while the XRD pattern of γ-$Cu_3V_2O_8$ at 610 °C was used for refinement. More details on the refinement results are presented in Table B-S2.

Briefly, Rietveld refinements of the XRD data for the different copper vanadate samples indicated that in the case of α-CuV_2O_6, there was a minority phase of α-$Cu_2V_2O_7$ of ~6.7%. Similarly, β-$Cu_2V_2O_7$ showed two minority phases- α-$Cu_2V_2O_7$ and α-CuV_2O_6 to the extent of ~3.0% and ~6.5% respectively along with the major phase β-$Cu_2V_2O_7$. The γ-$Cu_3V_2O_8$ sample also consisted of two minor phases, α-$Cu_2V_2O_7$ (6.1%) and $Cu_{11}V_6O_{26}$ (7.0%). Figure 4-3d shows the phase composition for the four SCS samples. Morphological characteristics of the annealed samples are presented in Figure B-S2; elemental analyses (via EDX) are contained in Figure B-S3 and Table B-S3.

Turning next to optical properties of the SCS samples, a structural analysis of the four copper vanadates was performed as a prelude to the DFT calculations. Figure 4-4 contains the structures on the left side panels. α-CuV_2O_6 consists of CuO_6 and VO_6 octahedral layers (Figure 4-4a), while

the crystal structures of α-$Cu_2V_2O_7$ and β-$Cu_2V_2O_7$ (Figures 4-4b, c) both share a common feature of CuO_5 square pyramids connected by V_2O_7 (dimerization of two VO_4 tetrahedra). On the other hand, γ-$Cu_3V_2O_8$ (Figure 4-4d) contains a network of two types of Cu motifs: CuO_5 square-pyramids and CuO_4 square-planar units that are cross-linked by VO_4 tetrahedra. Similar structures may be found for α-, β-, and γ-$Cu_2V_2O_7$ in ref 37 and for α-CuV_2O_6, β -$Cu_2V_2O_7$, γ-$Cu_3V_2O_8$, and $Cu_{11}V_6O_{26}$ in ref 16.

The electronic band structures and the partial density of states (PDOS), as estimated using the DFT + U method, are shown in Figure 4-4 (right-hand panels, e-h) for the four different copper vanadates (i.e., α-CuV_2O_6, α-$Cu_2V_2O_7$, β-$Cu_2V_2O_7$, and γ-$Cu_3V_2O_8$ respectively). Because the focus in this study was optical (rather than magnetic), no magnetic ordering was considered here unlike in the two precedent theoretical studies. As shown in the PDOS plots, all four phases have the V 3d states at the conduction band minima and the valence band maxima is mostly O 2p and Cu 3d states and they are strongly hybridized near the Fermi level. Furthermore, the Fermi level is dominated by O 2p states for α-CuV_2O_6, β-$Cu_2V_2O_7$, and γ-$Cu_3V_2O_8$ while Cu 3d states are the dominant contribution at the Fermi level for α-$Cu_2V_2O_7$. These conclusions are in broad accord with the previous theoretical studies.[16,39,47]

For α-CuV_2O_6 and γ-$Cu_3V_2O_8$, the bands were dispersive throughout all high symmetry points. For α-$Cu_2V_2O_7$, the conduction band was less dispersive along the Y→T→Z direction and along A1→Y direction, both conduction and valance bands were less dispersive indicating the effective masses of the electrons and holes. For β-$Cu_2V_2O_7$, both conduction and valence bands were flat along the X→Y1→H1 direction which also indicates that the carriers are "heavy." For all the copper vanadates studied, the valence band was composed of Cu 3d and O 2p and the conduction band was mostly V 3d states. Because the d-d transition is forbidden, the transition is predicted to

occur from occupied O 2p to unoccupied V 3d states. It is worth noting here that among other copper vanadates α-CuV_2O_6 would be a prominent photoabsorber because of its direct bandgap and dispersed band on both valence band maxima and conduction band minima.

All the copper vanadates in this study showed indirect bandgaps except α-CuV_2O_6. The calculated indirect band gap values for α-$Cu_2V_2O_7$, β-$Cu_2V_2O_7$, and γ-$Cu_3V_2O_8$ were 2.12, 2.28, and 2.11 eV, respectively, whereas the direct band gap value for α-CuV_2O_6 was 1.89 eV. Diffuse reflectance spectroscopy was employed to experimentally determine the absorbance coefficient of these oxides (c.f., Figure B-S4). While all the SCS samples strongly absorbed visible radiation, weak absorbance was detected below the absorption cutoff. Similar behavior was also found in the previous reports.[25,26] The reason for the weak absorption is believed to be due to the on-site excitation of *d*-shell electrons into the half-filled Cu $d_{x^2-y^2}$ orbitals of Cu^{2+}.[25]

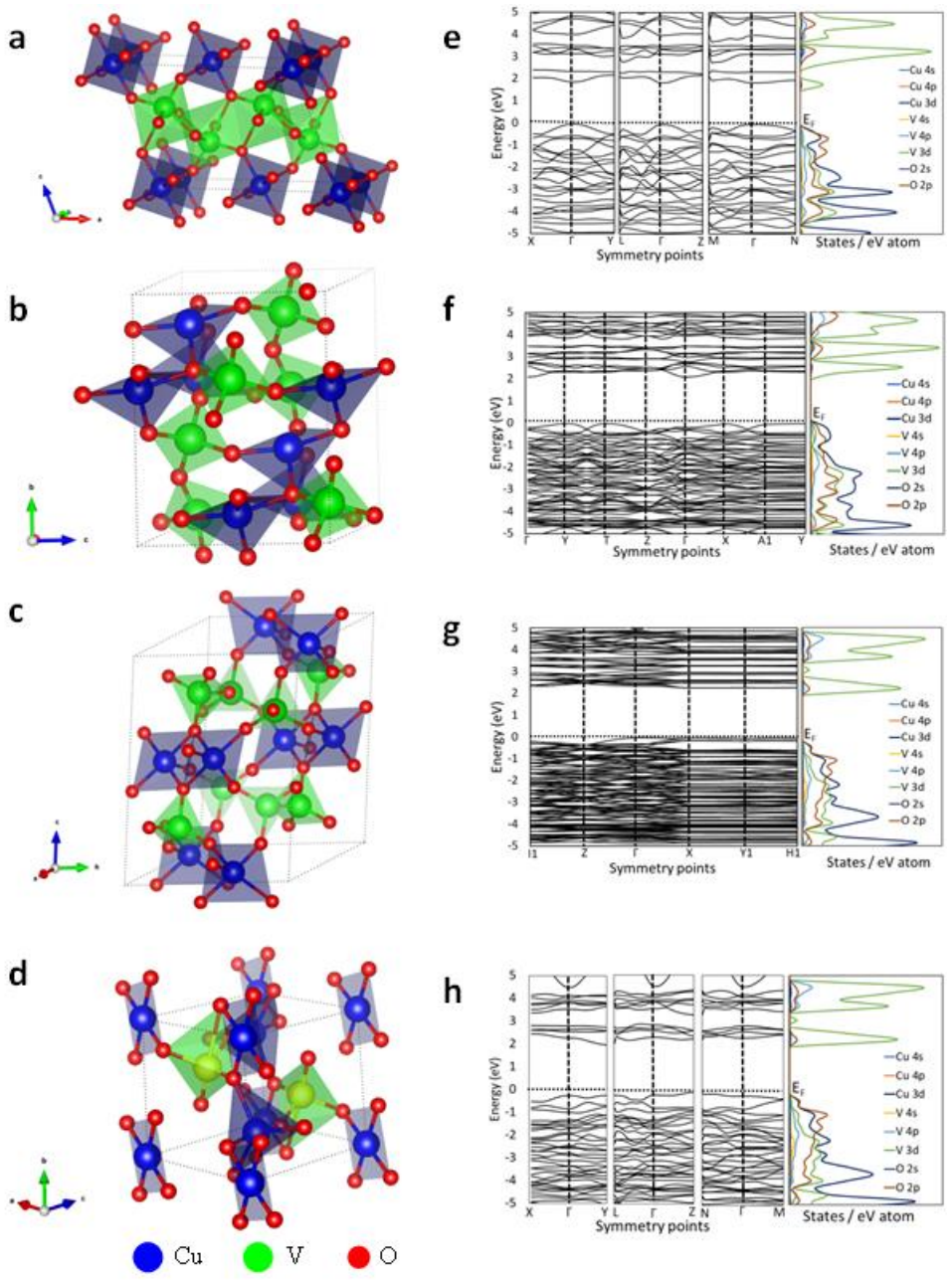

Figure 4-4. Chemical structures (panels a-d) and electronic band structures and density of states (DOS) (panels e-h) for α-CuV_2O_6 (a, e), α-$Cu_2V_2O_7$ (b, f), β-$Cu_2V_2O_7$ (c, g) and γ-$Cu_3V_2O_8$ (d, h). The unit cells are shown on panels a-d as dashed lines.

Table 4-3. Experimental and calculated bandgap values[a] along with literature data.

oxide	E_F / eV	theoretical bandgap (ev)	experimental bandgap (ev)		reported experimental bandgap	refs
			DRS	SPS		
α-CuV_2O_6	-4.91	1.89 (direct)	2.09 (direct) 2.07	1.76	1.96	10,12
α-$Cu_2V_2O_7$	-4.93	2.12	2.13	1.86	1.9 ± 0.1	16
β-$Cu_2V_2O_7$	-4.85	2.28	2.22	1.94	2.0 ± 0.2	10,16
γ-$Cu_3V_2O_8$	-4.89	2.11	2.18	1.73	1.8 ± 0.1	16,25

[a]All the optical transitions are indirect unless otherwise noted.

Previous theoretical and experimental studies suggested that all these oxides have indirect bandgaps.[16,25] However, α-CuV_2O_6 showed a direct transition in our theoretical study (see above) although the difference between indirect and direct bandgaps was very low (0.02 eV). Table 4-3 shows a comparison among the theoretical and experimental bandgaps along with the reported literature bandgaps. Clearly, our experimental bandgaps agree well with theoretically derived values as well as reported data in the literature on samples synthesized by other methods. The systematic discrepancy between the values derived from DRS and SPS (fourth and fifth columns in Table 4-3) will be addressed later.

The PEC activity of the four SCS-derived copper vanadate samples were evaluated using linear sweep voltammetry scan under chopped irradiation (Figure 4-5a). Sodium borate buffer (0.1 M, pH ~9.2) was used as electrolyte due to improved stability of electrodes as suggested by previous reports.[22,25] Linear sweep voltammograms were obtained sweeping the potentials from open circuit potential (OCP) to the positive directions. All four copper vanadates showed n-type photoactivity (positive photocurrents under reverse bias). Photocurrent onset potentials were found as ~0.8 V vs RHE for all four copper vanadates. However, photocurrents were very low initially and slowly

increased up to 1.0 V vs RHE. Beyond this value, the photocurrents increased gradually with applied positive bias and finally saturation of photocurrents was achieved.

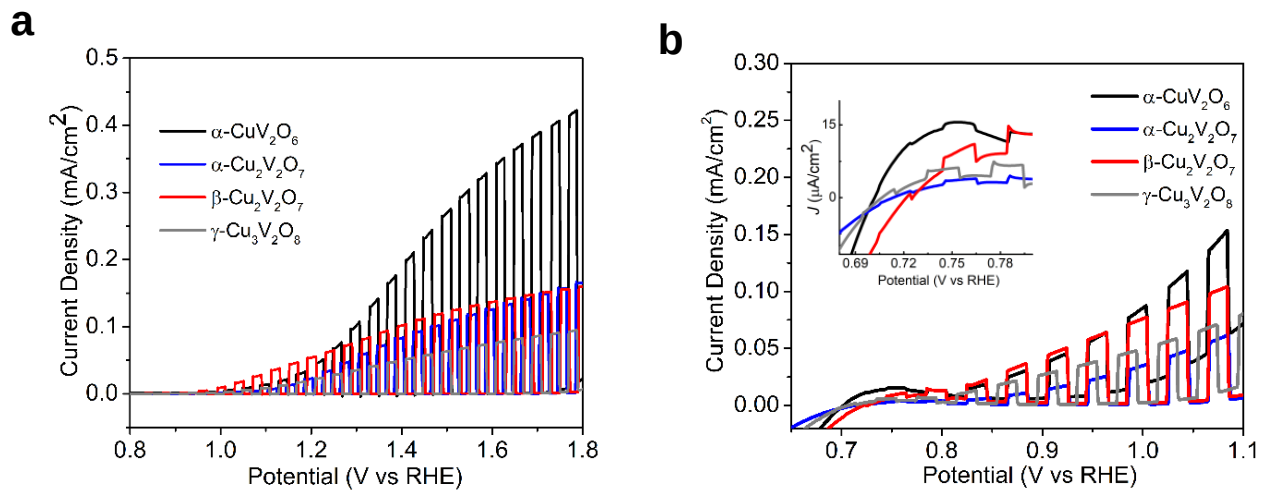

Figure 4-5. Photovoltammogram under interrupted irradiation of the samples (a) in 0.1 M borate buffer solution (pH=9.2) (b) 0.1 M borate buffer solution with 0.1 M Na_2SO_3 (pH 9.2). All linear sweep voltammetry scans were performed under front side illumination with a scan rate of 1 mV/s. Inset of (b) shows an extended view at the onset potential.

Photocurrents (in $\mu A/cm^2$) at the thermodynamic oxidation potential of water (1.23 V vs RHE) were found to be 55, 30, 65, and 25 for α-CuV_2O_6, α-$Cu_2V_2O_7$, β-$Cu_2V_2O_7$, and γ-$Cu_3V_2O_8$ respectively. Admittedly, these photocurrents were quite low; however, some of these values (55 $\mu A/cm^2$ for α-CuV_2O_6 and 65 $\mu A/cm^2$ for β-$Cu_2V_2O_7$) are two-fold higher than the maximum reported photocurrent (25 $\mu A/cm^2$ for α-CuV_2O_6 and 35 $\mu A/cm^2$ for β-$Cu_2V_2O_7$) under similar conditions.[10] These improved photocurrents are attributed to better crystallinity of these SCS-derived oxides as inferred from their XRD patterns. An alternative possibility is the presence of more oxygen vacancies in the samples, although this requires further experimental verification, beyond the scope of the present study.

Interestingly α-CuV_2O_6 showed very little photocurrent at low applied bias, however, the photocurrent increased drastically with applied bias more than 1.2 V vs RHE and attained a maximum value of ~400 μA/cm^2 at 1.8 V vs RHE which is more than two folds compared to other copper vanadates. A previous study[28] showed that surface states in Cu-rich vanadates are responsible for electron−hole recombination; this would be in line with the good performance noted here with the Cu-lean vanadate sample. However, the exceptional high photocurrent of α-CuV_2O_6 can also be correlated with its electronic band structure (see Figure 4-4e) that shows a direct bandgap.

Moreover, the coordination of Cu and V in α-CuV_2O_6(CuO_6 and VO_6 octahedra) are different from the other three copper vanadates (CuO_5 square-pyramid and/or CuO_4 square-planar and VO4 tetrahedra) and hybridize differently. This structural nuance could contribute to a higher mobility of minority carriers through the α-CuV_2O_6 crystal lattice although a separate (solid-state transport) study (beyond the scope of this work) is required to validate this presumption.

Because of the sluggish kinetics of these oxides to water oxidation, photocurrent onset potentials were obtained from sulfite (a kinetically fast hole acceptor) oxidation with the addition of 0.1 M Na_2SO_3 to the 0.1 M borate buffer; these data are shown in Figure 4-5b. The potentials were swept from a value, a little negative of the rest (open circuit) value in a positive direction to accurately record the photocurrent onset potentials (see inset in Figure 4-5b). The onset of photocurrents shifted toward more negative direction than water oxidation consistent with a previous report.[10,22,25] The onset potentials were found to be 0.72, 0.70, 0.69, and 0.66 V vs RHE for α-CuV_2O_6, α-$Cu_2V_2O_7$, β-$Cu_2V_2O_7$, and γ-$Cu_3V_2O_8$ respectively. Approximating these onset potentials as the flat-band potentials afford estimates of the E_F levels of these oxides. As the conduction band is a few hundred millivolts more negative than the Fermi level,[63] all these oxides

have conduction band minima in the range of 0.65-0.70 V vs RHE (Figure 4-6) in line with reported values.[10,22,25]

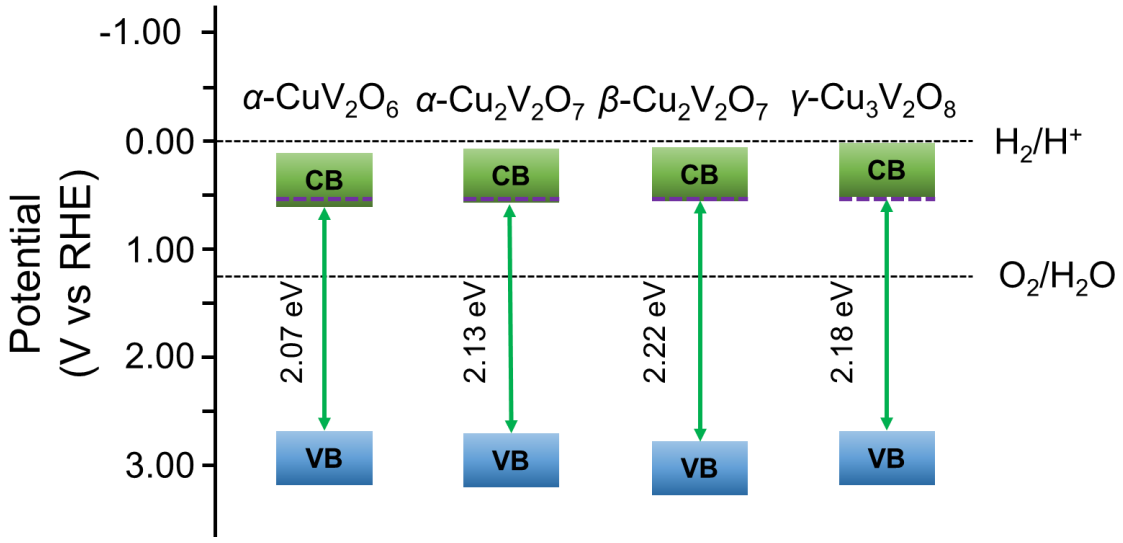

Figure 4-6. Band-edge positions based on experimental photocurrent onsets for the four copper vanadate samples considered in this study. Purple dashed lines show Fermi levels derived from the contact potential difference measurement.

Importantly, note that none of the copper vanadate samples in this study are thermodynamically capable of generating hydrogen from water. This is seen from the fact that the Fermi levels in all the cases lie positive of the hydrogen evolution potential (Figure 4-6). On the other hand, the photogenerated holes in all the cases will have sufficient energy to oxidize water.

The relative insensitivity of the band edge positions as a function of chemical composition in the Cu−V−O system deserves comment. Scrutiny of the conduction band edge position does reveal a slight but systematic shift with greater Cu/V ratio: 0.72, 0.70, 0.69, and 0.66 V versus RHE for α-CuV_2O_6, α-$Cu_2V_2O_7$, β-$Cu_2V_2O_7$, and γ-$Cu_3V_2O_8$, respectively. On the other hand, the valence band edge of V_2O_5 is derived from O 2p orbitals and lies at ∼3.0 V versus NHE. On incorporation of Cu, Cu $3d^9$ hybridizes with O 2p and "lifts" the valence band edge to ∼2.6 V versus NHE.

However, the conduction band edges of both V_2O_5 and copper vanadates are made of V 3d orbitals and hence they lie in similar positions (0.5−0.6 V versus NHE).

The optoelectronic properties were further investigated with Kelvin-probe measurements and surface photovoltage spectroscopy (Figure 4-7a,b). The E_F of the various copper vanadate samples were estimated from their contact potential differences (CPD), Figure 4-7a. The purple dashed lines in Figure 4-6 show the corresponding E_F for each oxide which lie close to the flat-band potential values, determined from the photovoltammograms (see Figure 4-5), as expected for reasonably-doped n-type semiconductors.

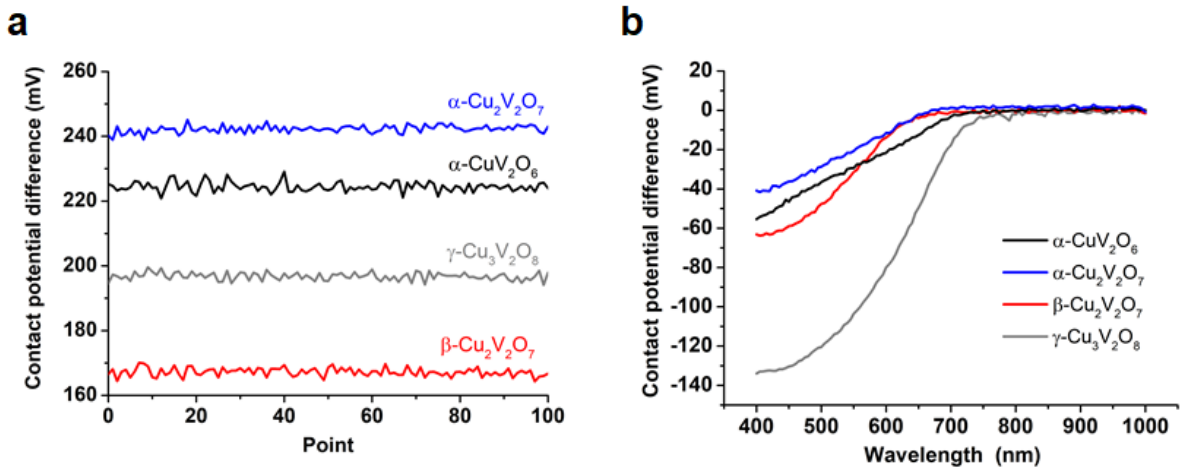

Figure 4-7. Contact potential difference (CPD) (a) and surface photovoltage spectra (b) for the four copper vanadate samples.

The wavelength-dependence of light driven charge separation was monitored by SPV measurements. All spectra show negative photovoltage values (Figure 4-7b), which can be associated with the transfer of electrons to the ITO layer.[64] These data show (and corroborate the trends in Figure 4-5) that all samples behave as n-type semiconductors.[64-66] The highest photovoltage was recorded in the case of the γ-$Cu_3V_2O_8$ sample (≈ −130 mV). Interestingly, this

trend was not reflected by the photovoltammograms, where γ-$Cu_3V_2O_8$ gave the lowest photocurrents. Since the buildup of photovoltage is connected to both charge separation and transport *in the electrode bulk* these data suggest that the reason behind the poor PEC performance is rooted in the sluggish water/sulfite oxidation kinetics on the surface.

Bandgap values (E_{BG}) were determined from the photovoltage onset on the SPV spectra (Table 4-3). These are consistently lower than the values derived from our diffuse reflectance spectroscopy data, but much closer to those reported in the literature. These systematic differences are possibly linked to the higher sensitivity of SPV to sub-bandgap transitions[67] and to the bandwidth of the monochromatic light (i.e., 40 nm).

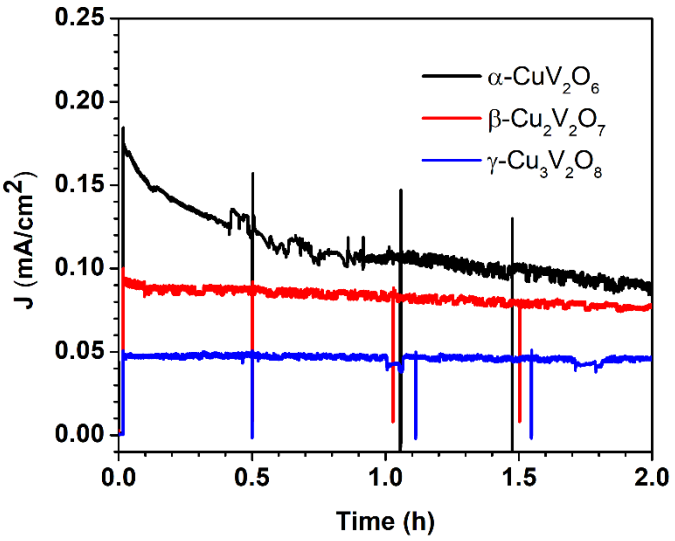

Figure 4-8. Chronoamperometric measurements of copper vanadates at 1.4 V vs RHE in 0.1 M sodium borate buffer (pH 9.2) with 100 mW/cm^2 light intensity.

Finally, the PEC stability of three SCS-derived copper vanadate samples with increasing Cu/V ratio, was compared (Figure 4-8). These chronoamperometric data pertain to a fixed potential of 1.4 V versus RHE under 100 mW/cm^2 irradiation. The photocurrent for the α-CuV_2O_6 sample decreased sharply at the beginning and ~30% of the photocurrent loss took place during the first

30 min. After that time frame, the photocurrent appeared quite stable for at least another 2 h at which time the experiment was discontinued (black curve, Figure 4-8). On the other hand, the photocurrent for β-$Cu_2V_2O_7$ showed a sharp fall during the first 5 min, then slowly decreased and ~20% of photocurrent was lost after 2 h (red curve, Figure 4-8). In contrast, photocurrent loss for γ-$Cu_3V_2O_8$ was negligible after 2 h.

Importantly, this study shows that a higher Cu/V ratio in the copper vanadate compositions renders better PEC stability for the corresponding oxide. We attribute the sharp loss of photocurrent for α-CuV_2O_6 to initial photoleaching of vanadium leaving behind a CuO layer on the surface.[68] Thus, CuO acts as a passive layer for the film, suppressing further corrosion of vanadium from the bulk matrix.[68] Accordingly, the V/Cu ratio in the electrolyte solution after the stability experiment was analyzed using ICP-AES which confirmed the presence of four-times higher V than Cu in the solution. This observation is entirely consistent with the stabilization mechanism proposed by previous authors.[68]

4.4 CONCLUSIONS

The main contribution of the present study and its differentiator from the considerable number of reports that have emerged on copper vanadates is the demonstration that a range of molar stoichiometries from 1:1 to 3:1 in this compound family can be derived simply by tuning the precursor mole ratio in the solution combustion synthesis procedure. Importantly, SCS is very time-efficient and the various compositions can be obtained in a matter of minutes (as opposed to hours or even days in classical solution-based or ceramic synthesis routes, Table 4-1). In this regard, SCS is eminently suited for incorporation into the high throughput screening methods[16,27] that have been deployed for the Cu-V-O family of n-type semiconductors. A secondary feature of this study is that it builds upon the corpus of structural, electronic, and optoelectronic body of information on copper vanadates, derived from a variety of synthetic procedures (c.f., Table 4-1).

While a number of attributes of these family of compounds are appealing from a solar fuels materials design perspective, their charge transport characteristics (limited by small-polaron hopping)[69] certainly would need further optimization, beyond the scope of this particular study.

4.5 REFERENCES

1. Merzhanov, A. G. The Chemistry of Self-Propagating High-Temperature Synthesis. *J. Mater. Chem*. 2004, *14*, 1779-1786.
2. Rajeshwar, K.; de Tacconi, N. R.; Chanmanee, W. Combustion Synthesis of Oxide Semiconductors for Solar Energy Conversion and Environmental Remediation. *Chem. Soc. Rev.* 2009, *38*, 1984-1998.
3. Hossain, M. K.; Kecsenovity, E.; Varga, A.; Molanar, M.; Janaky, C.; Rajeshwar, K. Solution Combustion Synthesis of Complex Oxide Semiconductors. *Int. J. Self-Prop. High Temp. Synthesis* 2018, *27*, 129-140.
4. Li, F. T.; Ran, J.; Jaroniec, M.; Qiao, S. Z. Solution Combustion Synthesis of Metal Oxide Nanomaterials for Energy Storage and Conversion. *Nanoscale* 2015, *7*, 17590-17610.
5. Wen, W.; Wu, J. M. Nanomaterials via Solution Combustion Synthesis: A Step Nearer to Controllability. *RSC Adv.* 2014, *4*, 58090-58100.
6. Rajeshwar, K.; McConnell, R.; Licht, S. editors, *Solar Hydrogen Generation: Toward a Renewable Energy Future*, Kluwer Academic, New York (2008).
7. Rajeshwar, K. Photoelectrochemistry and the Environment. *J. Appl. Electrochem*. 1995, *25*, 1067-1082.
8. Rajeshwar, K.; Hossain, M. K.; Macaluso, R. T.; Janáky, C.; Varga A.; Kulesza, P. J. Copper Oxide-Based Ternary and Quaternary Oxides: Where Solid-State Chemistry Meets Solar Fuels. *J. Electrochem. Soc.* 2018, *165*, H1-H15.
9. Hillel, T; Ein-Eli, Y. Copper Vanadate as Promising High Voltage Cathodes for Li Thermal Batteries. *J. Power Sources* 2013, *229*, 112-116.
10. Guo, W.; Chemelewski, W. D.; Mabayoje, O.; Xiao, P.; Zhang, Y.; Mullins, C. B. Synthesis and Characterization of CuV_2O_6 and $Cu_2V_2O_7$: Two Photoanode Candidates for Photoelectrochemical Water Oxidation. *J. Phys. Chem. C* 2015,*119*, 27220–27227.
11. Newhouse, P. F.; Boyd, D. A.; Shinde, A.; Guevarra, D.; Zhou, L.; Soedarmadji, E.; Li, G.; Neaton, J. B.; Gregoire, J. M. Solar Fuel Photoanodes Prepared by Inkjet Printing of Copper Vanadates. *J. Mater. Chem. A* 2016, *4*, 7483-7494.
12. Khan, I.; Qurashi, A. Shape Controlled Synthesis of Copper Vanadate Platelet Nanostructures, Their Optical Band Edges, and Solar-Driven Water Splitting Properties. *Sci. Rep.* 2017, *7*, 14370.
13. Cao, J. Q.; Wang, X. Y., Tang, A.; Wang, X.; Wang, Y.; Wu, W. Sol–gel Synthesis and Electrochemical Properties of CuV_2O_6 Cathode Material. *J. Alloys Compd.* 2009, *479*, 875-878.
14. Kim, M. W.; Joshi, B.; Yoon, H.; Ohm, T. Y.; Kim, K.; Al-Deyab, S. S.; Yoon, S. S. Electrosprayed Copper Hexaoxodivanadate (CuV_2O_6) And Pyrovanadate ($Cu_2V_2O_7$) Photoanodes for Efficient Solar Water Splitting. *J. Alloys Compd.* 2017, *708*, 444-450.
15. Ma, H.; Zhang, S.; Ji, W.; Tao, Z.; Chen, J. α-CuV_2O_6 Nanowires: Hydrothermal Synthesis and Primary Lithium Battery Application. *J. Am. Chem. Soc.* 2008, *130*, 5361-5367.

16. Zhou, L.; Yan, Q.; Shinde, A.; Guevarra, D.; Newhouse, P. F.; Becerra-Stasiewicz, N.; Chatman, S. M.; Haber, J. A.; Neaton, J. B.; Gregoire, J. M. High Throughput Discovery of Solar Fuels Photoanodes in the CuO-V_2O_5 System. *Adv. Energy Mater.* 2015, *5*, 1500968.
17. He, Z.; Ueda, Y. Flux Growth of β-$Cu_2V_2O_7$ Single Crystals in a Closed Crucible. *Cryst. Growth Des.* 2008, *8*, 2223-2226.
18. Clark, G.M.; Garlick, R. Formation and Properties of Copper (II) Divanadate (V). *J. Inorg. Nucl. Chem.* 1978, *40*, 1347-1349.
19. Slobodin, B. V.; Surat, L. L.; Samigullina, R. F. Polymorphism in Copper Pyrovanadate. *Russ. J. Inorg. Chem.* 2009, *54*, 797-802.
20. Rogado, N.; Haas, M. K.; Lawes, G.; Huse, D. A.; Ramirez, A. P.; Cava, R. J. β-$Cu_3V_2O_8$: Magnetic Ordering in a Spin-1/2 Kagomé-Staircase Lattice. *J. Phys.: Condens. Matter* 2003, *15*, 907-914.
21. Wang, M.; Liu, Q. Synthesis and Photocatalytic Property of $Cu_3V_2O_8$ Prepared by Liquid Phase Precipitation. *Adv. Mater. Res.* 2011, *236*, 1675-1678.
22. Seabold, J. A.; Neale, N. R. All First Row Transition Metal Oxide Photoanode for Water Splitting Based on $Cu_3V_2O_8$. *Chem. Mater.* 2015, *27*, 1005–1013.
23. Zhang, S.; Sun, Y.; Li, C.; Ci, L. $Cu_3V_2O_8$ Hollow Spheres in Photocatalysis and Primary Lithium Batteries. *Solid State Sci.* 2013, *25*, 15-21.
24. Li, M.; Gao, Y.; Chen, N.; Meng, X.; Wang, C.; Zhang, Y.; Zhang, D.; Wei, Y.; Du, F.; Chen, G. $Cu_3V_2O_8$ Nanoparticles as Intercalation-Type Anode Material for Lithium-Ion Batteries. *Chem. Eur. J* 2016, *22*, 11405-11412.
25. Jiang, C. M.; Farmand, M.; Wu, C. H.; Liu, Y. S.; Guo, J.; Drisdell, W. S.; Cooper, J. K.; Sharp, I. D. Electronic Structure, Optoelectronic Properties, and Photoelectrochemical Characteristics of γ-$Cu_3V_2O_8$ Thin Films. *Chem. Mater.* 2017, *29*, 3334−3345.
26. Lumley, M. A.; Choi, K.-S. Investigation of Pristine and (Mo, W)-Doped $Cu_{11}V_6O_{26}$ for Use as Photoanodes for Solar Water Splitting. *Chem. Mater.* 2017, *29*, 9472–9479.
27. Yan, Q.; Yu, J.; Suram, S. K.; Zhou, L.; Shinde, A.; Newhouse, P. F.; Chen, W.; Li, G.; Persson, K. A.; Gregoire, J. M.; Neaton, J. B. Solar Fuels Photoanode Materials Discovery by Integrating High-Throughput Theory and Experiment. *PNAS*, 2017, *114*, 3040-3043.
28. Jiang, C.-M.; Segev, G.; Hess, L. H.; Liu, G.; Zaborski, G.; Toma, F. M.; Cooper, J. K.; Sharp, I. D. Composition-Dependent Functionality of Copper Vanadate Photoanodes. *Appl. Mater. Interfaces 2*018, *10*, 10627-10633.
29. Cardenas-Morcoso, D.; Peiro-Franch, A.; Herraiz-Cardona, I.; Gimenez, S. Chromium Doped Copper Vanadate Photoanodes for Water Splitting. *Catal. Today* 2017, *290*, 65−72.
30. Brisi, C.; Molinari, A. Sistema Osido Ramicoanidride Vanadica. *Ann. Chim.* 1958, *48*, 263-269.
31. Fleury, P. The CuO-V_2O_5 System. *Compt Rend Acad Sci* 1966, *265*, 1375-1377.
32. Shannon, R. D.; Calvo, C. Crystal Structure of a New Form of $Cu_3V_2O_8$. *Can. J. Chem.* 1972, *50*, 3944-3949.
33. Cao, X.; Xie, J.; Zhan, H.; Zhou, Y. Synthesis of CuV_2O_6 as a Cathode Material for Rechargeable Lithium Batteries from V_2O_5 Gel. *Mater. Chem. Phys.* 2006, *98*, 71-75.
34. Zhang, S.; Ci, L.; Liu, H. Synthesis, Characterization, and Electrochemical Properties of $Cu_3V_2O_7(OH)_2{\cdot}2H_2O$ Nanostructures. *J. Phys. Chem. C* 2009, *113*, 8624-8629.

35. Zhang, S.; Hou, M.; Lu, M. Synthesis and Electrochemical Performance of Cable-Like Copper Vanadates/Polypyrrole Nanobelts as Anode Materials for Lithium-Ion Batteries. *Chem. Phys. Lett.* 2016, *658*, 203-206.
36. Dai, J.; Lai, M.; LaFollette, R. M.; Reisner, D. Thin Film Copper Vanadium Oxide Electrodes for Thermal Batteries. *ECS Trans.* 2011, *33*, 3-9.
37. Bhowal, S.; Sannigrahi, J.; Majumdar, S.; Dasgupta, I. A Comparative Study of Electronic, Structural, and Magnetic Properties of α-, β-, and γ−$Cu_2V_2O_7$. *Phy. Rev. B* 2017, *95*, 075110.
38. Prokofiev, A. V.; Kremer, R. K.; Assmus, W. Crystal Growth and Magnetic Properties of α-CuV_2O_6. *J. Cryst. Growth* 2001, *231*, 498-505.
39. Yashima, M.; Susuki, R. O. Electronic Structure and Magenetic Propertiies of Monoclinic β-$Cu_2V_2O_7$: A GCA + U Study. *Phys. Rev. B* 2009, *79*, 125201-1-125201-6.
40. Ghiyasiyan-Arani, M.; Masjedi-Arani, M.; Ghanbari, D.; Bagheri, S.; Salavati-Niasari, M. Novel Chemical Synthesis and Characterization of Copper Pyrovanadate Nanoparticles and its Influence on the Flame Retardancy of Polymeric Nanocomposites. *Sci. Rep.* 2016, *6*, 25231.
41. Machida, M.; Kawada, T.; Hebishima, S.; Hinokuma, S.; Takeshima, S. Macroporous Supported Cu-V Oxide as a Promising Substitute as the Pt catalyst for Sulfuric Acide Decomposition in Solar Thermochemical Hydrogen Production. *Chem. Mater*. 2012, *24*, 557-561.
42. Kawada, T.; Tajiri, T.; Yamashita, H.; Machida, M. Molten Copper Hexaoxodivanadate: An Efficient Catalyst of SO_3 Decomposition in Solar Thermochemical Water Splitting Cycles. *Catal. Sci. Technol.* 2014, *4*, 780-785.
43. Kawada, T.; Hinokuma, S.; Machida, M. Structure and SO_3 Decomposition Activity of nCuO-V_2O_5/SiO_2 (n = 0,1,2,3 and 5) Catalysts for Solar Thermochemical Water Splitting Cycles. *Catal. Today* 2015, *242*, 268-273.
44. Rao, N. S.; Palanna, O. G. Phase Transitions in Copper (II) Orthovanadate. *Bull. Mater. Sci.* 1993, *16*, 261-266.
45. Krivovichev, S. V.; Filatov, S. K.; Cherepansky, P. N.; Armbruster, T.; Pankratova, O. Y. Crystal Structure of γ-$Cu_2V_2O_7$ and its Comparison to Blossite (α-$Cu_2V_2O_7$) and Ziesite (β-$Cu_2V_2O_7$). *Can. Mineral.* 2005, *43*, 671-677.
46. Slobodin, B.V.; Samigullina, R. F. Thermoanalytical Study of the Polymorphism and Melting Behavior of $Cu_2V_2O_7$. *Inorg. Mater.* 2010, *46*, 196-200.
47. Jerzierski, A.; Kaczkowski, J. Electronic Structure and Thermodynamic Properties of $Cu_3V_2O_8$ Compound. *Phase Trans.* 2015, *88*,970-978.
48. Denisova, L. T.; Belousova, N. V.; Denisov, V. M.; Galiakhmetova, N. A. High-Temperature Heat Capacity of Oxides in the CuO-V_2O_5 System. *Phys. Solid State* 2019, *59*, 1270-1274.
49. Degen, T.; Sadki, M.; Bron, E.; Kö nig, U.; Nenert, G. The´ HighScore Suite. *Powder Diffr.* 2014, *29*, S13−S18.
50. Roy, D.; Samu, G. F.; Hossain, M. K.; Janáky, C.; Rajeshwar, K. On the Measured Optical Bandgap Values of Inorganic Oxide Semiconductors for Solar Fuels Generation. *Catal. Today* 2018, *300*, 136-144.
51. Hossain, M. K.; Samu, G. F.; Gandha, K.; Santhanagopalan, S.; Liu, J. P.; Janáky, C.; Rajeshwar, K. Solution Combustion Synthesis, Characterization, and Photocatalytic Activity of $CuBi_2O_4$ and its Nanocomposites with CuO and α-Bi_2O_3. *J. Phys. Chem. C* 2017, *121*, 8252-8261.
52. Hohenberg, P.; Kohn, W. Inhomogeneous Electron Gas. *Phys. Rev.*1964, *136*, B864.

53. Kohn, W.; Sham, L. J. Self-Consistent Equations Including Exchange and Correlation Effects. *Phys. Rev.* 1965, *140*, A1133-A1138.
54. Kresse, G.; Furthmüller, J. Efficiency of Ab Initio Total Energy Calculations for Metals and Semiconductors Using a Plane-Wave Basis Set. *Comput. Mater. Sci.* 1996, *6*, 15-50.
55. Kresse, G.; Furthmüller, J. Efficient Iterative Schemes for Ab Initio Total-Energy Calculations Using a Plane-Wave Basis Set. *Phys. Rev. B* 1996, *54*, 11169-11186
56. Perdew, J. P.; Burke, K.; Ernzerhof, M. Generalized Gradient Approximation Made Simple. *Phys. Rev. Lett.* 1996, *77*, 3865-3868.
57. Blöchl, P. E. Projector Augmented-Wave Method. *Phys. Rev. B* 1994, *50*, 17953-17979.
58. Momma, K.; Izumi, F. VESTA: A Three-Dimensional Visualization System for Electronic and Structural Analysis. *Appl. Crystallogr.* 2008, *41*, 653-658.
59. Nagabhushana, G. P.; Nagaraju, G.; Chandrappa, G. T. Synthesis of Bismuth Vanadate: its Application in H_2 evolution and Sunlight-Driven Photodegradation. *J. Mater. Chem. A* 2013, *1*, 388-394.
60. Kakihana, M. Sol-Gel Preparation of High Temperature Superconducting Oxides. *J. Sol-Gel Sci. Technol.* 1996, *6*, 7-55.
61. Thomas, A.; Janáky, C.; Samu, G. F.; Huda, M. N.; Sarker, P.; Liu, J. P.; Van Nguyen, V.; Wang, E. H.; Schug, K. A.; Rajeshwar, K. Time- and Energy- Efficient Solution Combustion Synthesis of Binary Metal Tungstate Nanoparticles with Enhanced Photocatalytic Activity. *ChemSusChem* 2015, *8*, 1652−1663.
62. Kormányos, A.; Thomas, A.; Huda, M. N.; Sarker, P.; Liu, J. P.; Poudyal, N.; Janáky, C.; Rajeshwar, K. Solution Combustion Synthesis, Characterization, and Photoelectrochemistry of $CuNb_2O_6$ and $ZnNb_2O_6$ Nanoparticles. *J. Phys. Chem. C* 2016, *120*, 16024−16034.
63. For example: Rajeshwar, K. Fundamentals of Semiconductor Electrochemistry and Photoelectrochemistry, in *Encyclopedia of Electrochemistry* (Edited by Licht, S.), Chapter 1, 3-53, Wiley-VCH, Weinheim (2001).
64. Ma, X.; Cui, X.; Zhao, Z.; Melo, M. A.; Roberts, E. J.; Osterloh, F. E. Use of Surface Photovoltage Spectroscopy to Probe Energy Levels and Charge Carrier Dynamics in Transition Metal (Ni, Cu, Fe, Mn, Rh) Doped $SrTiO_3$ Photocatalysts for H_2 evolution from Water. *J. Mater. Chem. A* 2018, *6*, 5774–5781.
65. Wu, Z.; Cheung, G.; Wang, J.; Zhao, Z.; Osterloh, F. E. Wavelength Dependent Photochemical Charge Transfer at the Cu_2O–$BiVO_4$ Particle Interface – Evidence for Tandem Excitation. *Chem. Commun.* 2018, *54*, 9023–9026.
66. Kwolek, P.; Szaciłowski, K. Photoelectrochemistry of n-Type Bismuth Oxyiodide. *Electrochim. Acta* 2013, *104*, 448–453.
67. Kronik, L.; Shapira, Y. Surface Photovoltage Spectroscopy of Semiconductor Structures: At the Crossroads of Physics, Chemistry and Electrical Engineering. *Surf. Interface Anal.* 2001, *31*, 954–965.
68. Zhou, L.; Yan, Q.; Yu, J.; Jones, R.J.; Becerra-Stasiewicz, N.; Suram, S.K.; Shinde, A.; Guevarra, D.; Neaton, J.B.; Persson, K.A.; Gregoire, J.M. Stability and Self-Passivation of Copper Vanadate Photoanodes Under Chemical, Electrochemical, and Photoelectrochemical Operation. *Phys. Chem. Chem. Phys.* 2016, *18*, 9349-9352.
69. Gupta, S.; Yadava, Y. P.; Singh, R. A. Electrical-Conduction in Copper Vanadate. *Z. Phys. B: Condens. Matter* 1987, 67, 179−183.

CHAPTER 5

SUMMARY AND PERSPECTIVES

Complex oxides (ternary and quaternary oxides and their composites) have emerged as promising alternatives to binary metal oxides for solar energy conversion and environmental remediation. However, it is no easy task to screen an enormous set of multinary oxides (8,000 ternary and 700,000 quaternary combinations), and this warrants a ***time-efficient*** route of synthesis. In this dissertation, we demonstrated solution combustion synthesis as a time- and energy-efficient synthesis route for generating Cu-based complex oxides in the Cu-Bi-V-O system. Comparative PEC characterizations could also be carried out by synthesizing a family of compounds.

Chapter 2 described a review on solution combustion synthesis for the preparation of complex oxide semiconductors. We showed that a diverse range of complex oxides can be prepared using SCS; this could be easily deployed to tune a range of materials parameters such as morphology, particle size, porosity and surface area, etc.

In chapter 3, we demonstrated the solution combustion synthesis of binary CuO and α-Bi_2O_3 as well as their ternary counterpart $CuBi_2O_4$ by utilizing two different fuels (urea and hexamethylenetertramine). A range of composites from CuO/$CuBi_2O_4$ to $CuBi_2O_4$/α-Bi_2O_3 as the end members were also successfully prepared. Rietveld refinement of the XRD patterns confirmed that the experimental compositions corresponded with theoretical expectations. The photoelectrochemical behavior of the composite samples showed improved photocurrent response

toward solar hydrogen generation than their parent oxide components. This performance enhancement was attributed to vectorial charge transfer across the composite heterojunction.

Chapter 4 discussed the complexation-assisted rapid one-pot synthesis of four copper vanadates (α-CuV_2O_6, α/β-$Cu_2V_2O_7$ and γ-$Cu_3V_2O_8$) by tuning the mole ratio of Cu and V. We hypothesized that the formation of heterobimetallic complex malate facilitated the formation of ternary oxides. Among the four copper vanadates, α-CuV_2O_6 demonstrated superior *n*-type semiconductor behavior toward solar PEC water splitting. This could be attributed to its unique crystal motifs as well as the direct nature of the optical transition from the valence band to the conduction band. However, further works are needed to more completely elucidate the complexation mechanism and tune the reaction parameters (e.g., pH, reactant concentrations, etc.) to get targeted compositions

Another avenue for future work may entail the study of electrode-electrolyte behavior under dark/light conditions of different copper vanadates. This will provide answers to many surface-related questions, such as carrier transport kinetics across the interface, surface states, and photostability, etc. Furthermore, doping of appropriate transition elements (e.g., W, Mo, Nb, and Ta) may be explored to "engineer" the electronic band structures of these semiconductors. In this way, a range of solid solutions can also be prepared.

A final and very important aspect that deserves further scrutiny concerns the photochemical stability of the new-generation semiconductors generated in this dissertation. Practical application of these new families of semiconductor materials entails that they maintain their chemical and electrochemical stability over several hours. The addition of experimental tools such as electrochemical quartz crystal microgravimetry will undoubtedly aid in better understanding of the underlying corrosion mechanisms. Such mechanistic understanding will also contribute to more

effective performance optimization for practical technologies such as water splitting and pollution abatement.

APPENDIX A

SUPPORTING INFORMATION FOR CHAPTER 3

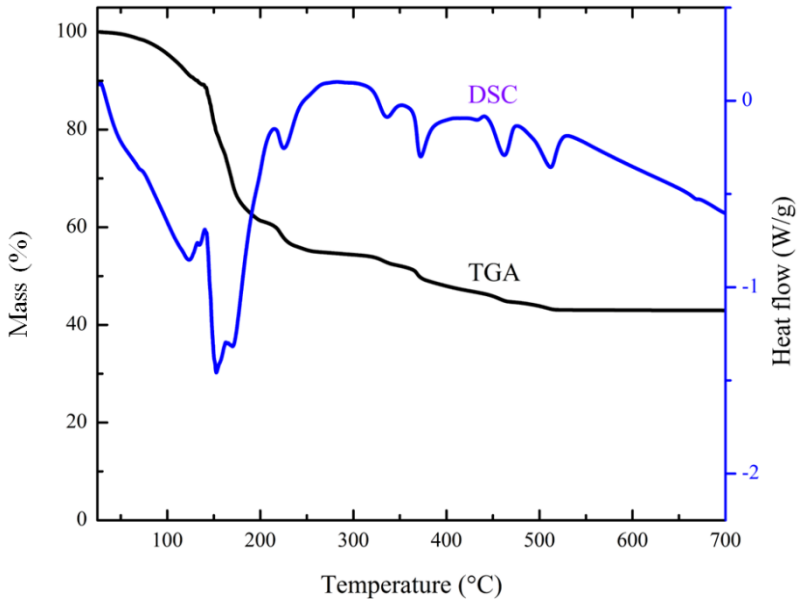

Figure A-S1. TGA-DSC analysis of precursor mixture without fuel. Refer to the experimental section for sample preparation details.

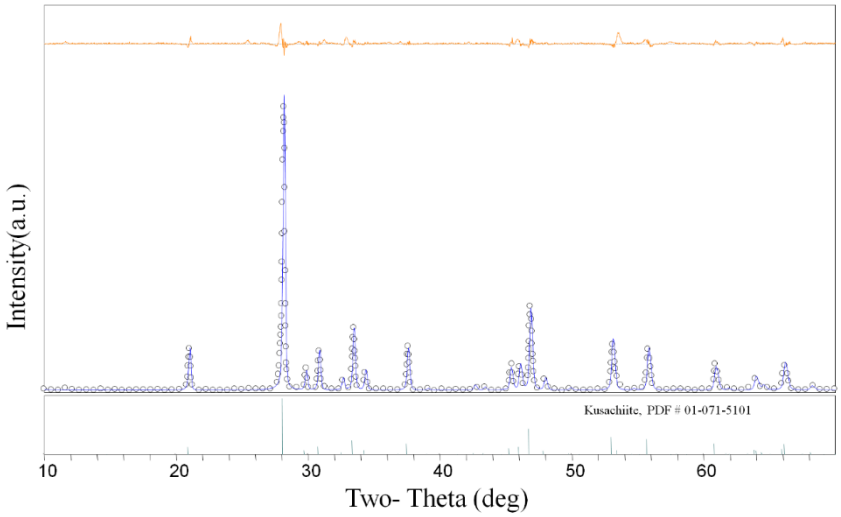

Figure A-S2. Rietveld refinement analysis of annealed $CuBi_2O_4$ (U) showing good agreement with the standard kusachiite (PDF#01-071-5101) (χ^2=2.1).

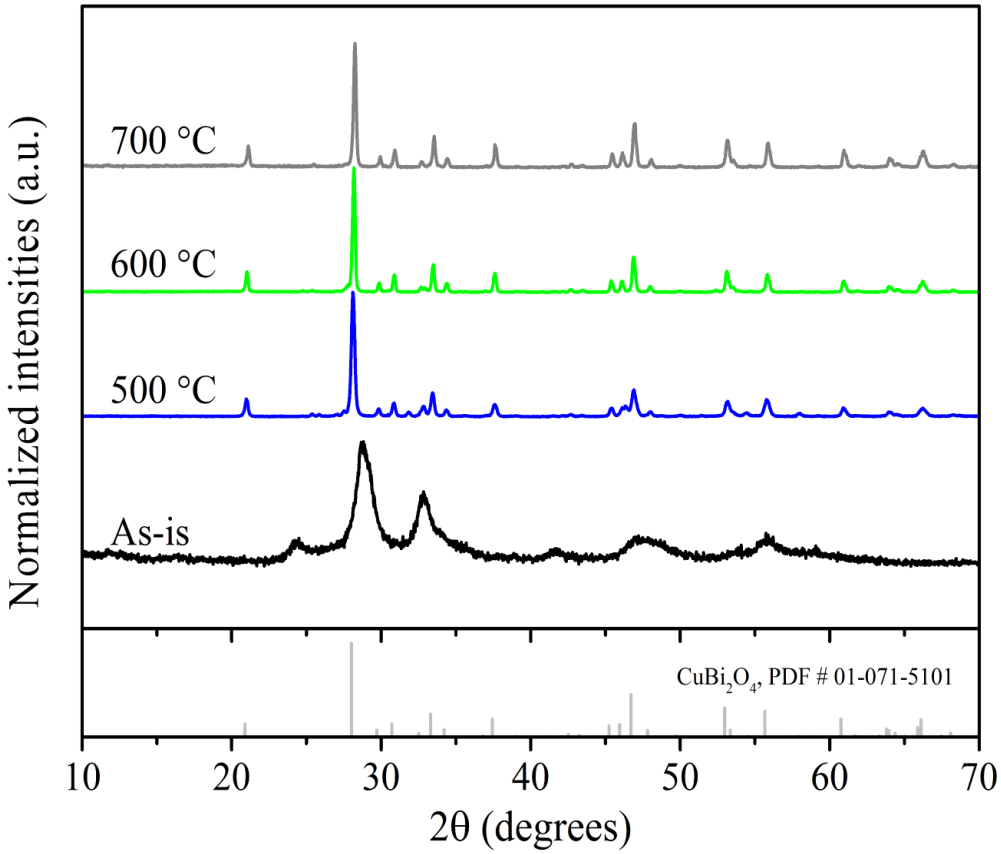

Figure A-S3. Effect of anneal temperature on the crystallinity of as-is $CuBi_2O_4$ (HMT). A standard XRD pattern of $CuBi_2O_4$ (PDF# 01-071-5101) is also shown for reference.

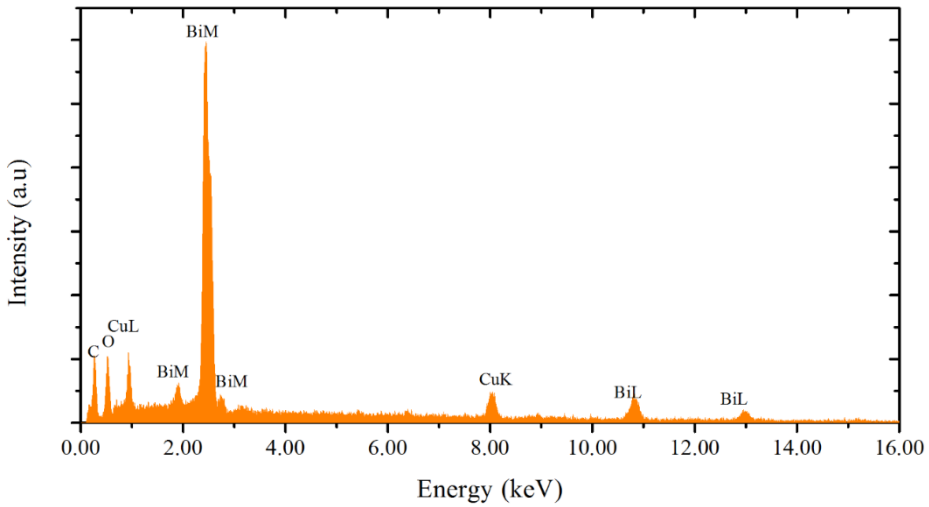

Figure A-S4. EDS spectrum of annealed $CuBi_2O_4$ (U).

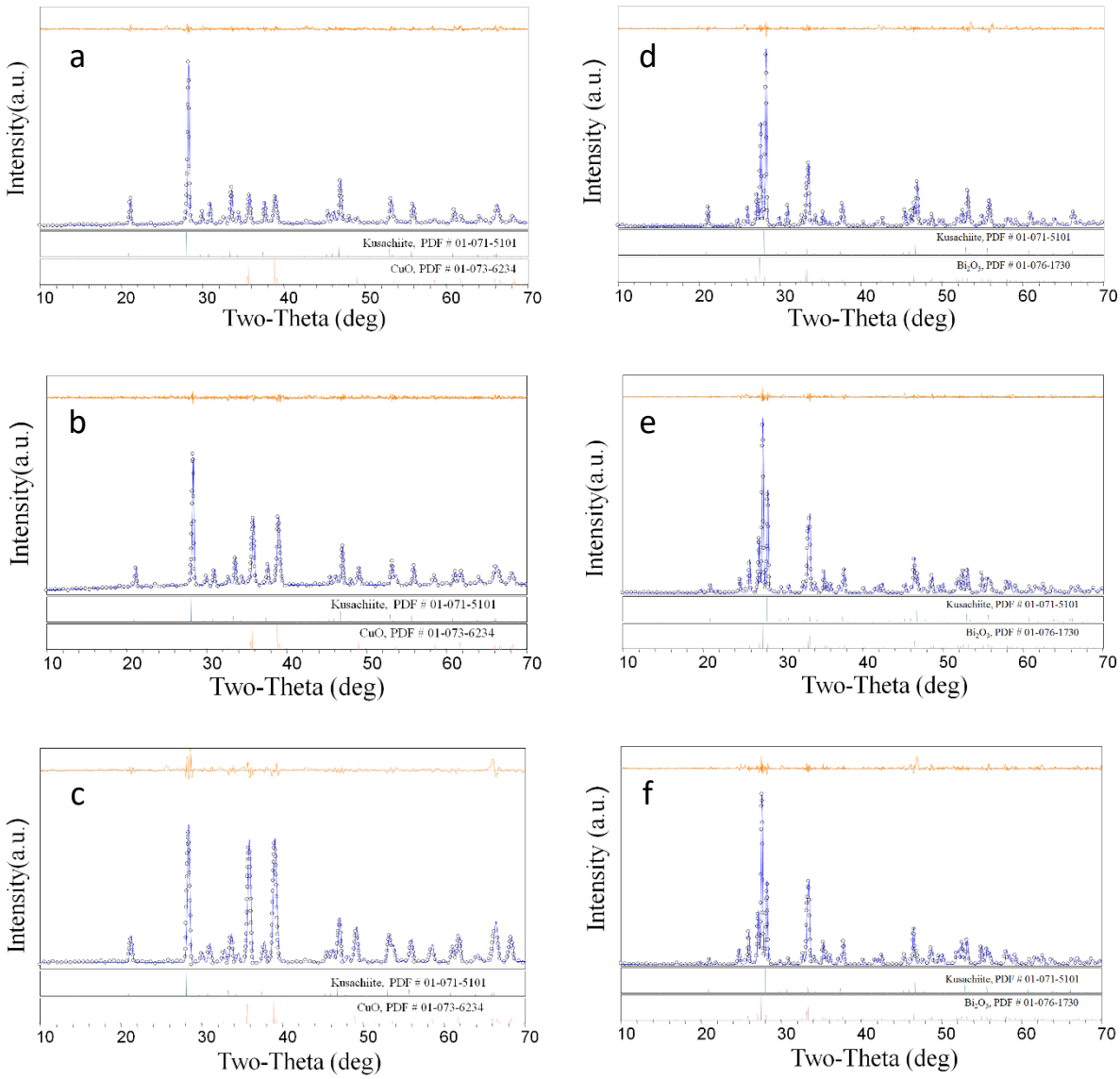

Figure A-S5. Rietveld refinement of XRD data for $CuO/CuBi_2O_4$ (frames a, b and c) and α-$Bi_2O_3/CuBi_2O_4$ (frames d, e and f).

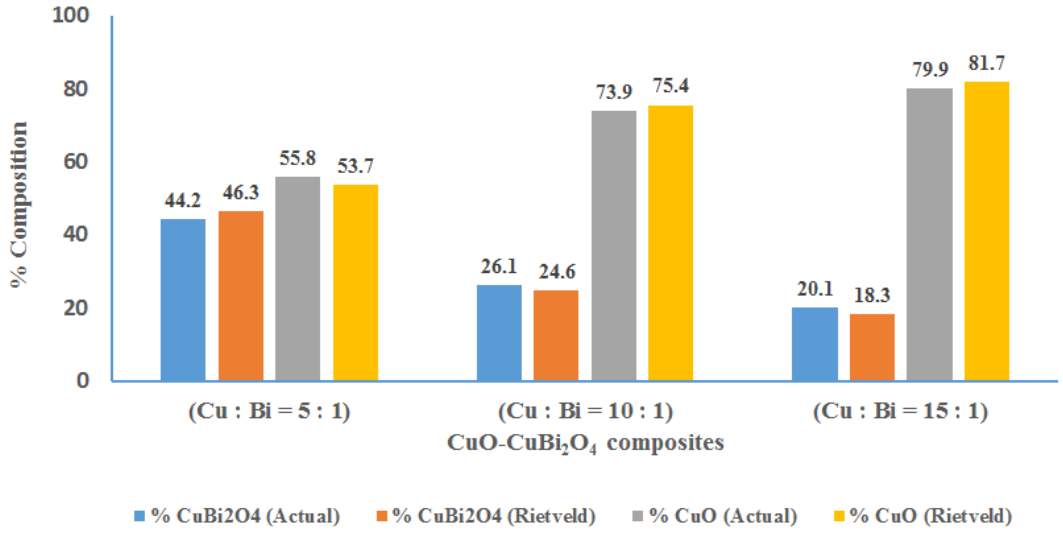

Figure A-S6. Comparison of results from Rietveld analyses for the $CuO/CuBi_2O_4$ for the three SCS-derived nanocomposite samples.

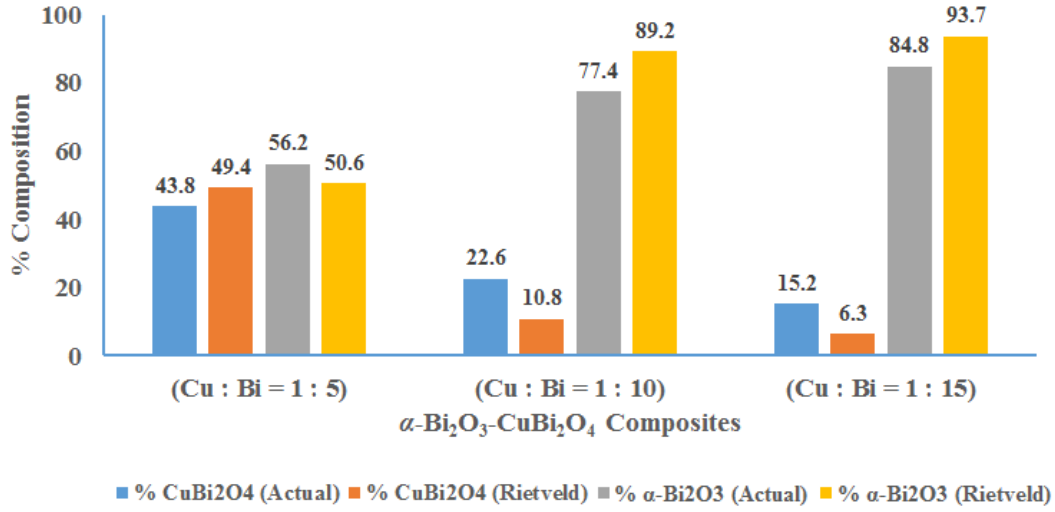

Figure A-S7. Comparison of results from Rietveld analyses for α-$Bi_2O_3/CuBi_2O_4$ for the three SCS-derived nanocomposite samples.

Table A-S1. Percent composition and goodness of fit for $CuO/CuBi_2O_4$ and α-$Bi_2O_3/CuBi_2O_4$ composites as obtained from Rietveld and comparison with theoretical yields.

Sample identification	Cu : Bi mole ratio	$CuBi_2O_4$ (%) Rietveld (Expected)	CuO (%) Rietveld (Expected)	Goodness of fit (χ^2)
$CuO/CuBi_2O_4$ (5:1)	5 : 1	46.3 (44.2)	53.7 (55.8)	1.27
$CuO/CuBi_2O_4$ (10:1)	10 : 1	24.6 (26.1)	75.4 (72.9)	1.13
$CuO/CuBi_2O_4$ (15:1)	15 : 1	18.3 (20.1)	81.7 (79.9)	1.12
Sample identification	Cu : Bi mole ratio	$CuBi_2O_4$ (%) Rietveld (Expected)	α-Bi_2O_3 (%) Rietveld (Expected)	Goodness of fit (χ^2)
α-$Bi_2O_3/CuBi_2O_4$ (1:5)	1 : 5	49.4 (43.8)	50.6 (56.2)	1.45
α-$Bi_2O_3/CuBi_2O_4$ (1:10)	1 : 10	10.8 (22.6)	89.2 (77.4)	1.36
α-$Bi_2O_3/CuBi_2O_4$ (1:15)	1 : 15	6.3 (15.2)	93.7 (84.8)	1.75

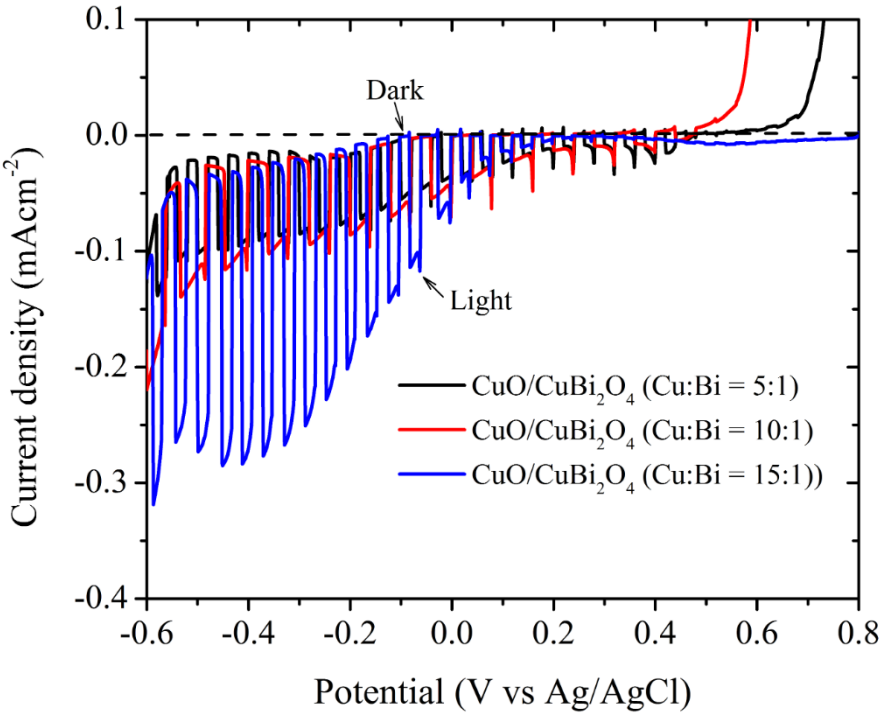

Figure A-S8. Chopped (light/dark) linear sweep voltammetry scans (scan rate 1 mVs^{-1}) for $CuO/CuBi_2O_4$ composites in 0.1 M $NaSO_4$ with N_2 bubbling. Scans were performed with frontside illumination.

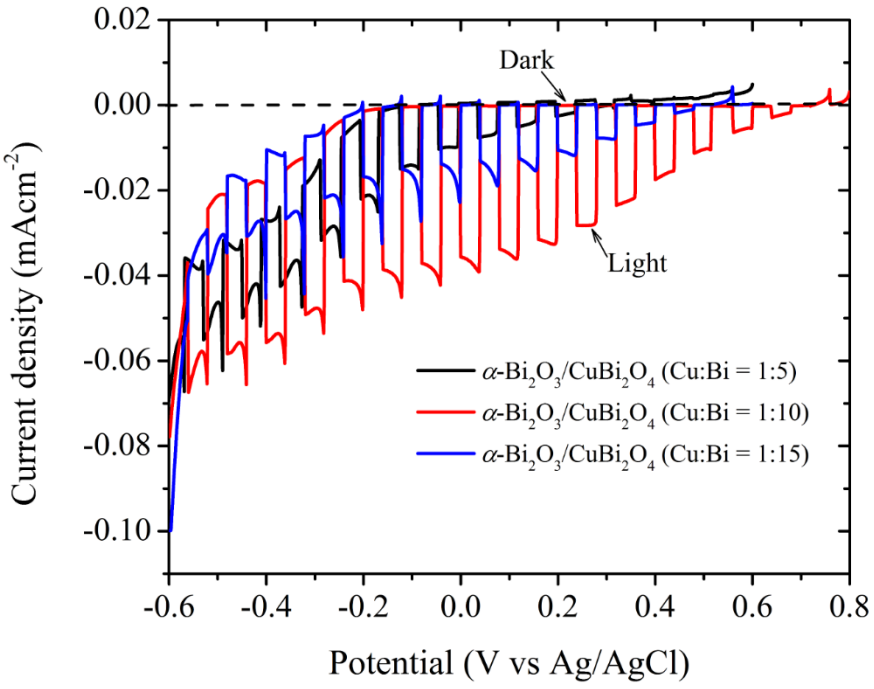

Figure A-S9. Chopped (light/dark) linear sweep voltammetry scans (scan rate 1mv/sec) for α-$Bi_2O_3/CuBi_2O_4$ composites in 0.1 M $NaSO_4$ with N_2 bubbling. Scans were performed with front side illumination.

APPENDIX B

SUPPORTING INFORMATION FOR CHAPTER 4

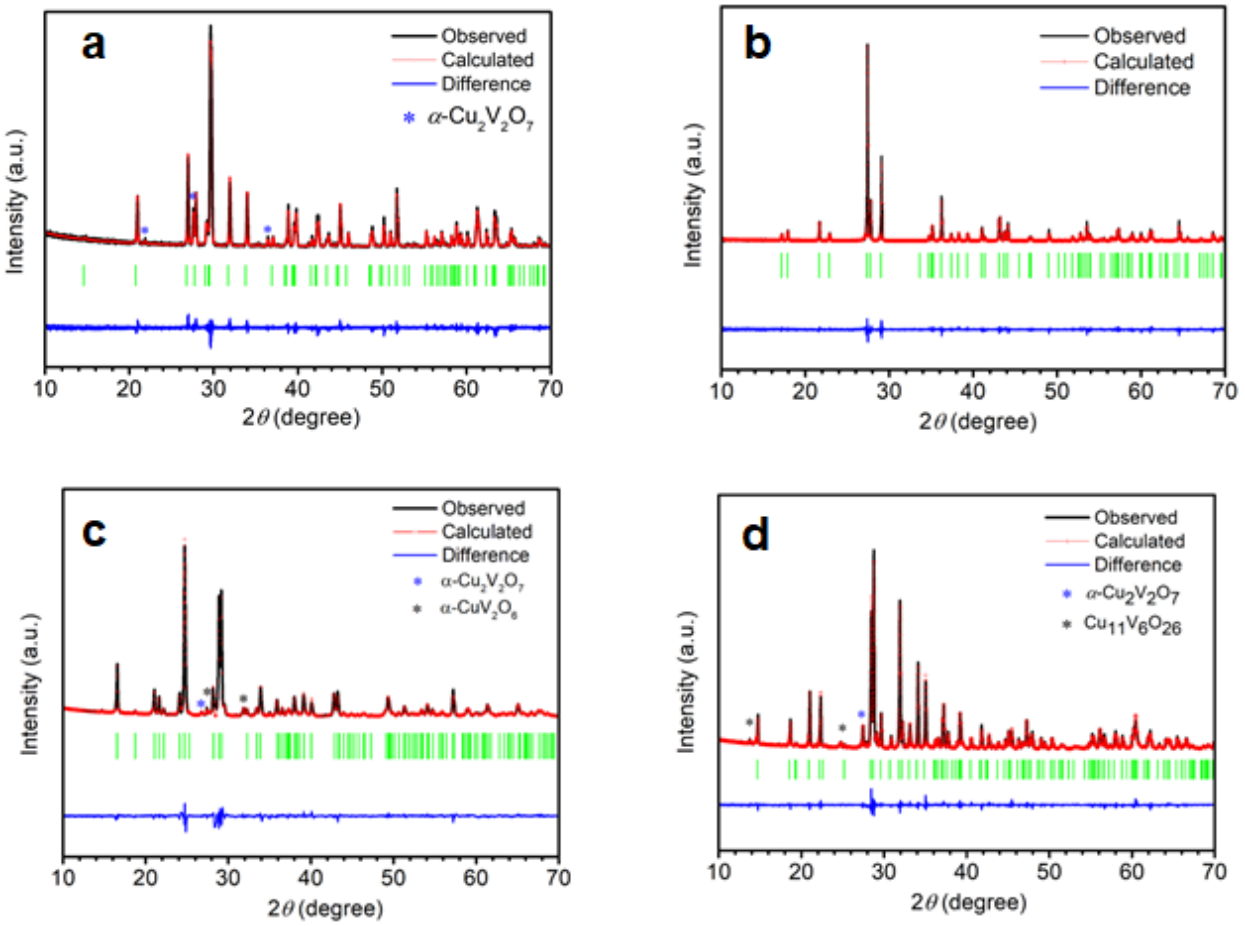

Figure B-S1. XRD patterns (black), Rietveld model (red) and difference (blue) of (a) α-CuV_2O_6, (b) α-$Cu_2V_2O_7$, (c) β-$Cu_2V_2O_7$ and (d) γ-$Cu_3V_2O_8$. Bragg reflections are shown in green.

Table B-S1. Unit cell parameters of the synthesized samples along with the standard cell parameters from database.

Oxides	Space group	*a* (Å)	*b* (Å)	*c* (Å)	*α* (°)	*β* (°)	*γ* (°)	V (10^6 pm^3)	JCPDS #
α-CuV_2O_6	$P\bar{1}$ (2)	3.543	4.859	6.478	69.991	87.750	70.514	98.450	01-074-2117
		3.550(3)	4.863 (5)	6.476 (5)	69.986 (1)	87.692 (2)	70.367 (2)	98.622 (1)	This study
α-$Cu_2V_2O_7$	*Fdd*2 (43)	20.676	8.392	6.446	90.000	90.000	90.000	1118.460	01-073-2487
		20.671(4)	8.402 (2)	6.444 (1)	90.000	90.000	90.000	1119.32 (2)	This study
β-$Cu_2V_2O_7$	*C*2/*c* (15)	7.689	8.028	10.106	90.000	110.252	90.000	585.350	01-076-2820
		7.694(3)	8.042 (3)	10.115 (3)	90.000	110.243(6)	90.000	587.54 (1)	This study
γ-$Cu_3V_2O_8$	$P\bar{1}$ (2)	5.196	5.355	6.505	69.220	88.690	68.080	155.730	01-074-1401
		5.185(6)	5.346 (7)	6.510 (7)	69.265 (2)	88.653 (2)	68.100 (2)	155.396 (1)	This study

Table B-S2. Rietveld refinement results for various copper vanadate samples.

Oxides	R_{exp} (%)	R_p (%)	R_{wp} (%)	χ^2
α-CuV_2O_6	9.66	8.27	10.87	1.12
α-$Cu_2V_2O_7$	4.02	4.12	4.43	1.10
β-$Cu_2V_2O_7$	4.86	7.63	10.80	2.22
γ-$Cu_3V_2O_8$	4.91	5.97	7.81	1.58

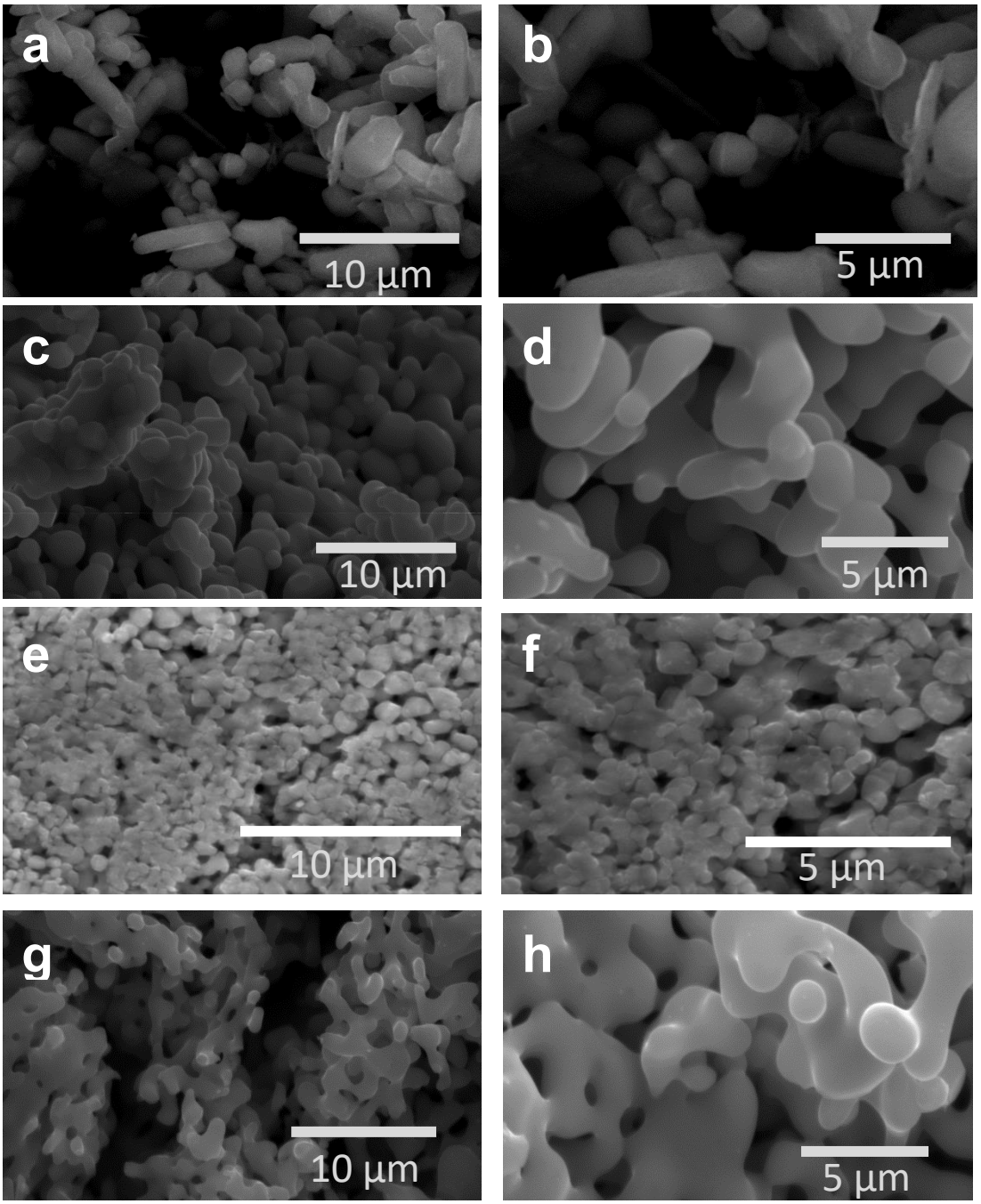

Figure B-S2. SEM images (a, b) α-CuV_2O_6 annealed at 600 °C (c, d) α-$Cu_2V_2O_7$ annealed at 610 °C (e, f) β-$Cu_2V_2O_7$ annealed at 500 °C and (g, h) γ-$Cu_3V_2O_8$ annealed at 610 °C.

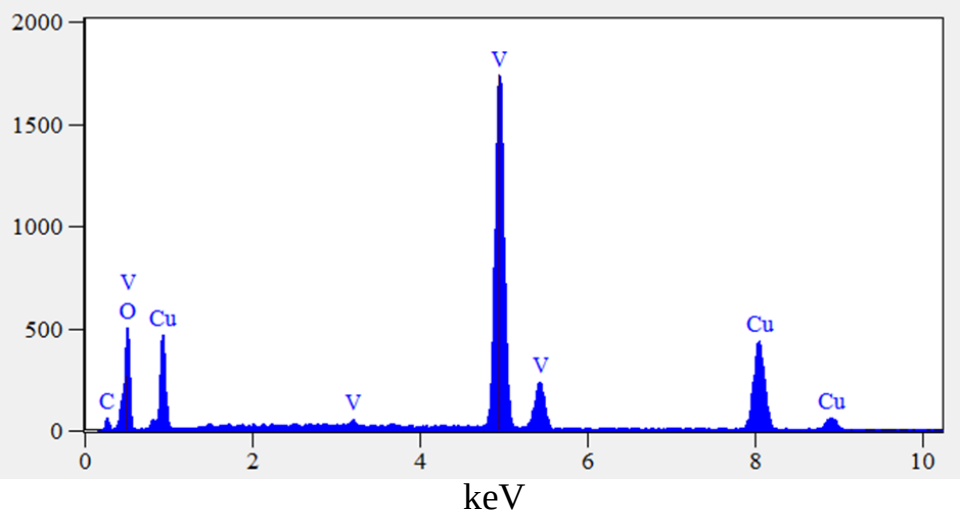

Figure B-S3. EDX spectrum of α-CuV_2O_6.

Table B-S3. V/Cu ratio from EDX analysis of annealed samples.

	V/Cu ratio			
Oxides	α-CuV_2O_6	α-$Cu_2V_2O_7$	β-$Cu_2V_2O_7$	γ-$Cu_3V_2O_8$
Experimental	2.14 (±0.02)	1.17(±0.02)	0.96 (±0.02)	0.76 (±0.03)
Expected	2.00	1.00	1.00	0.66

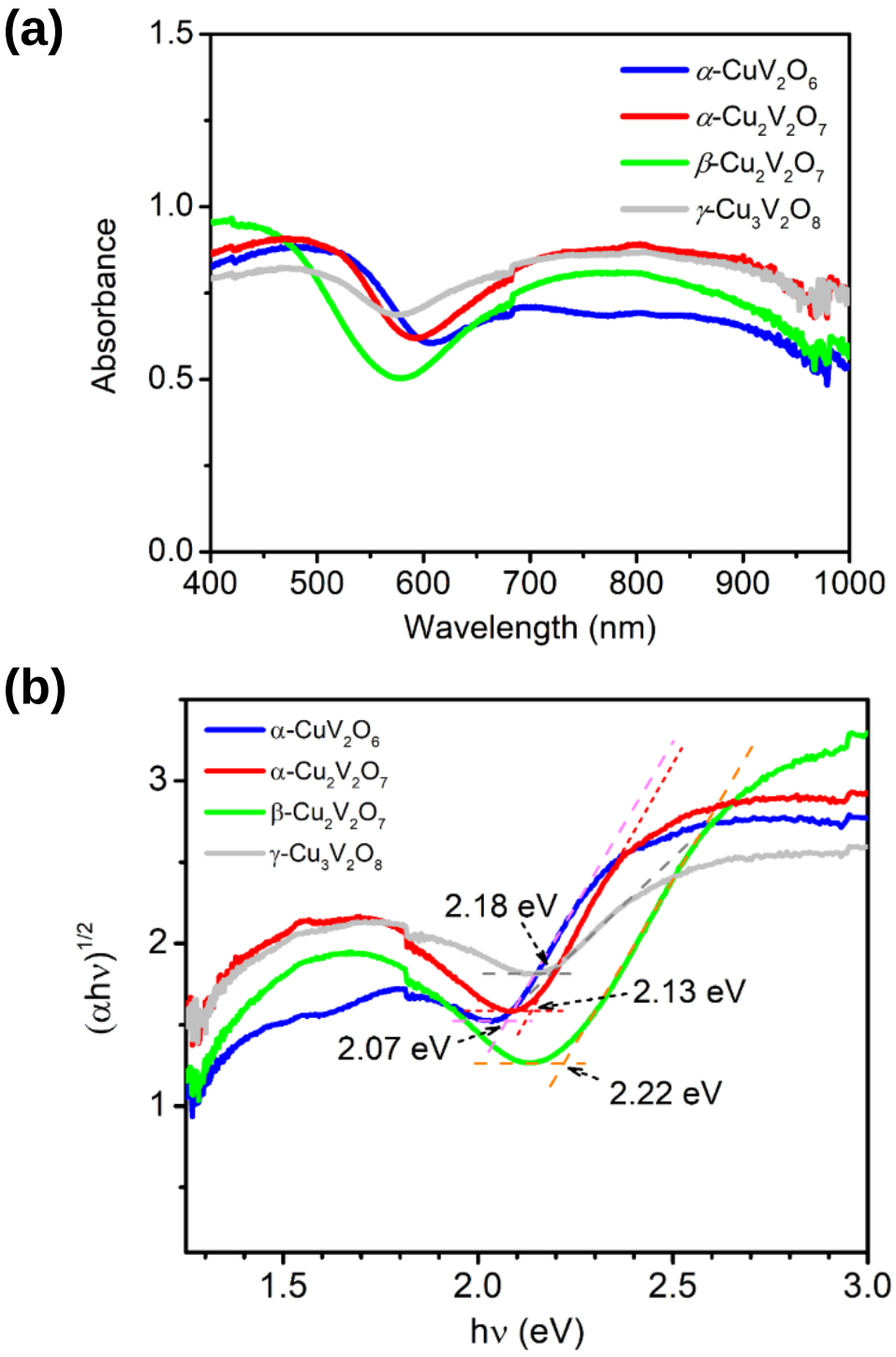

Figure B-S4. Absorbance (a) and indirect band gaps (b) of four copper vanadates.

BIOGRAPHICAL INFORMATION

Mohammad Kabir Hossain was born and raised in Narayanganj, Bangladesh. He earned a bachelor's degree in applied chemistry & chemical technology and a master's degree in applied chemistry & chemical engineering from the University of Dhaka. After a short stint at academia as a lecturer of chemistry, he moved to Manchester, UK under the Equity and Merit Scholarship and obtained his second master's degree in environment & sustainable technology. He then went back to his home country and took on a position as a laboratory in-charge of an analytical testing lab, and later he successfully co-founded an environmental consulting firm named 3R Environmental Consulting Limited. His intellectual pursuits and desire for deeper understanding, eventually, brought him to the United States in 2014 where he received his doctorate in Chemistry in August, 2019. His research focuses on the studies of multinary oxide semiconductors for solar energy conversion and environmental remediation. In this regard, he studied several complex oxides in the Cu-Bi-V-O system using a rapid 'one-pot' solution combustion synthesis (SCS) towards solar water splitting applications. In addition, he gained R&D experience on lithium-ion battery electrode materials at Sid Richardson Carbon & Energy Co. (currently Tokai Carbon) under the three-month internship program funded by National Science Foundation. He aspires to continue his research adventure either in academia or industry.